UiT The Arctic University of Norway

Faculty of Science and Technology / Department of Geosciences

Biogeochemistry of dissolved organic matter in Arctic Ocean waters charged with methane

Muhammed Fatih Sert

A dissertation for the degree of Philosophiae Doctor - July 2022

Biogeochemistry of dissolved organic matter in Arctic Ocean waters charged with methane

Muhammed Fatih Sert

A dissertation for the degree of Philosophiae Doctor

Faculty of Science and Technology

Department of Geosciences

Tromsø, July 2022

UiT Norges arktiske universitet

Supervisors:

Dr. Anna Silyakova[1]

Dr. Friederike Gründger[1,2]

Professor Helge Niemann[1,3,4]

[1]CAGE- Centre for Arctic Gas Hydrate, Environment and Climate
Department of Geosciences,
UiT The Arctic University of Norway, Tromsø, Norway

[2]Arctic Research Centre,
Department of Biology,
Aarhus University, Aarhus, Denmark

[3]NIOZ Royal Institute for Sea Research,
Department of Marine Microbiology and Biogeochemistry,
Utrecht University, Texel, the Netherlands

[4]Department of Earth Sciences, Faculty of Geosciences,
Utrecht University, Utrecht, the Netherlands

ISBN: 978-82-8236-494-2 (printed version)/ 978-82-8236-495-9 (electronic version)

Front page image: A rosette entering the Arctic Ocean waters (Photo: Torger Grytå).

Nearing Gemlik,
You'll see the sea;
Don't be suprised.

- Orhan Veli, 1942

Preface

This doctoral thesis was executed at the Department of Geosciences, UiT-The Arctic University of Norway, Tromsø from January 2017 to January 2022, under the supervision of Dr Anna Silyakova, Dr Friederike Gründger and Prof. Helge Niemann at the Centre for Arctic Gas Hydrate, Environment and Climate (CAGE). The project was funded by the Research Council of Norway Centers of Excellence funding scheme grant no. 223259.

As a requirement for the PhD program at UiT, I attended several courses as an individual instruction component including courses yielding a total of 30 credits, comprising 27 credits within mathematical/scientific subjects (marine geology and geophysics, molecular ecology, ecological statistics and chemometrics) and 3 credits in the field of ethics and theory of science. I took two of my courses abroad and financial support was provided by the UiT travel grant for PhD candidates.

As a doctoral candidate at the Department of Geosciences, 25 % of the four-year period is dedicated to duty works including the preparation and teaching classes for GEO-2008 (Environmental Geology), assisting student exercises for GEO-2008 (Geochemistry), laboratory assistance in the geology lab and participating scientific cruises. In addition to the four-year PhD period, 10 months of parental leave and 2 months of Covid extension were added to extend my PhD contact one year in total.

During my PhD project, I was affiliated with the trainee school Geoscience Research Academy of Tromsø (GReAT; formerly AMGG-Arctic Marine Geology and Geophysics), the Norwegian Research School on Changing Climate in the coupled Earth System (CHESS) and the Arctic Marine Ecosystem Research Network (ARCTOS). Preliminary results from this project were in various international conferences and workshops including Ocean Science Meeting 2018 in Portland, Oregon, USA.

This doctoral thesis is composed of a chapter for introduction and summary of the work, two published papers (PAPER I and PAPER II), and one manuscript in preparation (PAPER III). Altogether, this study provides new insights into the Arctic dissolved organic matter dynamics in relation to methane-related processes.

Papers included in the thesis are:

- Sert, M. F., D'Andrilli, J., Gründger, F., Niemann, H., Granskog, M. A., Pavlov, A. K., Ferré, B. and Silyakova, A. 2020. **Compositional Differences in Dissolved Organic Matter Between Arctic Cold Seeps Versus Non-Seep Sites at the Svalbard Continental Margin and the Barents Sea**, Frontiers in Earth Sciences. doi:10.3389/feart.2020.552731

  Data used in the paper: https://doi.org/10.18710/JHB371

- Sert, M. F., Niemann, H., Reeves, E. P., Granskog, M. A., Hand, K. P., Kekäläinen, T., Jänis, J., Rossel, P. E., Ferré, B., Silyakova, A. and Gründger, F. 2022. **Composition of dissolved organic matter in the ice-covered water column above hydrothermal vents at the Aurora Seamount, Gakkel Ridge, Arctic Ocean**, Biogeosciences. doi.org/10.5194/bg-19-2101-2022.

  Data used in the paper: https://doi.org/10.18710/QPGDFW

- Sert, M. F., de Groot, T., Kekäläinen, T., Jänis, J., Gründger, F., Niemann, H. and Silyakova, A. **Elevated methane alters dissolved organic matter composition in the Arctic Ocean cold seeps**.

  Data used in the paper: https://github.com/fatihserta/Incubation_2022.git

Acknowledgement

This thesis has been conducted with the tremendous support and guidance of the best-ever team of supervisors, Anna Silyakova, Friederike Gründger, and Helge Niemann. I would like to thank them for providing me with this opportunity and supporting me in every inch of this project with positive motivation.

I am grateful to my team leader Bénédicte Ferré for her support during these years, always with open-minded and considerate leadership.

I acknowledge the coauthors of the papers presented in this thesis, especially Mats Granskog and Juliana D'Andrilli, for being always available and supportive during experimental works and discussions.

I am tankful to geology lab personnel Matteus Lindgren, Trine Dahl, Karina Monsen, Ingvild Hald and Fabio Sarti. They made all lab work and arrangements super easy and efficient with big smiles.

I would like to acknowledge a mentor and friend from Turkey, Erol Kabil, who taught the basics of mass spectrometry and made this whole PhD journey smoother for me.

I would like to thank the DTU team, Colin Stedmon and Urban Wünsch, for their friendly support and for having me in their lab in beautiful Copenhagen.

I am grateful to all my friends, colleagues, and the leadership in CAGE and IG who made our department a great place to work.

And I am truly grateful to my love, best friend, and beautiful wife, Zeynep Sancak Sert. I thank you for your support, patience and friendship at this end of the world with miraculous polar nights and midnight suns.

Abstract

Dissolved organic matter (DOM) is defined as the organic substances that do not retain on a filter (pore size 0.1-1 µm) during the filtration of aquatic samples. DOM comprises the largest reservoir of reduced carbon (700 Pg C) and is closely associated with all oceanic elemental cycles and ecosystem processes. DOM is an essential component of the microbial loop and marine food web.

Methane is seeping from numerous geological sources in the Arctic Ocean associated with multiple mechanisms that elevate methane production and release. Independent of the mechanism, however, liberated methane is predominantly consumed in the water column by methanotrophic bacteria (MOB), which uses methane as a carbon and energy source during an aerobic enzymatic reaction called methane oxidation (MOx). In sedimentary fluid flow systems such as cold seeps or hydrothermal vents, the amount of methane release and subsequent MOx would be substantial that may trigger other ecosystem processes such as bacterial growth, heterotrophic consumption, and mechanisms that alter DOM composition in the water column.

Methane is one of the most potent greenhouse gasses in the atmosphere, and it has been quantified extensively in oceanic environments due to its subsequent effect on global warming. Its fate in the water column has been investigated in different geological settings. However, the impact of methane emanation and methane-driven processes on DOM dynamics has been merely constrained in the water column. The main objective of this thesis is to unravel the modifications in the DOM composition associated with the methane release in the Arctic Ocean cold seeps and hydrothermal vents.

Two field studies and a laboratory experiment have been conducted. The main focus areas were the methane receiving waters above Arctic cold seeps in continental shelves of Svalbard and the Barents Sea (Paper I) and Aurora hydrothermal vents in the Gakkel Ridge (Paper II). Studied areas were characterised by main oceanographic properties, methane distribution and molecular DOM compositions obtained by Fourier transform ion cyclotron resonance mass spectrometry (FT-ICR MS). Methane-driven modifications in DOM composition were further investigated by short term laboratory incubations (Paper III).

DOM compositions were chemically more diverse (3-5 %) and heterogeneous in methane-releasing cold seeps in coastal Svalbard and the central Barents Sea. Active cold seeps were located with hydroacoustics surveys, and a significant correlation was observed between seep activity and DOM compositions in terms of lability, molecular diversity and percentage of nitrogen-containing molecular formulas. On the other hand, the general water column biogeochemistry was essentially controlled by the hydrography, water mass properties and the primary production cycles. The variety of DOM compositions between seep and non-seep stations was suggested to be the "legacy" fingerprint of methane-driven DOM modifications and associated with multiple factors, including MOB activity, seeping of sedimentary DOM, seep fertilization and other microbial modifications.

Mechanisms behind the seep-associated DOM modifications were investigated further by short-term ex-situ incubations. Seawater samples were collected from the seep and non-seep stations and incubated in methane amended and unamended conditions. Methane amended samples in seep, and non-seep incubations show similar results: the number of molecular formulas increased up to 39 % and DOM compositions modified towards more diverse and heterogeneous compositions along with the elevated MOx activity. Data suggested that elevated methane concentrations, as happens in cold seeps, influenced both production and consumption of DOM.

Hydrothermal vents constitute another source of methane to the hydrosphere. Investigations in Aurora hydrothermal vents in the Gakkel ridge showed that DOM compositions had a lower number of formulas, 5-10% less molecular diversity and a lower percentage of formulas associated with the lipid-like molecular class in plume layer samples compared to non-plume samples at similar depths. Molecular differences were associated with isotopically heavier methane and other vent-derived properties. Hydrothermal processes modify DOM either with hydrothermal intrusion or vent-associated microbial activities and displace to a distance from the vent by the hydrothermal plume dispersion.

Research papers included in this thesis bring a new perspective for comprehending changes in the Arctic Ocean biogeochemistry and are a humble contribution to understanding DOM cycles in global oceans.

Contents

Chapter 1

Introduction

1.1 Background

1.1.1 Marine DOM

Marine dissolved organic matter (DOM) is Earth's largest DOM pool and the ocean's largest reservoir of reduced carbon. The carbon content of the marine DOM (dissolved organic carbon; DOC) is comparable to the mass of CO_2 carbon in the atmosphere. DOM production comprises an important transport mechanisms of atmospheric CO_2 to the deep ocean by organic carbon and microbial carbon pumps (Jiao et al., 2010). Therefore, variation in the DOM pool might impact atmospheric CO_2 and the radiative equilibrium of the Earth (Dittmar and Stubbins, 2014).

Marine DOM is derived predominantly from photosynthesis in the lit ocean. Primary producers (phytoplankton and photosynthetic bacteria) utilise inorganic carbon and other essential nutrients (e.g., nitrate, phosphate, silicate, iron) to produce organic matter in the presence of oxygen (electron acceptor). Primary production at the euphotic layer corresponds to approximately half of global organic matter production 50 Pg C (10^{15} g) per year (Armstrong et al., 2001; Hedges, 1992; Muller-Karger et al., 2005) and contributes approximately 100-times higher amount of organic carbon to the oceans than the sum of terrestrial input through river discharge (0.4 Pg C $year^{-1}$), aeo-

lian transport and wet deposition (0.1 Pg C year^{-1}) (Hedges, 1992). In addition to the production in the photic layers, the global rate of carbon fixation by chemoautotrophs is estimated to be 0.77 Pg C year $^{-1}$ which eventually contribute production of DOM through resuspension in near-shore and shelf sediments, nitrification in the euphotic zone and chemolithotrophs the dark ocean (Middelburg, 2011). Other than the input at the surface and coastal oceans, one external source of DOM is the sedimentary efflux of DOM through resuspension, cold hydrocarbon seeps and hydrothermal vents. Although the amount of DOM efflux through cold seeps and hydrothermal vents is relatively unknown, the total benthic influx is estimated as 0.18 Pg C year^{-1}, which is essentially equivalent to the organic carbon burial rate in marine sediments (Burdige et al., 1999).

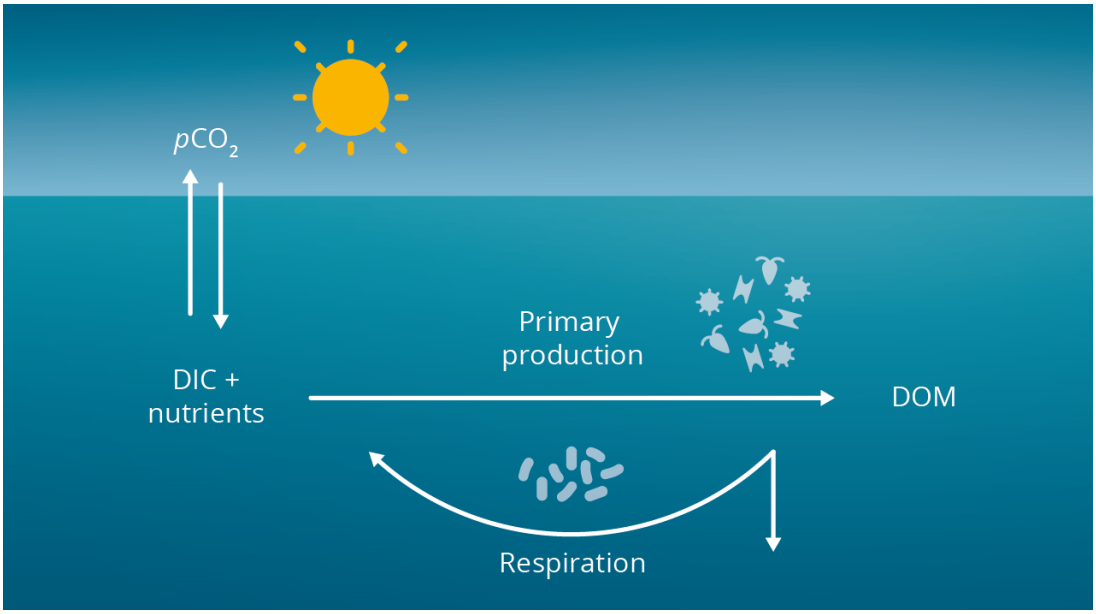

Figure 1.1 – *The main perspective for the DOM cycle in the oceans: dissolved inorganic carbon (DIC) and essential nutrients are utilized by primary producers at the euphotic zone. Bacteria utilize most of the labile DOM and regenerate nutrients by respiration.* Credit: Torger Grytå, UiT.

Once organic compounds synthesize within the cell, phytoplankton and bacteria actively release DOM constituents for nutrient acquisition, intracellular communication or chemical defense in connection with the nutrient status, growth conditions and microscale ecosystem properties (Kujawinski, 2011, and references therein). Plankton excrete transparent exopolymer compounds (usually polysaccharides) to construct an extracellular envelope which helps them aggregate during plankton blooms, scavenge DOM from

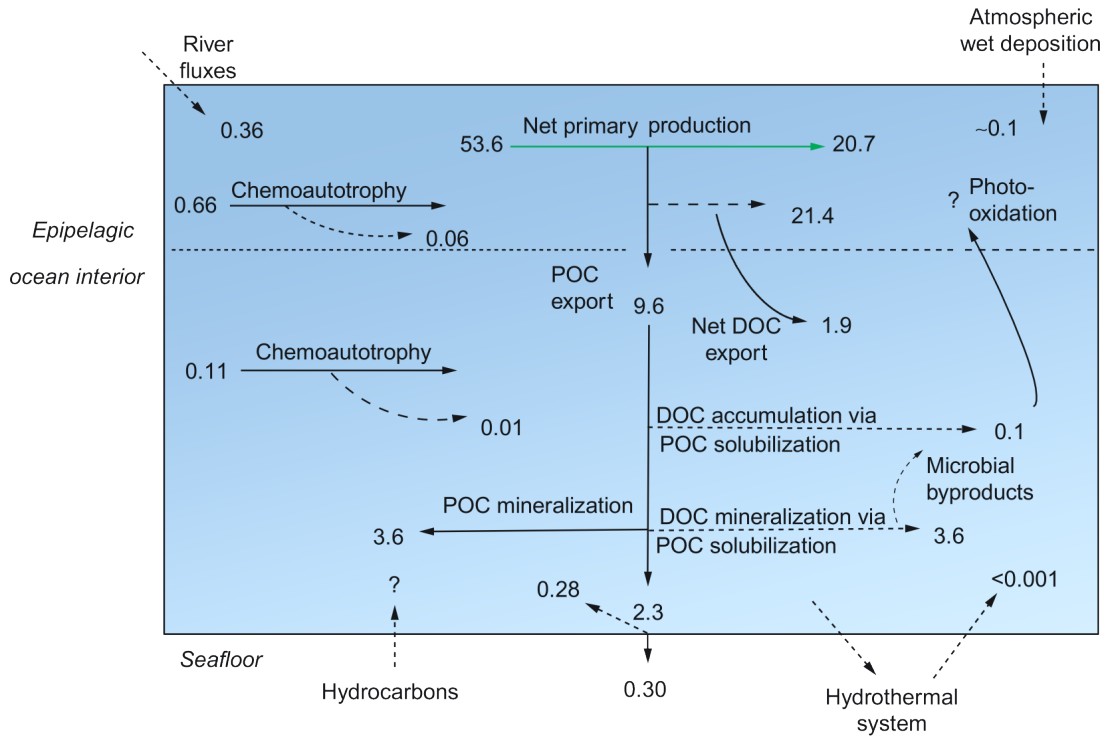

Figure 1.2 – *Main oceanic organic carbon pathways and fluxes (Pg C year-1), assuming inventories are in a steady state. Solid and dashed arrows represent particulate and dissolved organic matter, respectively. All input fluxes are balanced by removal. The figure is retrieved from Carlson and Hansell (2015).*

water and provide buoyancy (Dittmar and Stubbins, 2014, and references therein). In addition, grazer-mediated release (sloppy feeding), bacterial and viral cell lysis, and excretion also contribute to DOM production in all the layers of the ocean (Carlson and Hansell, 2015).

Microbes produce hundreds of thousands of different organic molecules as a part of their metabolic systems. Therefore, current DOM compositions in modern oceans are as versatile and complex as the metabolisms of marine microbes. Microbes also assimilate molecules entirely or cleaved fragments with the help of extracellular enzymes (Kujawinski, 2011). Depending on the reactivity and composition of incorporating constituents, DOM is an energy, nutrient and carbon source for most marine heterotrophic prokaryotes (bacteria and archaea) that use chemoheterotrophic respiration as a primary metabolic strategy (Carlson and Hansell, 2015). Although the production of DOM is ultimately derived from biotic processes, the decomposition of DOM can also be mediated by abiotic processes such as photooxidation, sorption on particles, and

hydrothermal circulations (Carlson and Hansell, 2015). Nevertheless, microbial consumption (mainly bacteria and archaea) of DOM is the ultimate metabolic strategy in the contemporary aerobic ocean (Carlson and Hansell, 2015) and comprises the fundamental role in DOM removal.

Combining these two main production and consumption pathways, the DOM cycle mainly (not exclusively) consists of production in the euphotic (sunlit) ocean by primary producers and remineralization in the water column by the heterotrophic microbes. The machinery behind the cycle is either administrated by the gravity along with the dissolution of sinking particles (organic carbon pump) or direct metabolism of dissolved or suspended organic matter by bacteria (microbial pump). Oceanic DOM inventory is assumed to be a steady-state with 662 Pg C of total budget corresponding to roughly 370 years of residence time with 1.8 Pg C year $^{-1}$ annual flux (Hansell et al., 2009). However, radiocarbon (Δ^{14}C) data indicate the average age of DOC is around 5000 years deep ocean (>900m) and about 3000 years at the epipelagic and mesopelagic layers of the Pacific and Atlantic Oceans (Bauer et al., 1992). Such a big difference in oceanic DOC ages implies significant variability in turnover rates and ease of decomposition between the different fractions of DOM. Such as, some portion of DOM is easily uptaken and metabolized in a very short time scale (minutes to days), but some molecules remain in the water column in millennium scale persistency. Regarding this, marine DOM is usually characterized in two main fractions, namely, labile, and refractory DOM.

Although there are debates on the definitions of each fraction and the roles of different classifications (e.g., Baltar et al., 2021), and whether DOM is rather a single pool of molecules characterized by a continuum of reactivity (e.g., Middelburg, 1989; Vähätalo et al., 2010), defining different pools of DOM with their lifetimes in water was found to be operationally useful (Hansell, 2013). Such as, labile DOM is defined as molecules that are consumed within hours to days of production and therefore, it represents only a tiny fraction (<0.2 Pg) of the global inventory at any given moment (Repeta, 2015). Conversely, refractory DOM is the portion of DOM that escapes from the rapid remineralization in the upper layers and accumulates as the residual, biologically recalcitrant pool of molecules that survive from years to millennia throughout the oceanic cycles

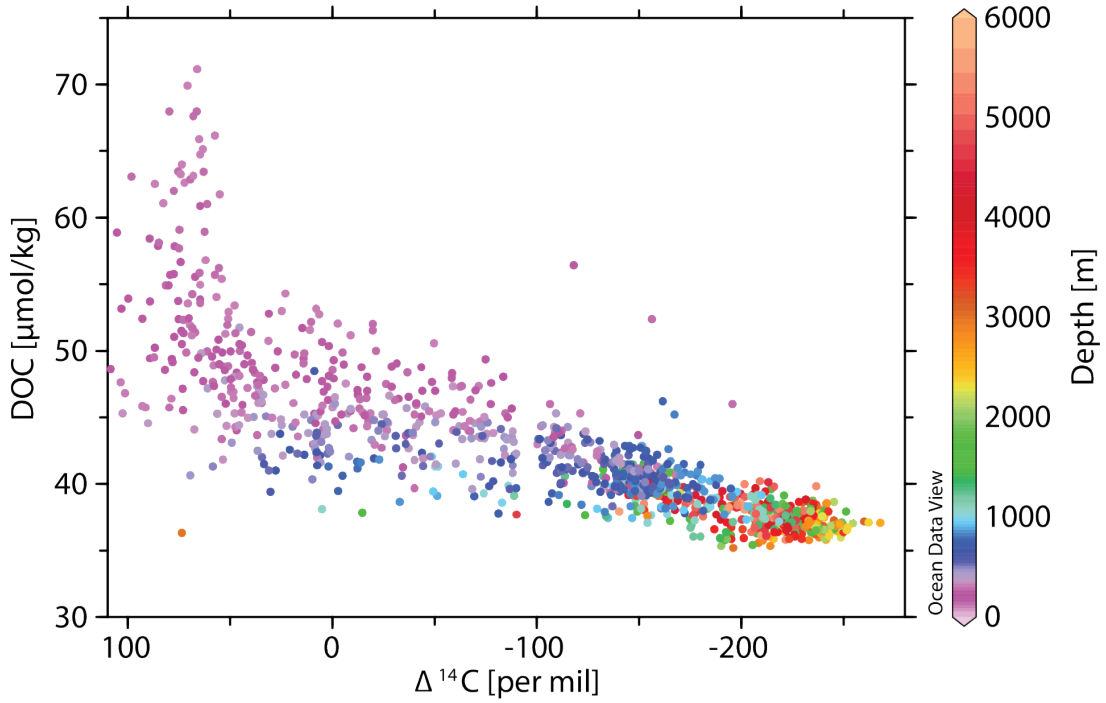

Figure 1.3 – *DOC concentrations versus $\Delta^{14}C$-DOC values (per mil deviation from that of nineteen century CO_2) from a transect in the Pacific Ocean. The figure is retrieved from Hansell et al. (2009).*

(Hansell, 2013; Lechtenfeld et al., 2015).

Resistance of refractory DOM to biodegradation is surprising and seems contradictory to thermodynamic equilibrium considering the efficiency of microbes in decomposing DOM under the presence of abundant oxygen and the potential yield of energy and nutrients (Dittmar, 2015; Dittmar and Stubbins, 2014; Moran et al., 2016). Hypotheses imply the role of microbes in the accumulation of refractory DOM, such that the bacteria generate refractory molecules inherently from labile sources over several lifecycles until they are resistant to further bacterial decomposition (Brophy and Carlson, 1989; Jiao et al., 2010; Lechtenfeld et al., 2015; Ogawa et al., 2001). However, this view was challenged by incubation experiments indicating that only a small portion of net community production (<0.4%) resembles oceanic refractory DOM (Osterholz et al., 2015), and DOM in the deep ocean is too dilute to be a viable source for bacteria (Arrieta et al., 2015).

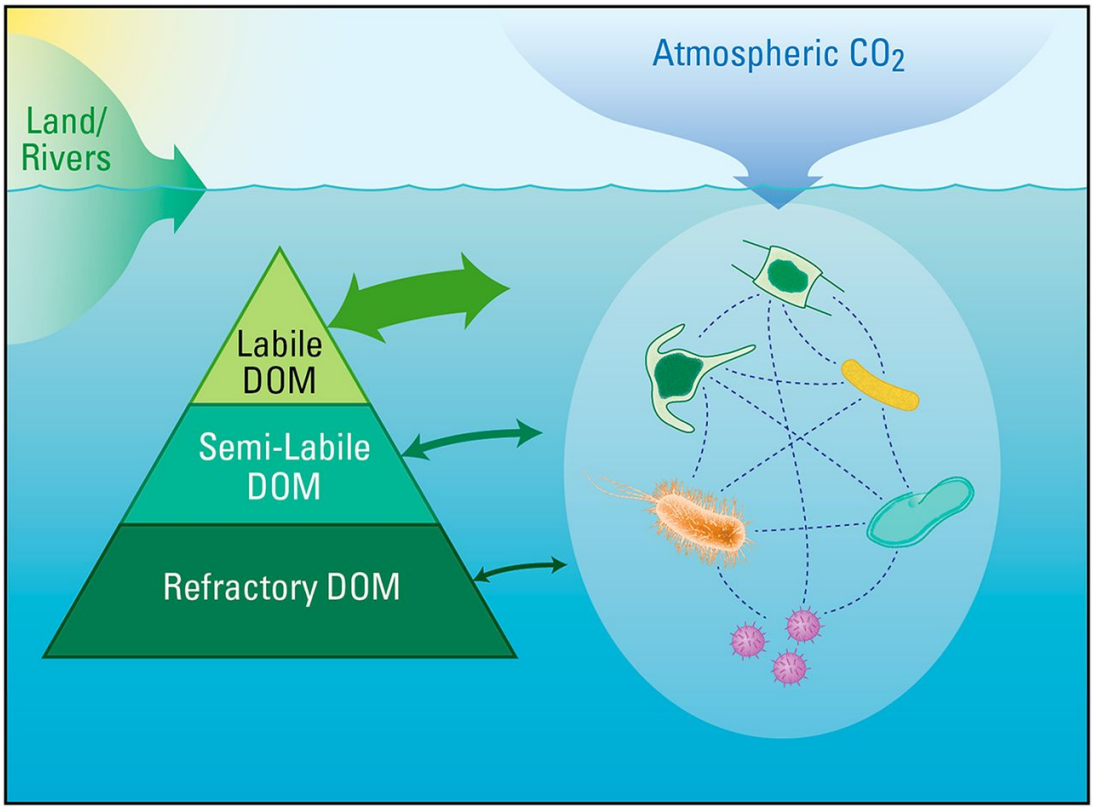

Figure 1.4 – *Fractions of DOM with their relative reactivities, budgets and depths. Arrows represent microbe DOM interactions where arrow thickness illustrates reactivities toward microbial metabolism. The figure is retrieved from Moran et al. (2016).*

1.1.2 Analytical techniques and approaches for analyzing DOM

The tremendous variety of involving microbial processes, chemical reactions, and complex food web interactions make DOM an extremely complex pool of chemical compounds. Based on different definitions, properties of the elements, and targeted compounds, analytical techniques range from quantifying bulk concentrations of carbon, nitrogen and phosphorus to stable/radio-isotopic contents or from molecule-specific analyses to immunochemical assays (Kujawinski, 2011; Mopper et al., 2007; Repeta, 2015). In the second edition of "Biogeochemistry of Dissolved Organic Matter", Daniel Repeta postulated that the 60-70 % of DOM is characterized in terms of major compound classes and distribution of major carbon, nitrogen, and phosphorus functional groups (Repeta, 2015). However, DOM research is now beyond this point, with the extensive contribution from the environmental metabolomics (e.g., Han et al., 2021; Hawkes et al., 2018; Petras et al., 2021) and advances in instrumental capacity (Hen-

drickson et al., 2015). Nevertheless, rather than being identified by the constituents, DOM is usually investigated by groups of substances (e.g., humic, biodegradable, non-extractable), biochemical classes (e.g., sugars, lipids, peptides), or elemental compositions (e.g., dissolved organic carbon, nitrogen, or phosphorus).

Due to the biochemical nature of the primary producers, the most common elements in cell tissues are carbon, hydrogen, oxygen, nitrogen, and phosphorus. Therefore, these common elements are also the main constituents of marine DOM. Historically, addressing bulk concentrations of these elements - especially dissolved organic carbon (DOC) and dissolved organic nitrogen (DON) - and quantifying separately after a selected oxidation method in marine samples was common. Many oxidation techniques were suggested, including wet chemical oxidation (Menzel, 1964) or photooxidation (Armstrong et al., 1966) in the early sixties, but then high-temperature catalytic oxidation became a standard method of choice in marine samples due to higher oxidation efficiency and precision (Qian and Mopper, 1996; Sharp et al., 1993; Sugimura and Suzuki, 1988). Although instruments for the molecular level characterization of the DOM are now more accessible, the determination of bulk concentrations of carbon, nitrogen, phosphorus, and sulfur in marine samples is still essential to comprehend the general cycle of DOM in marine environments and direct comparison of different environment.

Determination of isotopic compositions of DOC is another approach for distinguishing the source and lifetime of DOM. The isotopic composition of stable (δ^{13}C) and radioactive (Δ^{14}C) DOC are quantified by isotope ratio mass spectrometry and accelerator mass spectrometry, respectively, after ultraviolet (UV) oxidation (Beaupré et al., 2007). Isotopic ratios reported as permille (‰) represent deviations from internationally accepted standards. The natural tendency for the lighter CO_2 (higher ^{12}C content) during photosynthesis results in strong fractionation and depleted δ^{13}C (-21‰) and Δ^{14}C (-500 to -150‰) values for DOC compared to oceanic δ^{13}C (0‰) and Δ^{14}C (-300 to –150‰) DIC (Beaupré, 2015). The extent of fractionation is also related to community composition and environmental factors (e.g., temperature, pCO_2) and the relative significance can be traced by isotopic values (Beaupré, 2015). Radioisotope composition is also a powerful tracer for the age of DOM. With a series of corrections for isotopic fractionation and temporal variability atmospheric Δ^{14}C, it is possible to obtain a ^{14}C-age

and isotopic mixing model (e.g., Keeling plot) of bulk DOM or its constituents.

In order to obtain deeper insights into the chemical and molecular composition of DOM, two techniques are commonly used in the field. A relatively more accessible option is UV-visible and fluorescence spectroscopy, which is used by an expanding research community from environmental chemistry, limnology and oceanography. A large portion of DOM (20-70%) absorbs light over a broad range of UV and visible wavelengths and is called coloured or chromophoric DOM or CDOM. Chromophores are parts of molecules that capture the energy of photons and excite one of their lone pair electrons (-orbitals) from the ground state to the excited state by absorbing light from the light source. The light absorption of chromophores is proportional to the concentration by Beer-Lambert law; therefore, it provides quantitative information about the relative amount of CDOM in the water column. The shape of the absorption spectra of CDOM also provides information about the sources of DOM (e.g., allochthonous vs autochthonous) and their dominant molecular weights (Coble, 2007; Helms et al., 2008).

A variable portion of CDOM, fluorophores, is fluorescent at UV-visible wavelength. Fluorescence occurs while molecules return from an electronically lowest excited state to a ground state after losing energy with vibrational relaxation and internal conversion. Molecules with fewer vibrational degrees of freedom, like aromatic compounds, usually emit fluorescence, whereas aliphatic compounds' relaxation occurs without fluorescence (Stedmon and Nelson, 2015). These two properties can be combined for spectral analysis of DOM by exerting an excitation-emission matrix (EEM) to provide even more detailed insight into the chemical composition of DOM. EEMs comprise multiple emission spectra (e.g., 300-600 nm) at a range of excitations (e.g. 240-500 nm) (Coble, 2007; Stedmon and Nelson, 2015). Considering a multitude of samples, EEMs constitute a three-way array (sample by excitation by emission) and are often applied parallel factor analysis (PARAFAC) to characterize fluorescent DOM by decomposing the fluorescence matrices into independent fluorescent components, which provides an ability to trace these components in different samples (Stedmon et al., 2003; Stedmon and Bro, 2008).

Mass spectrometry (MS) is the other common technique for deciphering marine DOM constituents and compositions, which has been in use in DOM research for several decades (Mopper et al., 2007). Among many different MS configurations, Fourier trans-

form ion cyclotron mass spectrometry (FT-ICR MS) is one of the most comprehensive instrumental techniques for characterising molecular DOM in marine samples. FT-ICR MS was the central approach to determine the composition of DOM in this thesis. Therefore, details about this method and instrumental analysis are summarized in the following sections. Under a high magnetic field (up 21 T recently) FT-ICR MS offers immensely high resolving power (>2,000,000) and mass accuracy (>50 ppb) for complex DOM mixtures (Hendrickson et al., 2015; Koch et al., 2005). Prior to the FT-ICR MS detection, electrospray ionization (ESI) is the most common ionization method for the marine DOM.

1.1.3 Composition of DOM by FT-ICR MS

1.1.3.1 Extraction

Despite the advancement of molecular techniques for deciphering DOM compositions, isolation of DOM from sea salt is one of the major limitations for the compositional analysis in marine samples considering its relative amount compared to sea salt (ca $1/10^5$; w/w) (Mopper et al., 2007; Repeta, 2015). Among several other isolation techniques (e.g., reverse osmosis, ultrafiltration, coprecipitation), solid-phase extraction (SPE) of filtered, acidified seawater (pH 2-2.5) has the widest usage in marine DOM research. Accordingly, DOM is frequently (and more accurately) defined as SPE-DOM in compositional studies that use SPE as the extraction method (e.g., Dittmar et al., 2008; Gonsior et al., 2011; Hertkorn et al., 2013; Valle et al., 2018). A wide range of chemistries can be applied as sorbents in SPE extraction with changing polarities; such as octadecyl-bonded silica (e.g., C-18) and polystyrene divinyl benzene derivatives (e.g., PPL, ENV) were found to be working well for the retention of highly polar to nonpolar substances from a large volume of water for marine DOM samples (Dittmar et al., 2008).

1.1.3.2 Ionization

Mass spectrometry works with charged molecules. Therefore, ionizing the analyte molecules is essential to move ions toward detection under electric or magnetic fields. For ionization, electrospray ionization (ESI) in positive and negative modes is used in the papers in this thesis. ESI works at atmospheric pressure. The sample solution is pumped through a capillary spray needle with a typical flow rate of 0.1-10 microliter per minute. The needle is surrounded by an electrode that typically supplies 2-5 kV, negative or positive voltage. Then, a spray of charged droplets is formed at the tip of the Taylor cone, and the solvent in the droplets evaporates as they travel to the mass spectrometer entrance as free, charged analyte molecules (Cech and Enke, 2001; Skoog et al., 2007).

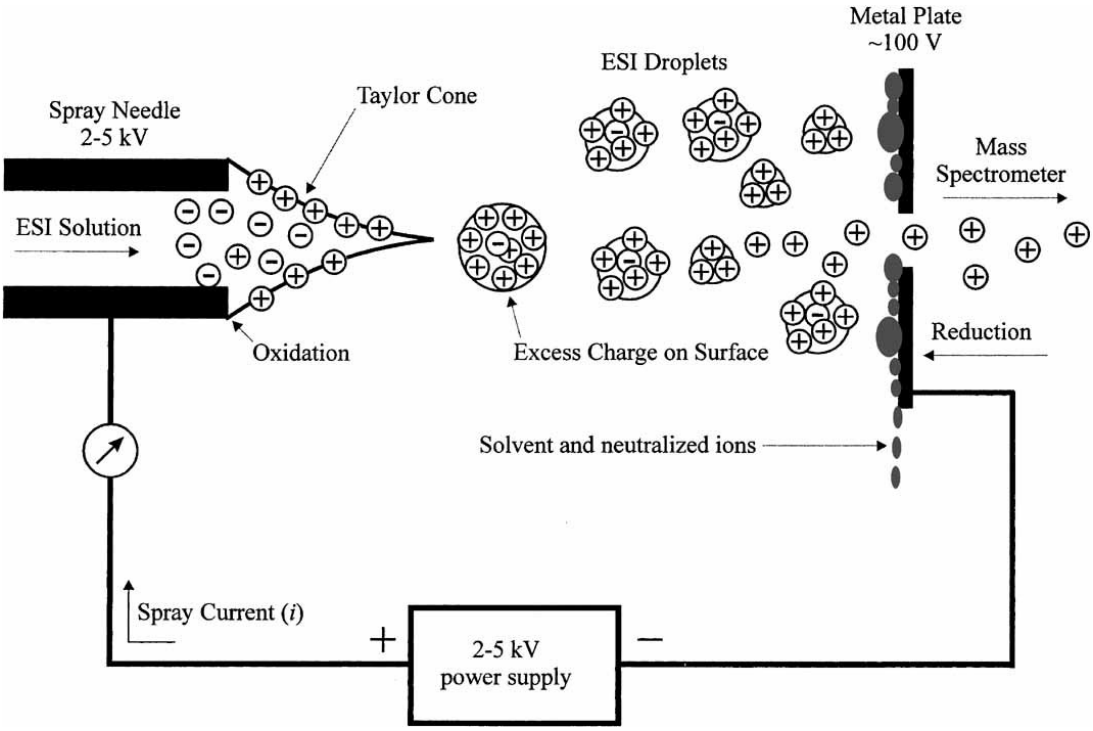

Figure 1.5 – *Schematic of the electrospray ionisation and the Taylor cone. Retreived from Cech and Enke (2001).*

ESI is a very powerful technique which brought a Nobel prize to the inventor John Fen in 2002 for the application of ESI to large biomolecules (Fenn et al., 1989). It is considered a soft ionization method that does not fragment the analyte molecules and keeps them intact for high throughput mass spectrometric analyses. It is widely used in many different types of mass spectrometry for analysing DOM due to its simplicity and

useability for a large number of analytes simultaneously (Oss et al., 2010). However, the ESI response varies significantly among different analytes in the same solution, where some analytes are more efficiently ionized than others, and some are not ionizable at all. The success of the analysis depends on the characteristics of the analyte, flow rate, applied voltage and surface tension of the solvent (Cech and Enke, 2001). For analysis of complex mixtures like DOM, therefore, optimizing the ESI parameters to improve the ionization performance is challenging.

1.1.3.3 Excitation and Detection

The ions generated in the ESI are accumulated in an ion trap and then transferred into the ICR cell, where a strong magnetic field is generated by superconducting magnets. Under a magnetic field, the motion of the charged ions becomes circular in a plane perpendicular to the magnetic field axis, and ions encounter a force called "Lorentz Force". The force axis, the motion of the ionized molecules and the magnetic field are perpendicular to each other by the left-hand rule (Fig. 1.6), and the angular frequency of circular motion is called cyclotron frequency.

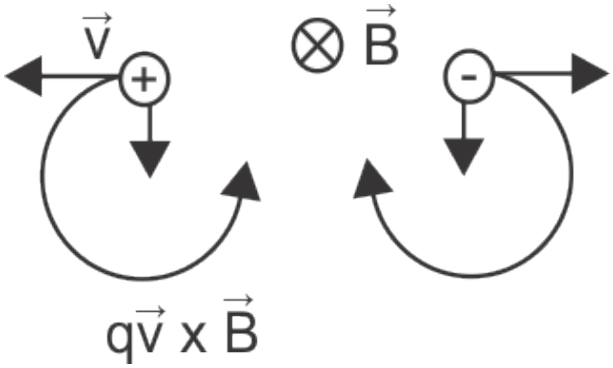

Figure 1.6 – *Representation of Ion cyclotron motion. Lorentz force (B) is perpendicular to the plane of the paper, and ions move in a circle as the component of charge (q) and velocity (v). Modified from Marshall et al. (1998).*

The Lorentz force (F) acting on a charged ion under the magnetic field:

$$F = m\frac{dv}{dt} = qv \times B = qvBsin\theta$$

where m is the ionic mass (kg), q is the charge (coulombs, C), v is the velocity (m s^{-1}), B is the magnetic field strength (tesla, T), and θ is the angle in degrees between the axis of the motion and the axis of the magnetic field strength. Since the ions move perpendicular to the axis of the magnetic field, the equation becomes:

$$F = qvB$$

The total charge on an ion is defined as

$$q = ze$$

where z is the number of charges and e is the charge per electron (coulombs, C).

Charged ions form an orbit with angular velocity ω (rad s^{-1}), where the cyclotron frequency f (hertz, Hz) is inversely proportional to the ions' mass to charge (m/z) ratio (1 Da = $1.66054 \times 10^{-27} kg$).

$$\omega = \frac{qB}{m}$$

$$f = \frac{\omega}{r} = \frac{qB}{2\pi m}$$

$$\frac{m}{z} = \frac{B}{2\pi f}$$

Around the cyclotron orbit, there are counteracting plates of detection and excitation, which trap the ions in a circular path. The excitation plates provide an electrical field with a brief application of ac voltage (Skoog et al., 2007). Ions absorb the energy when the frequency of the electrical field matches the cyclotron frequency. Then the velocity of the excited ion continuously increases until the electrical signal is terminated, as does the radius of its path without disturbing the cyclotron frequency (Skoog et al., 2007). Ions of different cyclotron frequencies (i.e., different mass to charge ratios) are not affected by the ac field. As the ions pass to the proximity of the detection plates, the

difference in voltage between plates can be measured as a function of time which provides time-domain data (Barrow et al., 2005). The time-domain data represent all the ions detected at the same time. Therefore a mathematical operation, Fourier transform, is applied to obtain frequency-domain data. The unique advantage of FT-ICR is that the mass to charge ratios are measured through the very small increment of frequencies which can be measured very accurately. Therefore. FT-IC MS provides inherently higher mass resolution and accuracy than other mass analysers (Marshall et al., 1998).

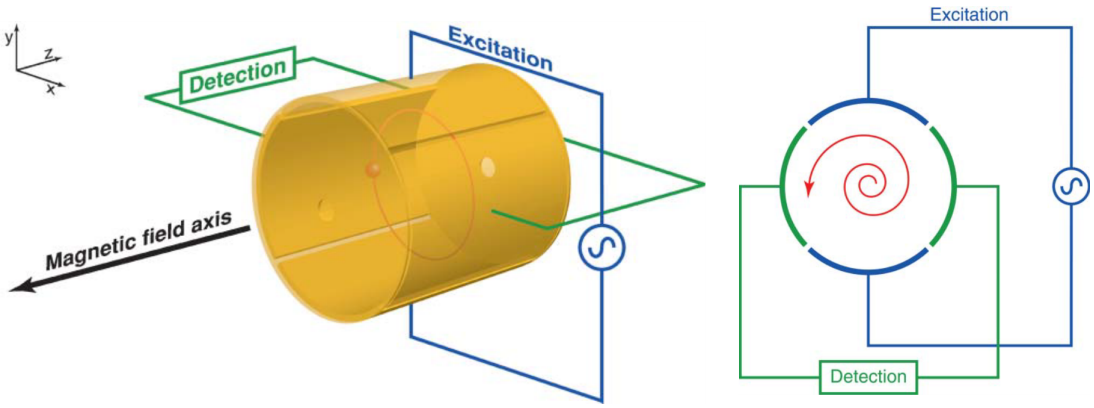

Figure 1.7 – *(Left) FT-ICR cell aligned with the magnetic field axis on the z-axis, excitation plates on the y-axis and detection plates on the x-axis. The orbiting ions are shown in red. (Right) A cross-section of cylindrical FT-ICR cell. The figures are retrieved from Barrow et al. (2005).*

1.1.3.4 Data acquisition and formula assignment

Once the mass spectra are obtained from the FT-ICR MS, two signal processing steps are applied: apodization and zero filling. Apodization refers to the smoothing of peaks at the spectra by removing artefact peaks adjacent to the real peaks that appear after the Fourier transform at the base of the spectrum. Zero-filling corresponds to adding zero-filled intervals to the transient, which results in more straightforward interpolation between the point in the frequency domain and improves the peak shapes (Scigelova et al., 2011).

After signal processing, noise filtration, calibration, and molecular formula assignments are carried out. The signal-to-noise ratio (S/N) is the ratio of peaks obtained from the analyte molecules to those originating from the instrument. For the noise filtration,

signals with lower peak intensity than the pre-assigned S/N were removed from the spectra. One common approach is to use a fixed S/N (e.g., 5-10). Depending on the expected precision, S/N threshold can be higher or lower, leading false-negative assignments in the former and false-positive assignments in the latter case. Another way of determining noise is to estimate the method detection limit by using repeated measurement of instrument blank or sample blank. In this case, there is no need to know about the analyte and its chemistry since the method detection limit and corresponding noise cutoff are estimated statistically for each analysis (Riedel and Dittmar, 2014).

Calibration of the mass spectra after the noise filtering is a common procedure, and there are several ways of calibration for FT-ICR mass spectra. Using an external mixture of calibrants with known peaks covering a similar mass range of the sample spectra is defined as external calibration and requires a dual spray source that DOM sample and calibrant are sprayed in alternating periods (D'Andrilli, 2009). On the other hand, internal calibration is conducted by peaks of known homologous methylene (-CH_2) series that cover the entire mass range of the sample spectra and are consistently found in most DOM samples (D'Andrilli, 2009).

After the calibration, a list of peaks is tabulated for formula assignments, with each peak having the information of m/z, intensity, peak resolution and S/N. Then, using a software algorithm, molecular formulas are estimated that correspond to each peak within a predefined error range (usually 1 ppm) and heteroatom combination (usually CHONSP). Peaks that do not have an acceptable error range are removed.

1.1.3.5 van Krevelen diagram and main biochemical classes of DOM

Various methods exist for analysing and visualizing lists of molecular formulas obtained from FT-ICR MS. The van Krevelen diagram (van Krevelen, 1950) is the most comprehensive and intuitive way to visualise FT-ICR MS data which significantly facilitates the information obtained from the assigned formulas (Kim et al., 2003). The van Krevelen plot is constructed with all assigned formulas using the atomic ratio of hydrogen to carbon (H:C) on the y-axis and oxygen to carbon (O:C) on the x-axis. This way, formulas obtained from different samples are easily compared, and compositional differences

are located. Furthermore, some major biochemical classes of compounds can be defined on the van Krevelen diagram by the ranges of O:C and H:C ratios.

FT-ICR MS resolves thousands of molecular formulas from a single sample without structural information. Formulas can be elements of metabolic processes, biochemical sensors, extracellular discharge or remnants of historical processes that resist degradation. Therefore, classifying formulas into several biochemical classes is an oversimplification. Moreover, traditional classification with distinct boundaries between molecular classes is often erroneous. An empirically derived metabolite map on the van Krevelen diagram and ^{13}C-NMR (nuclear magnetic resonance) spectroscopy based molecular mixing models suggest that molecular classes usually overlap and do not allow distinct boundaries on the van Krevelen diagram (Brockman et al., 2018; Hockaday et al., 2009; Rivas-Ubach et al., 2018). Therefore, descriptive classification based on formula characteristics (e.g., highly unsaturated O-poor to saturated O-rich) is chemically more precise and correct. Nevertheless, biochemical classification with approximate boundaries offers a better intuition of microbial processes and sources of DOM and provides an advantage for comparing samples and spotting functional differences.

Microbially derived, bioavailable fractions- lipids, proteins (more accurately peptides), and carbohydrates- are primarily classified above the H:C = 1.5 line and defined as labile DOM fractions (D'Andrilli et al., 2015). Gene expression and molecular characterization studies show that labile DOM consists of easily characterized low molecular weight compounds and can appear in many different chemical forms such as carboxylic acids, vitamins, amino acids, ATP, glycerol, fatty acids, nitrogen-containing metabolites taurine, choline, sarcosine, polyamines, methylamines, ectoine, one-carbon compounds such as methanol, simple biopolymers such as proteins, unbranched homopolysaccharides and number of lipids such as aliphatic hydrocarbons, aliphatic alcohols, ester terpenes and sterols (Hockaday et al., 2009; Moran et al., 2016; Repeta, 2015). Not all labile DOM contains nitrogen, but the bulk elemental composition of proteins (more accurately, peptides of 3 to 6 amino acid residues in the mass range of 300-800 Da) and amino sugars have N$\geq$ 1 (Hockaday et al., 2009). Up to 50 % organic carbon and 80 % organic nitrogen are incorporated in cells as amino acids, peptides and proteins (Repeta, 2015). Similarly, phytoplankton cells are rich in carbohydrates and together with pro-

teins and lipids, they are usually considered labile or semi-labile DOM and relatively more accessible for microorganisms.

Substances that are classified as lignins, tannins and carboxyl-rich aliphatic molecules (CRAM) are defined in the central part of the van Krevelen diagram (e.g., 0.5>H:C>1.5 and O:C>0.3). These are primarily refractory substances with high hydrophobicity; therefore, SPE works best on them. Van Krevelen diagrams of marine samples often have the highest peak density in this region. As the name also recalls, humic substances are either of terrestrial origin transformed with rivers and atmospheric depositions or modified from marine lipids, carbohydrates and proteins through extensive molecular transformation. Compared to soil and freshwater, marine-originated humic substances have lower aromatic and olefinic content, lower C/N ratio, and δ^{13}C value of 21-22 ‰ that often implies autochthonous sources (Repeta, 2015, and references therein).

The lower part of the van Krevelen diagram mainly consists of polycyclic aromatic compounds, black carbon, and unsaturated hydrocarbons. These are abundantly thermally altered compounds and highly refractory to microbial degradation. For marine DOM, thermal modification might stem from hydrothermal vents or other sedimentary heat sources (Dittmar and Koch, 2006; Dittmar and Paeng, 2009; Hertkorn et al., 2013). Otherwise, riverine inclusion of terrestrial black carbon and pyrogenic organic matter are souces of thermogenic DOM (Hertkorn et al., 2013). As the oxygen and hydrogen saturation decrease, molecules naturally have high double bond equivalency and aromaticity. The Aromaticity Index (AI) was suggested to identify the probability of the existence of aromatic structures (Koch and Dittmar, 2006). AI is a useful tool for classifying aromatic compounds in any sample and provides a hint for the general composition.

1.1.4 Methane in marine environments

Methane is the smallest and the simplest organic compound with a stable tetrahedral molecular geometry consisting of four hydrogens and a single reduced carbon. Methane is the most abundant hydrocarbon in the atmosphere and significant greenhouse gas that 25 to 32 times more potent than carbon dioxide in 100 years interval (Etminan

et al., 2016; Jain et al., 2000). Therefore, increasing concentration in the atmosphere may dramatically affect the Earth's climate and global warming (Intergovernmental Panel on Climate Change, 2014). While the anthropogenic activities elevate the net input to the atmosphere (35 % of anthropogenic greenhouse gas emissions (Hoglund-Isaksson, 2012)), oceans are usually regarded as net-zero emissions in the global warming scenarios as a source of methane (Hansen et al., 1997, 1998). Oceanic methane is considered in equilibrium with the atmosphere due to the several production/ consumption mechanisms mainly derived from natural biogeochemical processes.

The atmospheric equilibrium concentration of methane in the surface ocean is 3.2 nM based on Bunsen solubility coefficients at 6 °C and 34.8 salinity (Wiesenburg and Guinasso, 1979). However, methane is oversaturated most of the ocean surfaces and continental shelves (Bange et al., 1994; Conrad and Seiler, 1988). Concentrations ions tend to increase toward mixing layer and reaches its maxima in the mixed layer above the pycnocline (Reeburgh, 2007). Concentration of methane decreases with depth to reach uniform background concentrations of 0.18 nM in Pacific and 0.36 nM Atlantic Ocean below 2000 m depth (Charlou and Donval, 1993; Conrad and Seiler, 1988; Scranton and Brewer, 1978).

Ocean sediments comprise the major source of methane to the marine waters. Methane produced in sediments enters to the ocean through seeps, hydrothermal vents, mud volcanos or by direct diffusion from organic rich-anoxic sediments as either forming gas bubbles or emitting methane rich fluids (Reeburgh, 2007). There are various mechanisms that produce methane in the ocean sediments including microbial diagenesis of sedimentary organic matter, abiotic production through serpentinization reactions, leaks from near-surface petroleum sources, reactions in hydrothermal systems, and decomposition of clathrate hydrates (Reeburgh, 2007). In addition to the sedimentary processes, methane is produced in the surface ocean. The surface production of methane was initially thought to be mediated by the strictly anaerobic methanogens (the methane paradox) in the surface ocean that is saturated with oxygen (Reeburgh, 2007). Although the paradox is not fully resolved yet, studies implied that the methane production in the aerobic ocean might also stem from bacterial degradation of the organic matter (Repeta et al., 2016) or decomposition of methyl phosphonate (Karl et al.,

2008; Metcalf et al., 2012).

Despite all the sources, overall oceanic methane is undersaturated with respect to the atmosphere (Reeburgh, 2007) owing to two functional groups of microorganisms, aerobic methane-oxidizing bacteria (MOB) and anaerobic methanotrophic archaea (ANME). Accordingly, diffusing methane from the anaerobic layers of sediment is first utilized by the ANME and oxidized to bicarbonate along with the presence of an electron acceptor such as sulfate or nitrate during a reaction called anaerobic oxidation of methane (AOM) (Hinrichs and Boetius, 2003; Valentine and Reeburgh, 2000). At around 80% of sedimentary methane produced by methanogenesis is consumed by AOM in ocean sediments before reaching seafloor (Knittel and Boetius, 2009). Any methane that could escape from the AOM filter gets then oxidized aerobically at the aerobic layer of the sediment or in the water column by MOB through aerobic methane oxidation (MOx) reactions (Hanson and Hanson, 1996).

MOB has the unique ability to utilize methane as a major source of carbon and energy in all aerobic aquatic environments. The source of methane could be biogenic (e.g., a product of methanogenesis), thermogenic (e.g., thermal degradation of organic matter) and abiogenic (e.g., serpentinization of mafic rocks) seeping from the deeper layer of the sediments. During the reaction, methane is first converted to methanol and then formaldehyde mediated by an enzyme called methane monooxygenases (Hanson and Hanson, 1996). Formaldehyde plays a central role as an intermediate in catabolism and anabolism which is then further oxidized to carbon dioxide to gain energy up to 842 kj/mol (Reeburgh, 2007) or anabolized into cell material through two different enzymatic pathways (namely, Serine and RUMP) in three types of methanotrophs (Type I, II and III) (Hanson and Hanson, 1996). MOx is considered the final sink mechanism for the dissolved methane in the water column before reaching the atmosphere (Reeburgh, 2007) and, under suitable growth conditions (e.g., methane concentration, ocean currents, geological features acting as natural shelters), MOB can function so effectively that they can remove methane from the water column, entirely (Gründger et al., 2021; Steinle et al., 2015, 2017). Yet, MOx is not always linearly correlated with the methane concentrations and can be very sporadic despite high level of methane input to the water column linked to geomorphology and spatiotemporal variations in the MOB com-

munities (Gründger et al., 2021).

1.1.5 Sources of methane to marine environments

1.1.5.1 Cold seeps

Cold seeps are the point sources of hydrocarbon gases in marine sediments that is not associated with high temperature processes but originates mainly from dissociating gas hydrates or gas reservoirs that accumulate within the pore spaces of coarse-grained sediments (Judd et al., 2002). Seeping gas is predominantly consisting of methane ($\sim$ 99.7 %) (Pohlman et al., 2009) therefore they are also defined as methane seeps. Seeps occur along active and passive continental margins and from all parts of the oceans from shallow coastal regions to hadal depths and usually support rich biodiversity (Reeburgh, 2007; Vanreusel et al., 2009). Cold seeps in the Arctic Ocean are derived from different geological mechanisms but dissociating gas hydrates close to the limit of gas hydrate stability zones are thought to be the main source of biogenic methane release at the continental margins (Reeburgh, 2007; Westbrook et al., 2009). Seeping gasses usually form bubbles and ascend towards the sea surface. Along their trajectory towards the atmosphere, methane in the bubbles partly exchanges with other abundant dissolved gasses present in the water column (Jansson, 2018; McGinnis et al., 2006). Depending on the bubble size, depth of the water column, salinity, and water velocity major part of the seeping methane remains in the water column as dissolved gas and promote MOx nearby seepage areas.

1.1.5.2 Hydrothermal vents

Hydrothermal vents are one other source of methane to marine environments that emit methane together with varied composition of hydrothermal fluids that originated from magmatism and subseafloor hydrothermal circulation in different geodynamical settings from fast spreading (e.g., East Pacific Rise) to ultra-slow spreading ridges (e.g., Arctic Mid-Ocean Ridges) (Charlou and Donval, 1993; Konn et al., 2015). Vent methane, is usually but not ultimately characterized by abiogenic origin with heavier isotopic

composition (Whiticar, 1999) and derives from multiple sources including sea water ultramafic rock interactions (i.e., serpentinization), thermocatalysis of organic matter in high temperature systems and bacterial production in low temperature systems (Charlou and Donval, 1993, and references therein).

Hydrothermal methane does not form bubbles, but vent fluids, which spread to larger areas compared to cold seeps along with the buoyant plume venting from the hydrothermal source. When hot vent fluids meet with the much colder, stratified ocean waters, they are buoyant and begin to rise until reaching a density layer that the hydrothermal plume become neutrally buoyant (German and Seyfried, 2014). Hydrothermal plumes spread laterally with the ocean currents and continue to mix with ambient sea water along the trajectory of its dispersion. Elemental and molecular anomalies are used to trace original vent compositions from several to thousands of kilometers (Lupton and Craig, 1981) depending on their reactivities and interaction with ocean microbes (Ortmann and Suttle, 2005). By introducing vent associated microbial communities and hydrothermal originated elemental composition, hydrothermal plumes act as redox gradients that provide biogeochemical heterogeneity to otherwise homogenous deep ocean environments (Levin et al., 2016).

1.2 Motivation and objectives

Average air temperature has risen 2 to 3°C since the 1950s in the Arctic Ocean (AMAP, 2013). As a response to temperature increase, sea-ice extend has decreased (Meier et al., 2014; Olsen et al., 2011), and ocean waters have gotten warmer (Steele and Dickinson, 2016). An increase in water temperature potentially leads to the dissociation of methane hydrates (Berndt et al., 2014), elevates methane concentrations (McGinnis et al., 2006; Myhre et al., 2016; Westbrook et al., 2009) and modifies water column biogeochemistry (Findlay et al., 2015; Pohlman et al., 2009).

Methane migrates from the seabed into the water column and fuels the enzymatic MOx reactions as a final sink mechanism before reaching the atmosphere. Methane forms the base of a food chain from MOB and some chemolithotrophic symbiont bacteria to

higher trophic level organisms near cold seeps and hydrothermal vents independent of photosynthesis (Hanson and Hanson, 1996). MOB release extracellular enzymes (Hanson and Hanson, 1996), organic acids intermediates (Elvert and Niemann, 2008), cell lysis products (Kalyuzhnaya et al., 2013) and occasionally utilize carbon substrates other than methane (Dedysh et al., 2005; Theisen and Murrell, 2005). Therefore, a part of the MOB utilized methane potentially contributes to methane-associated DOM in the water column. In addition, a link between methanotrophy and primary production (seep fertilization) (D'souza et al., 2016; Pohlman et al., 2017) may further modify water column DOM composition. Biogeochemistry of the DOM in the Arctic Ocean has been investigated by several studies (e.g., Anderson and Amon, 2015; Hioki et al., 2014; Letscher et al., 2011; Osterholz et al., 2014), yet a detailed synthesis of methane-driven DOM modifications has never been documented before the articles attached to this thesis.

This thesis aims to identify and characterize the interactions between methane involving processes and DOM compositions in the water column of Arctic marine environments.

The individual objectives were:

1. To characterize DOM composition in the water column at different cold seep sites in the Arctic Ocean
2. To investigate methane triggered DOM modifications in relation to MOx and consequent microbial advances in controlled experiment
3. To investigate hydrothermal vents as a source of methane and characterize the specific effects of hydrothermal intrusions on the marine DOM cycle from sea bottom to sea ice
4. To investigate the roles of hydrophysical and biogeochemical properties in the Arctic Ocean in relation to methane involving processes and DOM modifications.

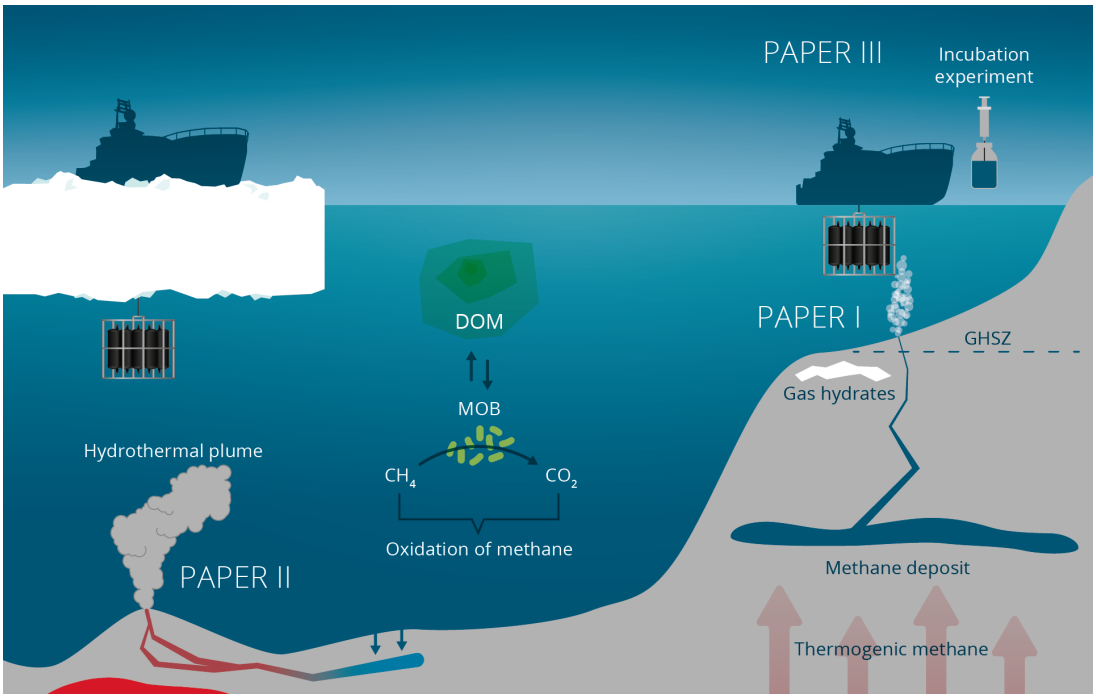

Figure 1.8 – *Summary of the overall objectives, general properties of the study sites and main approaches with the research papers.* Credit: Torger Grytå, UiT.

1.3 Study areas

The study sites were selected in compliance with our working group research agenda and planned scientific cruises. For Paper I, study sites were visited during the research cruises CAGE 2017-1 and 2017-2. Our primary approach was to cover as many areas as possible that were previously visited, and seepage activities were assessed. Selected stations were in (i) Prins Karl Forland (PKF) region at the continental shelf of Svalbard, (ii) Vestnesa ridge and Yermak Plateau (iii) Storfjordrenna and Pingo site at the southern tip of Svalbard, and (iv) Olga basin in the central Barents Sea. For Paper II, Aurora hydrothermal vents at the ultraslow spreading Gakkel ridge was sampled. The cruise was part of an exploration campaign that was aiming to investigate the role of Arctic Ocean and the Gakkel ridge in biological connectivity amongst the ocean basins and global biogeography of the chemosynthetic ecosystems. For Paper III, Norskebanken flares were visited and sampled for the incubation experiment. The area was previously characterized as an active methane seepage area in the south of Yermak Plateau (North of Svalbard).

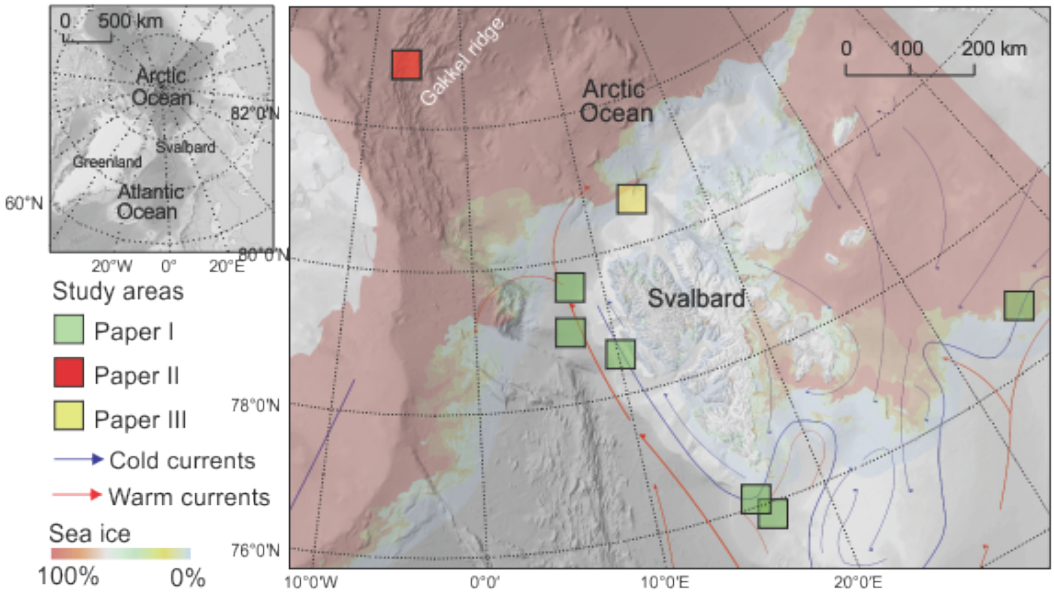

Figure 1.9 – *Studied areas, surface currents and sea ice concentrations.*

PKF is characterized by active methane seepages at the continental margin of western Svalbard and at the shallow shelf west of PKF Island. Here, numerous gas flares ($\sim$ 200) at 80-90 m depths were identified by hydroacoustic surveys (Sahling et al., 2014; Silyakova et al., 2020). Methane and MOx measurements were carried out for consecutive years (Gründger et al., 2021; Sert et al., 2020; Silyakova et al., 2020). The area is mainly influenced by the Atlantic originated West Spitsbergen Current and considered one of the natural laboratories for the bottom water warming related methane release and seasonality in the Arctic Ocean (Ferré et al., 2020a; Graves et al., 2015).

Recently discovered gas hydrate pingos (GHPs) in the Storfjordrenna region at the southern tip of the Svalbard archipelago are characterized by intensive cold seep activity through the 500 m range dome like structures (Serov et al., 2017). Here, unlike the PKF, methane release is localized to the GHPs and macroscopically visible biofilms in the sediment matrix are associated with the ANME (Gründger et al., 2019). The hydrography here is also mainly influenced by the Atlantic waters and fronted by Arctic originated waters at the deep layers. Three GHPs, at around 350 m depth and two stations at 1 km south of the GHP region were sampled and assessed in Paper I.

Vestnesa ridge features deep sea cold seeps where sub-seafloor fluid flow formed well-

described chimney structures (Bünz et al., 2012; Panieri et al., 2017). Fluid flow found to be rising ∼800 m above the seafloor from the chimneys with in the ∼700 m in diameter and ∼10 m deep pockmarks and extensive authigenic carbonate deposits represent a prolonged methane carbon sink that prevents much of the upward methane release (Panieri et al., 2017). Here the water column is characterized by the Atlantic waters at top 500 m which pass through Fram Strait into the Arctic Ocean and deep waters underneath (Rudels et al., 2000).

Yermak Plateau is located on the eastern flank of the Fram Strait and shape the northwestern part of the Barents Sea shelf. The area is enclosed by the Arctic Ocean and the Svalbard archipelago with water depths around 600-800 m and less than 500 m in the southernmost part (Alexandropoulou et al., 2021). Yermak Plateau serves as a topographic obstacle for passage of warm Atlantic Waters into the Arctic Ocean along with the marginal ice zone that function as a transition region between open water and dense ice cover characterized with enhanced tidal variability (Fer et al., 2015). For the incubation experiment (Paper III), seawater was collected from Norskebanken cold seeps. The survey was aimed to discover methane seepages on Norskebanken offshore northern Svalbard at the south of Yermak Plateau where average water depth is less than 300 m. This area is a part of Yermak plateau and is known for the giant Hinlopen/Yermak Megaslide event that forms a glacier fed, siliclastic (terrigenous material formed by weathering) continental margin (Geissler et al., 2016). The water mass circulation in the area is characterized by the North Svalbard Current which is originated from West Spitsbergen Current that carries warm Atlantic Waters to the Arctic Ocean (Ferré et al., 2020b).

Olga basin is one of the study sites that was sampled along an exploration cruise to the central Barents Sea and West Sentralbanken. We collected samples from three stations above the hydroacousticly located active cold seeps. Here water depth was between 150-160 m and the water column was entirely occupied with Arctic waters.

The Aurora hydrothermal vent system was the only hydrothermal system studied at this study. The hydrothermal system was near to the summit of a seamount with around 200 m height and located at the bottom of 4000 m depth water column. Here, hydrothermal intrusion manifest itself with a black smoker plume from chimneys that

contain high amounts of methane ($10^{4\text{-}5}$ × background) (Boetius, 2015; Edmonds et al., 2003). Aurora hydrothermal field is in the westernmost segment of the ultraslow spreading Gakkel Ridge and a part of a series axial volcanic ridges and smaller volcanic mounds that rise up hundreds of meters above the axial floor depth (Bünz et al., 2020; Michael et al., 2003).

1.4 Methods

1.4.1 Hydro-physical and biochemical parameters

1.4.1.1 Water sampling and storage

Biogeochemical characterization of the water column was conducted by sensor-based profiling and discrete water sampling in all stations. A rosette system equipped with airtight Niskin bottles and a CTD (Conductivity Temperature Depth) profiler aligned with oxygen, turbidity and chlorophyll sensors was used on every sampling occasion. Samples for methane concentration, stable C isotope ratios of methane ($\delta^{13}CH_4$: Paper II) and MOx rates (Paper I and III) were collected immediately after the CTD rosette was recovered onboard. Then, 4 × 1350 mL of acid-washed glass bottles were subsampled for DOM, DOC, nutrients, and other parameters. If immediate handling were not possible, these bottles were stored at 4℃ at dark and processed within six hours.

1.4.1.2 Sensor based measurements

Sea-Bird 911 plus CTD was used to measure temperature, salinity, pressure, and conductivity with accuracies of 0.001 ℃, 0.002, 0.3 dB and 0.003 S/m, respectively. CTD was coupled with SBE 43 dissolved oxygen sensor (0.01 ml/l resolution in 0-15 ml/l range), Wet Labs ECO chlorophyll fluorometer (excitation/emission: 470/695 nm, sensitivity, and limit of detection 0.01 µg/l) and Wet Labs C-Star beam transmissometer for measuring turbidity. In Paper II, Lowered Acoustic Doppler Current profiler (LADCP) was also mounted on the CTD rosette to determine the water currents' direction and

velocity. When LADCP was mounted on the rosette, the real-time positioning of the rosette was determined by high precision acoustic profiler (HiPAP, Kongsberg Maritime). EK60 single beam echosounder was used on all cruises to locate active seeps in the studied sites.

1.4.1.3 Analyses of seawater

Dissolved methane was quantified using headspace gas chromatography (ThermoScientific, GC Trace 1310, FID Detector, MSieve 5A). Hydrogen gas was used as a carrier gas, and the oven temperature was set to 150 ℃. The method's detection limit was 1 ppm with 5% standard deviation, and the reproducibility of measurements was controlled with 2 ppm and 100 ppm methane-containing air standards. Dissolved methane concentrations in seawater (nmol/l) were calculated from headspace concentrations using Boyle's law of ideal gas, Henry's law, and Bunsen solubility coefficients as a function of temperature and salinity (Wiesenburg and Guinasso, 1979). Methane oxidation rates (MOx) were determined by ex-situ incubations of tritium labelled methane in Paper I and Paper III, as previously described elsewhere (Niemann et al., 2015; Steinle et al., 2015). In Paper I, samples for MOx were taken as hexaplicates, amended with 10 µl, 50 pmol C^3H_4/N_2 (25 kBq) and incubated for 72 hours. In Paper III, samples were taken quadruplicates, amended with 5 µl, 50 pmol C^3H_4/N_2 (18 kBq) and incubated for 48 hours. In both cases, incubations were carried out at in-situ temperatures in the dark. Activities of $^3H_4$ and reaction product of ^3H_2O were measured by a liquid scintillation counter, and MOx rates were calculated by assuming first-order reaction kinetics (Reeburgh, 2007) and rate constant (k_{MOx}), which was corrected for tracer turnover in killed controls.

The concentrations of nitrate, phosphate, silicate, ammonium, and total phosphorus and total nitrogen following persulfate oxidation were measured with a segmented flow nutrient analyzer based on colourimetry. The detection limits and precisions are 0.5 ±0.1 µM for nitrate, 0.06 ±0.01 µM for phosphate, 0.4 ±0.1 µM for silicate and 0.01 ±0.01 µM for ammonium. Concentrations for dissolved organic nitrogen and phosphorus were calculated by subtracting dissolved inorganic nitrogen (nitrate+nitrite+ammonium) and phosphate concentrations from total nitrogen and total phosphorus, respectively.

DOC concentrations were determined with a high-temperature combustion technique using a total organic carbon analyzer (Qian and Mopper, 1996). The method's precision and accuracy were controlled by deep-ocean reference samples obtained from Hansell Laboratory (University of Miami). Samples were injected three times, and the average standard deviation of the method was 1.2 % for 54 DOC samples.

Isotope ratio mass spectrometry was used for the isotopic compositions of dissolved organic carbon (δ^{13}C-DIC) and oxygen in water (δ^{18}O-H_2O). $\delta^{13}CH_4$ was measured with a cavity ring-down spectrometer. Per mil deviations for all isotopic values were calculated against the international standards of Vienna Pee Dee Belemnite, Vienna Standard Mean Ocean Water, Greenland Ice Sheet Precipitation and Standard Light Antarctic Precipitation.

1.4.2 FT-ICR MS analyses

FT-ICR MS was the primary method for the characterization of DOM in all the research papers included in this thesis. Instrumental analyses were carried out in National High Magnetic Field Laboratory (NHMFL, FL, USA) with a custom-built 9.4 T FT-ICR MS in the Paper I and 12 T Bruker SolariX FT-ICR MS (Bruker Daltonics, Bremen, Germany) in the University of Eastern Finland in Paper II and III. Instrumental setups, analysis conditions and methodology for the formula assignments are given in corresponding papers and explained as follows.

For each sampling occasion in Paper I and Paper II, 1 L of samples were filtered by pre-combusted (450 ℃, 5 h) 0.7 µm pore-sized glass-fiber filters (Whatman GF/F). In Paper III, 1 L samples were filtered by 0.2 µm pore-sized sterile DNA filters (Millipore Sterivex), and filters were collected for microbial composition analysis. After the filtration, samples were acidified to pH 2 by concentrated hydrochloric acid solution (37 % w/w) and extracted by styrene polymer type cartridges (500 mg, 6 mL, PPL, BondElut, Aligent Technologies). The extraction method was adapted from Dittmar et al. (2008), except that the final elution volume was modified to 2 mL of methanol. Four method blanks were obtained by following the same extraction protocol with MilliQ water for each paper. Final eluates of samples and blanks were stored at pre-combusted amber

vials at -20℃ until analysis except from 2-3 days transportation from UiT to the final location of analysis. Samples were directly injected to FT-ICR MS for Paper I and after 1:10 dilution (v/v) with methanol for Paper II and Paper III based on the laboratory's sample handling procedures. Therefore, considering the DOC concentrations obtained from samples, the final DOM samples in methanol solutions had an average carbon content of 341±91 mg/L for Paper I and 34±7 mg/L for Paper II and III.

Both negative and positive ESI sources were used for the ionization samples. Ions generated by the ESI were accumulated in hexapole/octupole ion trap and transferred to ICR cell for trapping excitation and detection. Mass spectra were generated following a Hanning apodization, Fourier transform and magnitude calculation. NHMFL Predator (v 4.2.0) and Bruker DataAnalysis (5.0 SR1) software were used for initial spectral post-processing and internal mass calibration. Peak lists were generated within a threshold of signal-to-noise ratio (Table 1.1) and internally calibrated with commonly known DOM methylene (-CH_2) compounds within the given spectral ranges (Table 1.1).

Molecular formula assignments from peak lists were conducted by PetroOrg software in all papers (Corilo, 2014), including all possible naturally occurring monoisotopic molecular combinations of C, H, N, O and S within the ranges given in corresponding papers (Table 1.1). Formula confirmation was based on individual monoisotopic mass spectral peaks (mass error <1 ppm, double bond equivalent <50) and homologous series inclusion (>3). After the initial assignment, molecular classes by heteroatom contents were visually inspected for mass errors, and homologous series with systematically high errors were removed. Therefore, apart from the initially given threshold, much lower mass errors (ca $\leq$ 0.2) were achieved practically for the assigned formulas. Sodium (Na) and chlorine adducts (Cl) were also considered for positive and negative modes, respectively. Isotopic peak patterns were controlled for duplicated molecular formulae that can cooccur with adducts, and formulas that do not fit the pattern were removed. In all papers, formulas compiled from four method blanks were subtracted from samples.

For each formula, relative abundances (intensities) were considered as is calculated by the PetroOrg molecular formula assignment algorithm, where ESI abundances were rescaled as proportions of the most abundantly ionizable peak. Occasionally, impurities suppress the baseline of the spectrogram and leave the most abundant peaks

Table 1.1 – *Instrumental configurations and data accusation parameters for FT-ICR MS analysis in papers.*

	Paper I	Paper II and III
Instrument	Custom-built, 9.4 Tesla	Bruker SolariX, 12 Tesla
Flow rate	0.5 µL/min	2 µL/min
Number of co-added scans	50	100
Signal-to-noise ratio	S/N_{RMS} >6	S/N >5
Acceptable mass error	<1 ppm	<1 ppm
m/z range of the calibration standards	200-900 Da	150-2000 Da
Allowed molecular combination	$^{12}C_{1-100}{}^{1}H_{1-200}{}^{14}N_{0-2}$-$^{16}O_{0-50}{}^{32}S_{0-1}{}^{35}Cl_{0-1}$-$^{23}Na_{0-1}$	$^{12}C_{1-100}{}^{1}H_{1-200}{}^{14}N_{0-4}$-$^{16}O_{0-30}{}^{32}S_{0-2}{}^{35}Cl_{0-1}$-$^{23}Na_{0-1}$

unassigned. Since abundant unassigned peaks downsize the relative abundances of other assigned peaks, relative abundances were ignored in some cases, and only presence/absence evaluation was considered. Assigned molecular formulas generated for each sample at positive and negative ion modes were merged into a single molecular formula list for further analysis. In the case of duplicated formula based on the CHNOS combination, relative abundance obtained from the negative ESI was considered. Relative abundance values of combined lists were considered only in the diversity index calculation in Paper I and Paper II and the Bray-Curtis dissimilarity matrix in Paper II. Otherwise, combined formula lists of DOM formulas were considered as binary data (presence/absence) in papers.

Biochemical characterization of DOM samples was conducted from the combined formula lists by obtaining percentages of heteroatom contents and H:C versus O:C atomic ratios. Four biochemical compound categories were considered based on the ranges of H:C and O:C ratios: (i) lipid- and protein- like, (ii) carbohydrate- and amino-sugar-like, (iii) unsaturated hydrocarbons and condensed aromatics, (iv) lignin- and tannin-like. Boundaries for these categories were modified from previous studies (Hockaday et al., 2009; Hodgkins et al., 2016). For calculating molecular class percentages, the number of formulas in the given class was divided by the total number of formulas ob-

tained from the sample and multiplied by 100. Similarly, percentages of heteroatoms (e.g., CHO, CHON, CHONS, CHOS) were calculated by the number of formulas obtained from each category. In Paper I, samples are also interpreted with percentages of formulas above the molecular lability boundary (i.e., H:C $\geq$1.5) (D'Andrilli et al., 2015).

Multivariate statistical analysis methods were used to evaluate DOM composition data in all the papers. First, dissimilarity matrices were constructed using corresponding indices (Jaccard in Paper I and Paper III and Bray-Curtis in Paper II). Then, ordination analyses were conducted to generate ordination plots by using statistical approaches. Nonparametric multidimensional scaling (NMDS) is one of these approaches used frequently in DOM literature (e.g., Kellerman et al., 2015; Kujawinski et al., 2016; Longnecker, 2015; Osterholz, 2014; Sleighter et al., 2010). NMDS points out the variation between samples. Such as, samples with similar compositions are grouped closer in the ordination plot, and the closer the distances between samples have more similar the compositions (see Paliy and Shankar, 2016). Using NMDS allowed for identifying the compositional differences between samples in Paper I. The NMDS analysis is based on the dissimilarity matrices constructed from binary (presence/absence) data (Jaccard, 1912). Another approach was the principal coordination analysis (PCoA). PCoA is especially convenient when the number of samples is insufficient to be evaluated with the NMDS (Oksanen, 2018). The main reason is that NMDS is a nonmetric and iterative calculation and reorients the ordination plot until minimum stress is obtained. Stress value for the NMDS can be expressed as $s^2 = 1 - R^2$ where R^2 is the linear fit representing correlation between fitted values and ordination distances (Sibson, 1972). When the number of samples is scarce, R^2 approaches 1 rapidly and stress becomes nearly zero. PCoA, on the other hand, provides unique analytical result each cases and the fixed number of ordination axes determined by the number of the samples.

1.5 Summaries of papers and concluding remarks

1.5.1 Hypotheses on methane and DOM interaction - Paper I and Paper III

The main hypothesis in this thesis was that methane driven microbial processes alter the molecular composition of DOM with elevated microbial activity and consequent discharge of metabolic products, cell excretes and organic intermediates. In seep sites and hydrothermal vents, DOM modifications may have distinct molecular level signatures across the water column and even alter ecosystem dynamics which may further modify DOM composition.

To test our hypothesis, we first investigated the water column biogeochemistry near active methane seeps at six different sites and 18 seep and non-seep stations. Each site had different hydrographic settings, biochemical characteristics and bathymetric features. Samples were taken at discrete water depths at selected stations and analyzed for methane related parameters (methane concentrations and MOx rates), biochemical properties (nutrients, DOC, Chl$a$) and DOM molecular composition.

Obtained data revealed that DOM compositions were associated with the spatial distribution of active seeps. DOM compositions were more labile, heterogeneous and had higher chemical diversity and lipid and protein-like compositions in samples collected from seep stations compared to samples from non-seep stations. Compositional differences between seep and non-seep DOM were most significant in the Prins Karl Forland region, where the seep influence was most substantial, and the water column was shallowest.

Investigation on varying methane sources and consequent differences allowed us to characterize biogeochemical properties in different seep sites. However, it had one major drawback that concurrent processes (e.g., water currents, nutrient dynamics) and coexistence of many different microbial consortia were complex and did not reveal any direct correlation between measured parameters and DOM compositions. We concluded that compositional differences might have been associated with several mechanisms

such as MOB derived DOM, seep-driven microbial modifications, or direct seepage of sedimentary DOM. However, the dynamic hydrography and varied water column characteristics of the study sites did not allow us to be conclusive about the exact role of MOx in DOM modifications. An incubation experiment was suggested to identify underlying mechanisms further, which led us to Paper III.

The main approach of Paper III was to reassess previous observations in a controlled laboratory experiment to be able to attribute compositional changes to experimental conditions. Seep and non-seep samples were incubated in methane amended and unamended conditions under the assumption that the MOx activity alters DOM compositions in seep environments through bacterial production and decomposition. Samples were collected before and after incubations for microbial composition analysis along with the DOM composition analysis to trace how the natural microbial community reacts to elevated methane concentrations and changes in MOB associated communities. However, DNA analyses were delayed and planned for later assessment. FT-ICR MS analyses revealed that DOM composition at the seep site was more diverse and heterogeneous than at non-seep sites under initial conditions. However, at the end of three days of incubation, DOM composition in methane-amended non-seep incubations shifted towards seep-like composition. I.e., the number of formulas increased, and the composition changed into more diverse and heterogeneous. Similarly, molecular formulas associated with hydrogen saturated aliphatic compounds and lipid and carbohydrate-like compositions displayed opposite trends between amended and unamended samples. The overall composition of non-seep methane amended samples was modified to become more similar to seep initial and seep amended samples. We showed that elevated methane concentrations and concurrent MOx activity influenced both production and consumption of DOM. I.e., when methane is available, MOB have an advantage over other organisms and proliferates and modifies DOM composition in a similar way. However, from an ecophysiological perspective, we also suggest that MOB might be active at a molecular level, and heterotrophic bacteria and eukaryotes might have the primary control on microbial processes and DOM compositions.

Taken together, the results from Paper I and Paper III showed that there is an interaction between methane-triggered processes and DOM composition in cold seep marine

environments. We suggest that there is a microbial mechanism triggered by methane oxidation, which also modifies DOM towards a more labile, chemically diverse and heterogeneous composition. MOB is possibly the principal agent and facilitator of this mechanism; however, we could not rule out the potential role of heterotrophic bacteria and other microbial consortia.

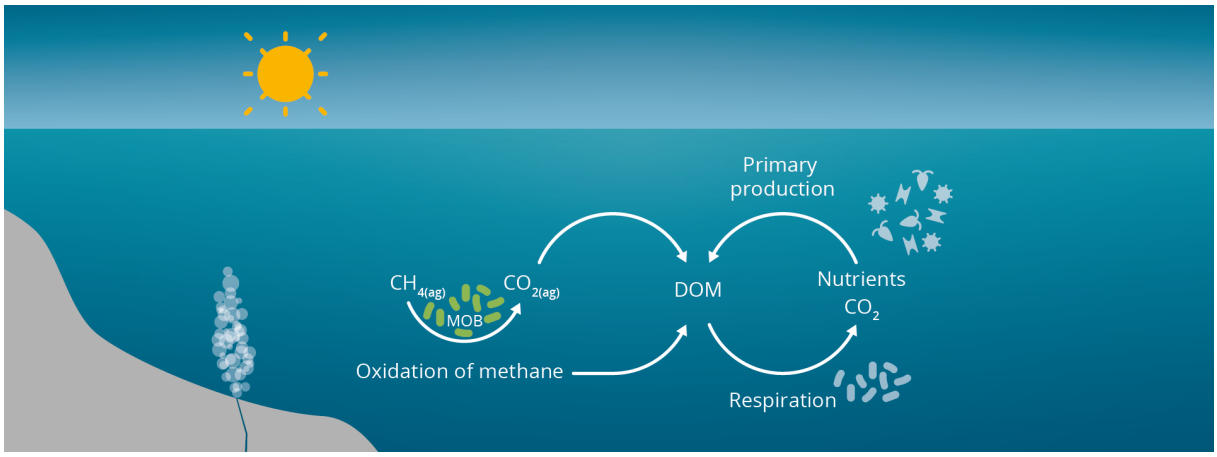

Figure 1.10 – *Routes of interaction between methane oxidation and the DOM cycle in the oceans.* Credit: Torger Grytå, UiT

Three possible mechanisms can explain DOM alterations by considering the interactions between methane, MOB, MOx, and DOM. First, DOM is modified by MOB along with the consumption of methane during chemical reactions, such as cell synthesis, reproduction, and ATP production. Second, MOB triggers some other microbial interaction while using methane during MOx, and these simultaneous mechanisms alter DOM (e.g., MOx coupled denitrification). Third, an indefinite combination of the former two where methane initiates a food chain in the ecosystem by providing a new energy supply to the system from methane oxidation with a maximum yield of 842 kJ/mol CH_4 (Lee et al., 2019; Reeburgh, 2007). The ability of MOB to convert methane into organic compounds has been previously described (Elvert and Niemann, 2008); however, the metabolic pathways for the synthesis of organic compounds and ATP producing assimilatory routes are unknown. Similarly, excreted compounds from cell lysis or starvation responses in cultures are not described (Kalyuzhnaya et al., 2013). Naturally, oxidation of methane by MOB is a carbon fixation mechanism in which methane, as the simplest form of organic matter, is utilized and transformed into more complex cell material. From this perspective, the consumption of methane leads to the production of higher

forms of organic matter and facilitates the functioning of the ecosystem and the food chain. Heterotrophs utilize allochthonous and autochthonous DOM as sources of carbon and energy, and MOB would be an important diet for zooplankton or other upper trophic level organisms (Bastviken et al., 2003; Brankovits et al., 2017). Therefore, considering the overall mechanisms and pelagic food web cycles triggered by methane, it might be possible to consider DOM as a source to the system as well as the product in seep environments.

In addition to the microbial community perspective, there is a hydrological significance of methane release in cold seeps. As methane seeps from the sediment forms bubbles, which rise throughout the water and upwell some nutrients to the upper layers (D'souza et al., 2016). Additional nutrients may be especially important and influential at depths exceeding 1000 m, where there is a strong gradient in nutrient concentrations between the bottom and the surface layer. The transport of methane with the rising bubbles may also trigger the above mentioned cycle in the upper layers.

In cold methane seeps, the amount of methane utilized by MOB is determined by the size and activity of the communities (Steinle et al., 2015), which are controlled by nutrient and redox dynamics, hydrographic conditions, site-specific geographical features and seasonal changes (Gründger et al., 2021; Steinle et al., 2015). Therefore, in seep sites, the DOM modifications in relation to methane input are possibly a function of all these factors.

1.5.2 Distribution and composition of DOM in hydrothermal vents – Paper II

DOM compositions in hydrothermal fields show discrepancies compared to the general deep ocean DOM composition. Two main mechanisms can be attributed to these discrepancies. The first mechanism is related to hydrothermal circulation, in which cold seawater migrates into the crust through open fissures and gets heated to extremes of temperature (Simoneit et al., 2004). Due to continuous exposure to high temperatures and low pH, DOM is modified to a highly aromatic, unsaturated, oxygen-poor petroleum-like composition during hydrothermal circulation of cold deep seawater

(Hawkes et al., 2015; Rossel et al., 2015, 2017). The second mechanism is related to hydrothermal fauna, which is ultimately sustained by chemotrophic production fueled by a mixture of reduced chemical compounds such as methane, hydrogen and hydrogen sulfide emitted from the vents (Levin, 2005; McCollom et al., 1999; Petersen et al., 2011).

Our hypothesis for this paper is that these two hydrothermally derived mechanisms modify DOM during hydrothermal processes, and corresponding modifications affect larger areas along with the spreading buoyant and non-buoyant plume emitted from the hydrothermal vents. We investigated the vertical distribution of DOM compositions at three hydrocast stations near Aurora hydrothermal vent field in ultraslow spreading Gakkel Ridge in the Arctic Ocean. The study area was characterized by vigorously venting black smokers, sulfide mounds, bacterial mats, sediments of hydrothermal origin and benthic communities typical for hydrothermal vent ecosystems (Bünz et al., 2020). Sea ice and the upper 1000 m of the water column were also sampled to investigate the DOM composition of the upper layers and surface ocean- sea-ice interactions.

We show that the displacing plume layer carried thermally degraded DOM compositions to a distance from the vent, characterized by a lower number of formulas, molecular diversity, average abundance, and percentages of formulas assigned in lipid and protein-like molecular class. DOM compositions had a higher number of formulas, molecular diversity, and carbohydrate-like class percentages at sites with higher vent-related biological imprints and lower influence from the plume dispersion. Hydrothermal vents emanate methane with hydrothermal fluids and vent originated thermogenic methane reaches a large area along with a plume layer which might trigger a series of consecutive changes.

Hydrophysical and biochemical properties on the top 1000 m layer mainly reflect vertical changes in primary production, atmospheric gas exchanges, riverine influences and water mass distributions. The water column was relatively uniform below 2000 m. DOM composition in sea ice was markedly more labile, contained high lipid-like percentages and had low molecular weight averages than the surface ocean suggesting selective transport of DOM during formation and the new production of ice algae.

1.5.3 Advantages and limitations of FT-ICR MS on DOM analysis

One novelty of this study was identifying the composition of dissolved organic matter in relation to methane-driven modifications with ultrahigh-resolution mass spectrometry. In this regard, FT-ICR MS provided the highest resolution by identifying thousands of molecular formulas in a mass range of 200 to 1000 Da and a tremendous ability to resolve DOM modifications along with ecosystem changes. However, ecosystem processes and related changes in the unconstrained water column are so complex that they often imply more than one reason for any modifications. Although methane oxidation is very strong in seep areas, it may still be less influential than the other seasonal and spatial variations, such as hydrography, primary production, bacterial regeneration, upwelling and diel vertical migration. Furthermore, in many cases, the molecular scale information obtained by FT-ICR MS is not parallelly observed in other parameters describing the environmental conditions since the sensitivity of other measurements is often not good enough to explain small molecular trends. For instance, the limit of detection for DOC is about 2 µM (Qian and Mopper, 1996). However, FT-ICR MS can detect DOM metabolites in seawater with picomolar level concentrations (e.g., Johnson et al., 2017). Therefore, spatial variations of DOM compositions should be supported by appropriate, high-resolution analyses such as isotopic tracers, specific molecular investigations, and microbial compositions.

DOM comprises molecules of all ranges of size and complexity, from small constituents such as amino acids and simple sugars to high molecular weight complex biopolymers such as proteins and polysaccharides. Among these, a portion of DOM cannot be detected by ESI FT-ICR MS analysis with SPE extraction. The limitation comes from the reactivity, size, and polarity of the analytes. E.g., amino acids, small sugars and short-fatty acids usually cannot escape from the rapid bacterial degradation until detection and, therefore, are not usually concentrated in the final analyte. Second, highly polar, hydrophilic substances do not restrain on SPE and are washed away during cleaning steps. Any procedure that increases the recovery of these substances also increases the salt content and lowers the analytical performance for all molecules. Third, molecules bigger than 2000 Da cannot be assigned within a given confidence

level because the isomers for any detected mass increase rapidly with molecular weight (D'Andrilli, 2009). Given that, SPE-DOM detected by FT-ICR MS is predominantly composed of semi-labile to refractory compounds with moderate polarity and low molecular weight (LMW<1000 Da). Nevertheless, LMW, semi-labile and refractory DOM correspond up to 80% of the DOM pool (Hansell, 2013; Ogawa and Tanoue, 2003), and FT-ICR MS detection of SPE-DOM is still unrivalled in elucidating the marine DOM characteristics.

ESI is the most common ionization technique for analyzing marine DOM with FT-ICR MS. It has a significant advantage due to its sensitivity, specificity, and simplicity. It is efficient at ionizing molecules with polar nitrogen and oxygen-containing functional groups and does not fragment large molecules. However, ionization efficiency varies greatly with different analytes, even if they have the same concentration within the solution. Therefore, FT-ICR MS analysis of marine DOM is considered so-called semi-quantitative which allows sample-to-sample comparison but does not perform best in molecular basis quantification. One improvement to handle this might be the using internal standards of various types of functionalities to access the relative ionization performances of molecules and molecule groups. Derivatization can also be a good alternative for improving ionization performance for specific analytes that are known to ionize weakly with ESI (Cech and Enke, 2001; Cho et al., 2015; Koivusalo et al., 2001; Oss et al., 2010).

Four biochemical compound classes were considered based on the given boundaries of H:C and O:C atomic ratios in van Krevelen diagram. The main motivation behind this was to prevent overgeneralization of the compound classes by separating them into very elaborately defined boundaries. On the contrary, molecular formulas were roughly classified and overall lability was assessed. This brings a consented bias for the interpretation of the results and often oversimplifies the ecosystem functions. However, great caution has been taken to use appropriate language regarding the known bias of using biochemical classes and improper interpretations of the chemical compositions of the samples was avoided.

Both negative and positive ESI used to improve the data extent in this thesis. Negative ESI is known to perform well for marine DOM analysis and more frequently applied in

studies. However, positive ESI has provided a significant improvement to our data, especially on labile compositions and N-containing compounds which are proxies for a relatively recent production (Sipler and Bronk, 2015). To carry data extent even further, atmospheric pressure photoionization (APPI) can be applied. APPI is less susceptible to chemical noise from solvents and salts and therefore has lower ion suppression from the matrix effects (D'Andrilli et al., 2010, and references therein) which can contribute to molecular composition analysis of both polar and non-polar substances (D'Andrilli et al., 2010; Hockaday et al., 2009).

Extensive operation and maintenance procedures and the time-intensive nature of data assessment usually limit the instrument times allocated for researchers and hamper using replicates of samples to improve accuracy and peak reproducibility. Furthermore, analysis methods and acquisition procedures vary significantly between the laboratories. What is actually obtained by FT-ICR MS largely depends on the analyst's approach and the causal evaluation of researchers (D'Andrilli et al., 2020). Recent attempts to standardize analysis procedures (Hawkes et al., 2020) and open-source software-based data assessment routines (Merder et al., 2020) might allow reproducible and internationally recognized analytical results.

1.6 Future perspectives

This thesis comprises the first attempt to resolve DOM composition in relation to methane-driven processes in the Arctic Ocean. We showed that DOM is modified in methane-receiving marine environments with a significant correlation between the spatial distribution of seeps and DOM compositions in terms of lability, molecular diversity and percentage of nitrogen-containing molecular formulas. Further evidence on MOB-driven DOM modifications is obtained by incubation experiment with the samples obtained from the seep and non-seep sites. The number of molecular formulas increased up to 39 % in methane amended seep and non-seep samples parallel to MOx activity, indicating the possible role of MOB in both production and consumption of DOM. The role of other microbes and microbial modifications, along with the DOM alterations, is remained unresolved in this thesis. More studies are needed to investigate which mi-

crobes contribute to DOM modifications in methane-rich environments and how the microbial consortia respond to methane increase. Integration of FT-ICR MS analysis with the sequencing techniques of the microbial community can provide an answer to this. Metagenomics would estimate microbial responses to changing environmental conditions and a link between DOM and bacterial structure.

Incubation experiments with methanotroph isolates would provide detailed information that can directly be linked to MOx and MOB cellular processes. In this case, analysis methods targeting labile and semi-labile components of DOM would be necessary. Then, the extraction efficiency on labile and semi-labile DOM might be amplified by applying tandem cartridges (Wang et al., 2019) or sorption material (Sánchez-González et al., 2012). Lipidomics and proteomics investigation in medium water and cell tissues may provide a direct comparison of the cell functioning and organic matter production/ consumption pathways. Molecular labelling techniques, such as lipid isotope probing, allow for tracing the microbial conversion of DOM to cellular metabolites, smaller organic molecules and carbon dioxide (Wagner et al., 2020). These tracing methods were used previously to show the biosynthesis of cellular membrane lipids in anaerobic methane-oxidizing archaea (ANME) (Kellermann et al., 2012, 2016). Similarly, the assessment of carbon isotopic tracers, δ^{13}C and Δ^{14}C, may provide insights into carbon flows and mechanisms of cellular uptake with methane DOM interactions. Relative contributions of methane-derived DOC to sedimentary and seawater DOM can be obtained using δ^{13}C and Δ^{14}C measurements and isotopic mixing models (Pohlman et al., 2011).

Cold seeps in the Arctic Ocean carry extensive glaciation-deglaciation history from the Last Glacial Maximum (23,000 years before the present). Retreating marine-based ice sheets formed giant craters, mounds, pockmarks and fractures leading hydrocarbon sources upward to the hydrosphere (Andreassen et al., 2017; Mienert et al., 2005). Geological settings and communities dependent on seeps are primarily different from other cold seeps elsewhere in the world (Åström et al., 2018; Cordes et al., 2007). Similarly, investigations on hydrothermal vents in the Arctic Ocean are relatively recent comparing the other oceans and mid-ocean ridge systems. The Iceland hotspot and its off-axis trace constitute a topographic barrier for hydrography and gene flow from the hydrothermal fauna at the Atlantic ridge system (Ramirez-Llodra et al., 2007). There-

fore, more studies are needed to investigate the biogeochemical connectivity of Arctic seep environments and hydrothermal vents with other sites around the globe.

Bibliography

Alexandropoulou, N., Winsborrow, M., Andreassen, K., Plaza-Faverola, A., Dessandier, P.-A., Mattingsdal, R., Baeten, N., and Knies, J. (2021). A Continuous Seismostratigraphic Framework for the Western Svalbard-Barents Sea Margin Over the Last 2.7 Ma: Implications for the Late Cenozoic Glacial History of the Svalbard-Barents Sea Ice Sheet. *Frontiers in Earth Science*, 9:327.

AMAP (2013). *Arctic climate issues 2011: changes in Arctic snow, water, ice and permafrost*. OCLC: 865475784.

Anderson, L. G. and Amon, R. M. W. (2015). Chapter 14 - DOM in the Arctic Ocean. In Hansell, D. A. and Carlson, C. A., editors, *Biogeochemistry of Marine Dissolved Organic Matter (Second Edition)*, pages 609–633. Academic Press, Boston.

Andreassen, K., Hubbard, A., Winsborrow, M., Patton, H., Vadakkepuliyambatta, S., Plaza-Faverola, A., Gudlaugsson, E., Serov, P., Deryabin, A., Mattingsdal, R., Mienert, J., and Bünz, S. (2017). Massive blow-out craters formed by hydrate-controlled methane expulsion from the Arctic seafloor. *Science*, 356(6341):948–953.

Armstrong, F. a. J., Williams, P. M., and Strickland, J. D. H. (1966). Photo-oxidation of Organic Matter in Sea Water by Ultra-violet Radiation, Analytical and Other Applications. *Nature*, 211(5048):481–483. Bandiera_abtest: a Cg_type: Nature Research Journals Number: 5048 Primary_atype: Research Publisher: Nature Publishing Group.

Armstrong, R. A., Lee, C., Hedges, J. I., Honjo, S., and Wakeham, S. G. (2001). A new, mechanistic model for organic carbon fluxes in the ocean based on the quantitative association of POC with ballast minerals. *Deep Sea Research Part II: Topical Studies in Oceanography*, 49(1):219–236.

Arrieta, J. M., Mayol, E., Hansman, R. L., Herndl, G. J., Dittmar, T., and Duarte, C. M. (2015). Dilution limits dissolved organic carbon utilization in the deep ocean. *Science*, 348(6232):331–333. Publisher: American Association for the Advancement of Science.

Baltar, F., Alvarez-Salgado, X. A., Arístegui, J., Benner, R., Hansell, D. A., Herndl, G. J., and Lønborg, C. (2021). What Is Refractory Organic Matter in the Ocean? *Frontiers in Marine Science*, 8.

Bange, H. W., Bartell, U. H., Rapsomanikis, S., and Andreae, M. O. (1994). Methane in the Baltic and North Seas and a reassessment of the marine emissions of methane. *Global Biogeochemical Cycles*, 8(4):465–480.

Barrow, M. P., Burkitt, W. I., and Derrick, P. J. (2005). Principles of Fourier transform ion cyclotron resonance mass spectrometry and its application in structural biology. *Analyst*, 130(1):18–28. Publisher: Royal Society of Chemistry.

Bastviken, D., Ejlertsson, J., Sundh, I., and Tranvik, L. (2003). Methane as a Source of Carbon and Energy for Lake Pelagic Food Webs. *Ecology*, 84(4):969–981.

Bauer, J. E., Williams, P. M., and Druffel, E. R. M. (1992). C14 activity of dissolved organic carbon fractions in the north · central Pacific and Sargasso Sea. *Nature*, 357.

Beaupré, S. R. (2015). Chapter 6 - The Carbon Isotopic Composition of Marine DOC. In Hansell, D. A. and Carlson, C. A., editors, *Biogeochemistry of Marine Dissolved Organic Matter (Second Edition)*, pages 335–368. Academic Press, Boston.

Beaupré, S. R., Druffel, E. R. M., and Griffin, S. (2007). A low-blank photochemical extraction system for concentration and isotopic analyses of marine dissolved organic carbon. *Limnology and Oceanography: Methods*, 5(6):174–184. _eprint: https://onlinelibrary.wiley.com/doi/pdf/10.4319/lom.2007.5.174.

Berndt, C., Feseker, T., Treude, T., Krastel, S., Liebetrau, V., Niemann, H., Bertics, V. J., Dumke, I., Dünnbier, K., Ferré, B., Graves, C., Gross, F., Hissmann, K., Hühnerbach, V., Krause, S., Lieser, K., Schauer, J., and Steinle, L. (2014). Temporal Constraints on Hydrate-Controlled Methane Seepage off Svalbard. *Science*, 343(6168):284–287.

Boetius, A. (2015). The Expedition PS86 of the Research Vessel POLARSTERN to the Arctic Ocean in 2014. Technical report, Alfred-Wegener-Institut Helmholtz-Zentrum für Polar- und Meeresforschung.

Brankovits, D., Pohlman, J. W., Niemann, H., Leigh, M. B., Leewis, M. C., Becker, K. W., Iliffe, T. M., Alvarez, F., Lehmann, M. F., and Phillips, B. (2017). Methane- and dissolved organic carbon-fueled microbial loop supports a tropical subterranean estuary ecosystem. *Nature Communications*, 8(1):1835.

Brockman, S. A., Roden, E. V., and Hegeman, A. D. (2018). Van Krevelen diagram visualization of high resolution-mass spectrometry metabolomics data with Open-VanKrevelen. *Metabolomics*, 14(4):48.

Brophy, J. E. and Carlson, D. J. (1989). Production of biologically refractory dissolved organic carbon by natural seawater microbial populations. *Deep Sea Research Part A. Oceanographic Research Papers*, 36(4):497–507.

Burdige, D. J., Berelson, W. M., Coale, K. H., McManus, J., and Johnson, K. S. (1999). Fluxes of dissolved organic carbon from California continental margin sediments. *Geochimica et Cosmochimica Acta*, 63(10):1507–1515.

Bünz, S., Polyanov, S., Vadakkepuliyambatta, S., Consolaro, C., and Mienert, J. (2012). Active gas venting through hydrate-bearing sediments on the Vestnesa Ridge, offshore W-Svalbard. *Marine Geology*, 332-334:189–197.

Bünz, S., Ramirez-Llodra, E., German, C., Ferre, B., Sert, F., Kalenickenko, D., Reeves, E., Hand, K., Dahle, H., Kutti, T., Purser, A., Hilario, A., Ramalho, S., Rapp, H. T., Ribeiro, P., Victorero, L., Hoge, U., Panieri, G., Bowen, A., Jakuba, M., Suman, S., Gomez-Ibanez, D., Judge, C., Curran, M., Nalicki, V., Vagenes, S., Lamar, L., Klesh, A., Dessandier, P. A., Steen, I., Mall, A., Vulcano, F., Meckel, E. M., and Drake, N. (2020). RV Kronprins Håkon (cruise no. 2019708) Longyearbyen – Longyearbyen 19.09. – 16.10.2019. Miscellaneous. Num Pages: 100 Publisher: UIT - The Arctic University of Norway.

Carlson, C. A. and Hansell, D. A. (2015). Chapter 3 - DOM Sources, Sinks, Reactivity, and Budgets. In *Biogeochemistry of Marine Dissolved Organic Matter (Second Edition)*, pages 65–126. Academic Press, Boston.

Cech, N. B. and Enke, C. G. (2001). Practical implications of some recent studies in electrospray ionization fundamentals. *Mass Spectrometry Reviews*, 20(6):362–387. _eprint: https://onlinelibrary.wiley.com/doi/pdf/10.1002/mas.10008.

Charlou, J. L. and Donval, J.-P. (1993). Hydrothermal methane venting between 12°N and 26°N along the Mid-Atlantic Ridge. *Journal of Geophysical Research: Solid Earth*, 98(B6):9625–9642. _eprint: https://agupubs.onlinelibrary.wiley.com/doi/pdf/10.1029/92JB02047.

Cho, Y., Ahmed, A., Islam, A., and Kim, S. (2015). Developments in FT-ICR MS instrumentation, ionization techniques, and data interpretation methods for petroleomics. *Mass Spectrometry Reviews*, 34(2):248–263. _eprint: https://onlinelibrary.wiley.com/doi/pdf/10.1002/mas.21438.

Coble, P. G. (2007). Marine optical biogeochemistry: the chemistry of ocean color. *Chemical Reviews-Columbus*, 107(2):402–418.

Conrad, R. and Seiler, W. (1988). Methane and hydrogen in seawater (Atlantic Ocean). *Deep Sea Research Part A. Oceanographic Research Papers*, 35(12):1903–1917.

Cordes, E. E., Carney, S. L., Hourdez, S., Carney, R. S., Brooks, J. M., and Fisher, C. R. (2007). Cold seeps of the deep Gulf of Mexico: Community structure and biogeographic comparisons to Atlantic equatorial belt seep communities. *Deep Sea Research Part I: Oceanographic Research Papers*, 54(4):637–653.

Corilo, Y. (2014). PetroOrg Software.

D'Andrilli, J. (2009). *Molecular characterization of marine and terrestrial dissolved organic matter using ultrahigh resolution mass spectrometry.* Ph.D., Ann Arbor, United States.

D'Andrilli, J., Cooper, W. T., Foreman, C. M., and Marshall, A. G. (2015). An ultrahigh-resolution mass spectrometry index to estimate natural organic matter lability: FTICRMS organic matter molecular lability index. *Rapid Communications in Mass Spectrometry*, 29(24):2385–2401.

D'Andrilli, J., Dittmar, T., Koch, B. P., Purcell, J. M., Marshall, A. G., and Cooper, W. T. (2010). Comprehensive characterization of marine dissolved organic matter by

Fourier transform ion cyclotron resonance mass spectrometry with electrospray and atmospheric pressure photoionization. *Rapid Communications in Mass Spectrometry*, 24(5):643–650.

Dedysh, S. N., Knief, C., and Dunfield, P. F. (2005). Methylocella species are facultatively methanotrophic. *Journal of Bacteriology*, 187(13):4665–4670.

Dittmar, T. (2015). Chapter 7 - Reasons Behind the Long-Term Stability of Dissolved Organic Matter. In Hansell, D. A. and Carlson, C. A., editors, *Biogeochemistry of Marine Dissolved Organic Matter (Second Edition)*, pages 369–388. Academic Press, Boston.

Dittmar, T., Koch, B., Hertkorn, N., and Kattner, G. (2008). A simple and efficient method for the solid-phase extraction of dissolved organic matter (SPE-DOM) from seawater. *Limnology and Oceanography: Methods*, 6(6):230–235.

Dittmar, T. and Koch, B. P. (2006). Thermogenic organic matter dissolved in the abyssal ocean. *Marine Chemistry*, 102(3-4):208–217.

Dittmar, T. and Paeng, J. (2009). A heat-induced molecular signature in marine dissolved organic matter. *Nature Geoscience*, 2(3):175–179. Number: 3 Publisher: Nature Publishing Group.

Dittmar, T. and Stubbins, A. (2014). Dissolved Organic Matter in Aquatic Systems. In Holland, H. D. and Turekian, K. K., editors, *Treatise on Geochemistry*, pages 125–156. Elseiver:Oxford, 2 edition.

D'Andrilli, J., Fischer, S. J., and Rosario-Ortiz, F. L. (2020). Advancing Critical Applications of High Resolution Mass Spectrometry for DOM Assessments: Re-Engaging with Mass Spectral Principles, Limitations, and Data Analysis. *Environmental Science & Technology*. Publisher: American Chemical Society.

D'souza, N. A., Subramaniam, A., Juhl, A. R., Hafez, M., Chekalyuk, A., Phan, S., Yan, B., MacDonald, I. R., Weber, S. C., and Montoya, J. P. (2016). Elevated surface chlorophyll associated with natural oil seeps in the Gulf of Mexico. *Nature Geoscience*, 9(3):215–218.

Edmonds, H. N., Michael, P. J., Baker, E. T., Connelly, D. P., Snow, J. E., Langmuir, C. H., Dick, H. J. B., Mühe, R., German, C. R., and Graham, D. W. (2003). Discovery of abundant hydrothermal venting on the ultraslow-spreading Gakkel ridge in the Arctic Ocean. *Nature*, 421(6920):252–256.

Elvert, M. and Niemann, H. (2008). Occurrence of unusual steroids and hopanoids derived from aerobic methanotrophs at an active marine mud volcano. *Organic Geochemistry*, 39(2):167–177.

Etminan, M., Myhre, G., Highwood, E. J., and Shine, K. P. (2016). Radiative forcing of carbon dioxide, methane, and nitrous oxide: A significant revision of the methane radiative forcing. *Geophysical Research Letters*, 43(24):12,614–12,623. _eprint: https://onlinelibrary.wiley.com/doi/pdf/10.1002/2016GL071930.

Fenn, J. B., Mann, M., Meng, C. K., Wong, S. F., and Whitehouse, C. M. (1989). Electrospray ionization for mass spectrometry of large biomolecules. *Science*, 246(4926):64–71.

Fer, I., Müller, M., and Peterson, A. K. (2015). Tidal forcing, energetics, and mixing near the Yermak Plateau. *Ocean Science*, 11(2):287–304.

Ferré, B., Jansson, P. G., Moser, M., Serov, P., Portnov, A., Graves, C. A., Panieri, G., Gründger, F., Berndt, C., Lehmann, M. F., and Niemann, H. (2020a). Reduced methane seepage from Arctic sediments during cold bottom-water conditions. *Nature Geoscience*, 13(2):144–148.

Ferré, B., Moser, M., Dølven, K. O., Sert, F., Stetzler, M., Savini, A., Jones, E., de Groot, T., Friedrich, J., Jensen, S., Meyer, J. P., Micheel, M., and Erntsen, E. (2020b). CAGE 20-7 Cruise report: Sediment and water column analyses around flares at Norskebanken, Hinlopen and offshore Prins Karls Forland. Technical report.

Findlay, H. S., Gibson, G., Kedra, M., Morata, N., Orchowska, M., Pavlov, A. K., Reigstad, M., Silyakova, A., Tremblay, J.-, Walczowski, W., Weydmann, A., and Logvinova, C. (2015). Responses in Arctic marine carbon cycle processes: conceptual scenarios and implications for ecosystem function. *Polar Research*, 34(1):24252.

Geissler, W. H., Gebhardt, A. C., Gross, F., Wollenburg, J., Jensen, L., Schmidt-Aursch, M. C., Krastel, S., Elger, J., and Osti, G. (2016). Arctic megaslide at presumed rest. *Scientific Reports*, 6(1):38529. Bandiera_abtest: a Cc_license_type: cc_by Cg_type: Nature Research Journals Number: 1 Primary_atype: Research Publisher: Nature Publishing Group Subject_term: Natural hazards;Solid Earth sciences Subject_term_id: natural-hazards;solid-earth-sciences.

German, C. and Seyfried, W. (2014). Hydrothermal Processes. In *Treatise on Geochemistry*, pages 191–233. Elsevier.

Gonsior, M., Peake, B. M., Cooper, W. T., Podgorski, D. C., D'Andrilli, J., Dittmar, T., and Cooper, W. J. (2011). Characterization of dissolved organic matter across the Subtropical Convergence off the South Island, New Zealand. *Marine Chemistry*, 123(1):99–110.

Graves, C. A., Steinle, L., Rehder, G., Niemann, H., Connelly, D. P., Lowry, D., Fisher, R. E., Stott, A. W., Sahling, H., and James, R. H. (2015). Fluxes and fate of dissolved methane released at the seafloor at the landward limit of the gas hydrate stability zone offshore western Svalbard: Dissolved methane off western Svalbard. *Journal of Geophysical Research: Oceans*, 120(9):6185–6201.

Gründger, F., Carrier, V., Svenning, M. M., Panieri, G., Vonnahme, T. R., Klasek, S., and Niemann, H. (2019). Methane-fuelled biofilms predominantly composed of methanotrophic ANME-1 in Arctic gas hydrate-related sediments. *Scientific Reports*, 9(1):9725.

Gründger, F., Probandt, D., Knittel, K., Carrier, V., Kalenitchenko, D., Silyakova, A., Serov, P., Ferré, B., Svenning, M. M., and Niemann, H. (2021). Seasonal shifts of microbial methane oxidation in Arctic shelf waters above gas seeps. *Limnology and Oceanography*, n/a(n/a).

Han, L., Kaesler, J., Peng, C., Reemtsma, T., and Lechtenfeld, O. J. (2021). Online Counter Gradient LC-FT-ICR-MS Enables Detection of Highly Polar Natural Organic Matter Fractions. *Analytical Chemistry*, 93(3):1740–1748. Publisher: American Chemical Society.

Hansell, D., Carlson, C., Repeta, D., and Schlitzer, R. (2009). Dissolved organic matter in the ocean: a controversy stimulates new insights. *Oceanography*, 22(4):202–211.

Hansell, D. A. (2013). Recalcitrant Dissolved Organic Carbon Fractions. *Annual Review of Marine Science*, 5(1):421–445.

Hansen, J., Sato, M., Lacis, A., Ruedy, R., Tegen, I., and Matthews, E. (1998). Climate forcings in the Industrial era. *Proceedings of the National Academy of Sciences of the United States of America*, 95(22):12753–12758.

Hansen, J., Sato, M., and Ruedy, R. (1997). Radiative forcing and climate response. *J. Geophys. Res.*

Hanson, R. S. and Hanson, T. E. (1996). Methanotrophic bacteria. *Microbiological reviews*, 60(2):439–471.

Hawkes, J. A., D'Andrilli, J., Agar, J. N., Barrow, M. P., Berg, S. M., Catalán, N., Chen, H., Chu, R. K., Cole, R. B., Dittmar, T., Gavard, R., Gleixner, G., Hatcher, P. G., He, C., Hess, N. J., Hutchins, R. H. S., Ijaz, A., Jones, H. E., Kew, W., Khaksari, M., Palacio Lozano, D. C., Lv, J., Mazzoleni, L. R., Noriega-Ortega, B. E., Osterholz, H., Radoman, N., Remucal, C. K., Schmitt, N. D., Schum, S. K., Shi, Q., Simon, C., Singer, G., Sleighter, R. L., Stubbins, A., Thomas, M. J., Tolic, N., Zhang, S., Zito, P., and Podgorski, D. C. (2020). An international laboratory comparison of dissolved organic matter composition by high resolution mass spectrometry: Are we getting the same answer? *Limnology and Oceanography: Methods*, 18(6):235–258. _eprint: https://onlinelibrary.wiley.com/doi/pdf/10.1002/lom3.10364.

Hawkes, J. A., Patriarca, C., Sjöberg, P. J. R., Tranvik, L. J., and Bergquist, J. (2018). Extreme isomeric complexity of dissolved organic matter found across aquatic environments. *Limnology and Oceanography Letters*, 3(2):21–30. _eprint: https://aslopubs.onlinelibrary.wiley.com/doi/pdf/10.1002/lol2.10064.

Hawkes, J. A., Rossel, P. E., Stubbins, A., Butterfield, D., Connelly, D. P., Achterberg, E. P., Koschinsky, A., Chavagnac, V., Hansen, C. T., Bach, W., and Dittmar, T. (2015). Efficient removal of recalcitrant deep-ocean dissolved organic matter during hydrothermal circulation. *Nature Geoscience*, 8(11):856–860.

Hedges, J. I. (1992). Global biogeochemical cycles: progress and problems. *Marine Chemistry*, 39(1):67–93.

Helms, J. R., Stubbins, A., Ritchie, J. D., Minor, E. C., Kieber, D. J., and Mopper, K. (2008). Absorption spectral slopes and slope ratios as indicators of molecular weight, source, and photobleaching of chromophoric dissolved organic matter. *Limnology and Oceanography*, 53(3):955–969.

Hendrickson, C. L., Quinn, J. P., Kaiser, N. K., Smith, D. F., Blakney, G. T., Chen, T., Marshall, A. G., Weisbrod, C. R., and Beu, S. C. (2015). 21 Tesla Fourier Transform Ion Cyclotron Resonance Mass Spectrometer: A National Resource for Ultrahigh Resolution Mass Analysis. *Journal of The American Society for Mass Spectrometry*, 26(9):1626–1632.

Hertkorn, N., Harir, M., Koch, B. P., Michalke, B., and Schmitt-Kopplin, P. (2013). High-field NMR spectroscopy and FTICR mass spectrometry: powerful discovery tools for the molecular level characterization of marine dissolved organic matter. *Biogeosciences*, 10(3):1583–1624.

Hinrichs, K.-U. and Boetius, A. (2003). The Anaerobic Oxidation of Methane: New Insights in Microbial Ecology and Biogeochemistry. In Wefer, G., Billett, D., Hebbeln, D., Jørgensen, B. B., Schlüter, M., and van Weering, T. C. E., editors, *Ocean Margin Systems*, pages 457–477. Springer, Berlin, Heidelberg.

Hioki, N., Kuma, K., Morita, Y., Sasayama, R., Ooki, A., Kondo, Y., Obata, H., Nishioka, J., Yamashita, Y., Nishino, S., Kikuchi, T., and Aoyama, M. (2014). Laterally spreading iron, humic-like dissolved organic matter and nutrients in cold, dense subsurface water of the Arctic Ocean. *Scientific Reports*, 4:6775.

Hockaday, W. C., Purcell, J. M., Marshall, A. G., Baldock, J. A., and Hatcher, P. G. (2009). Electrospray and photoionization mass spectrometry for the characterization of organic matter in natural waters: a qualitative assessment. *Limnology and Oceanography: Methods*, 7(1):81–95.

Hodgkins, S. B., Tfaily, M. M., Podgorski, D. C., McCalley, C. K., Saleska, S. R., Crill, P. M., Rich, V. I., Chanton, J. P., and Cooper, W. T. (2016). Elemental composition

and optical properties reveal changes in dissolved organic matter along a permafrost thaw chronosequence in a subarctic peatland. *Geochimica et Cosmochimica Acta*, 187:123–140.

Hoglund-Isaksson, L. (2012). Global anthropogenic methane emissions 2005–2030: technical mitigation potentials and costs. *Atmos. Chem. Phys.*, page 18.

Jaccard, P. (1912). The distribution of the flora in the alpine zone. *New Phytologist*, 11(2):37–50.

Jain, A. K., Briegleb, B. P., Minschwaner, K., and Wuebbles, D. J. (2000). Radiative forcings and global warming potentials of 39 greenhouse gases. *Journal of Geophysical Research: Atmospheres*, 105(D16):20773–20790. _eprint: https://onlinelibrary.wiley.com/doi/pdf/10.1029/2000JD900241.

Jansson, P. (2018). *Methane bubbles in the Arctic Ocean: Quantification, variability analysis and modelling of free and dissolved methane from the seafloor to the atmosphere.* PhD thesis.

Jiao, N., Herndl, G. J., Hansell, D. A., Benner, R., Kattner, G., Wilhelm, S. W., Kirchman, D. L., Weinbauer, M. G., Luo, T., Chen, F., and Azam, F. (2010). Microbial production of recalcitrant dissolved organic matter: long-term carbon storage in the global ocean. *Nature Reviews Microbiology*, 8:593–599.

Johnson, W. M., Soule, M. C. K., and Kujawinski, E. B. (2017). Extraction efficiency and quantification of dissolved metabolites in targeted marine metabolomics. *Limnology and Oceanography: Methods*, 15(4):417–428.

Judd, A. G., Hovland, M., Dimitrov, L. I., García Gil, S., and Jukes, V. (2002). The geological methane budget at Continental Margins and its influence on climate change. *Geofluids*, 2(2):109–126. _eprint: https://onlinelibrary.wiley.com/doi/pdf/10.1046/j.1468-8123.2002.00027.x.

Kalyuzhnaya, M. G., Yang, S., Rozova, O. N., Smalley, N. E., Clubb, J., Lamb, A., Gowda, G. A. N., Raftery, D., Fu, Y., Bringel, F., Vuilleumier, S., Beck, D. a. C., Trotsenko, Y. A., Khmelenina, V. N., and Lidstrom, M. E. (2013). Highly efficient

methane biocatalysis revealed in a methanotrophic bacterium. *Nature Communications*, 4:2785.

Karl, D., Beversdorf, L., Orkman, K., Church, M., Martinez, A., and Delong, E. (2008). Aerobic production of methane in the sea. *Nature Geoscience*, 1.

Kellerman, A. M., Kothawala, D. N., Dittmar, T., and Tranvik, L. J. (2015). Persistence of dissolved organic matter in lakes related to its molecular characteristics. *Nature Geoscience*, 8(6):454–457.

Kellermann, M. Y., Wegener, G., Elvert, M., Yoshinaga, M. Y., Lin, Y.-S., Holler, T., Mollar, X. P., Knittel, K., and Hinrichs, K.-U. (2012). Autotrophy as a predominant mode of carbon fixation in anaerobic methane-oxidizing microbial communities. *Proceedings of the National Academy of Sciences*, 109(47):19321–19326. Publisher: Proceedings of the National Academy of Sciences.

Kellermann, M. Y., Yoshinaga, M. Y., Wegener, G., Krukenberg, V., and Hinrichs, K.-U. (2016). Tracing the production and fate of individual archaeal intact polar lipids using stable isotope probing. *Organic Geochemistry*, 95:13–20.

Kim, S., Kramer, R. W., and Hatcher, P. G. (2003). Graphical Method for Analysis of Ultrahigh-Resolution Broadband Mass Spectra of Natural Organic Matter, the Van Krevelen Diagram. *Analytical Chemistry*, 75(20):5336–5344.

Knittel, K. and Boetius, A. (2009). Anaerobic Oxidation of Methane: Progress with an Unknown Process. *Annual Review of Microbiology*, 63(1):311–334.

Koch, B. P. and Dittmar, T. (2006). From mass to structure: an aromaticity index for high-resolution mass data of natural organic matter. *Rapid Communications in Mass Spectrometry*, 20(5):926–932.

Koch, B. P., Witt, M., Engbrodt, R., Dittmar, T., and Kattner, G. (2005). Molecular formulae of marine and terrigenous dissolved organic matter detected by electrospray ionization Fourier transform ion cyclotron resonance mass spectrometry. *Geochimica et Cosmochimica Acta*, 69(13):3299–3308.

Koivusalo, M., Haimi, P., Heikinheimo, L., Kostiainen, R., and Somerharju, P. (2001). Quantitative determination of phospholipid compositions by ESI-MS: effects of acyl

chain length, unsaturation, and lipid concentration on instrument response. *Journal of Lipid Research*, 42(4):663–672.

Konn, C., Charlou, J. L., Holm, N. G., and Mousis, O. (2015). The Production of Methane, Hydrogen, and Organic Compounds in Ultramafic-Hosted Hydrothermal Vents of the Mid-Atlantic Ridge. *Astrobiology*, 15:19.

Kujawinski, E. B. (2011). The Impact of Microbial Metabolism on Marine Dissolved Organic Matter. *Annual Review of Marine Science*, 3(1):567–599.

Kujawinski, E. B., Longnecker, K., Barott, K. L., Weber, R. J. M., and Kido Soule, M. C. (2016). Microbial Community Structure Affects Marine Dissolved Organic Matter Composition. *Frontiers in Marine Science*, 3.

Lechtenfeld, O. J., Hertkorn, N., Shen, Y., Witt, M., and Benner, R. (2015). Marine sequestration of carbon in bacterial metabolites. *Nature Communications*, 6(1):1–8.

Lee, K., Choi, O. K., Kim, Y., Park, J., and Lee, J. W. (2019). Methane utilization in aerobic methane oxidation coupled to denitrification (AME-D): theoretical estimation and effect of hydraulic retention time (HRT). *Biodegradation*, 30(2):101–112.

Letscher, R. T., Hansell, D. A., and Kadko, D. (2011). Rapid removal of terrigenous dissolved organic carbon over the Eurasian shelves of the Arctic Ocean. *Marine Chemistry*, 123(1-4):78–87.

Levin, L. A. (2005). Ecology of Cold Seep Sediments: Interactions of Fauna with Flow, Chemistry and Microbes. *Oceanography and Marine Biology*.

Levin, L. A., Baco, A. R., Bowden, D. A., Colaco, A., Cordes, E. E., Cunha, M. R., Demopoulos, A. W. J., Gobin, J., Grupe, B. M., Le, J., Metaxas, A., Netburn, A. N., Rouse, G. W., Thurber, A. R., Tunnicliffe, V., Van Dover, C. L., Vanreusel, A., and Watling, L. (2016). Hydrothermal Vents and Methane Seeps: Rethinking the Sphere of Influence. *Frontiers in Marine Science*, 3. Publisher: Frontiers.

Longnecker, K. (2015). Dissolved organic matter in newly formed sea ice and surface seawater. *Geochimica et Cosmochimica Acta*, 171:39–49.

Lupton, J. E. and Craig, H. (1981). A Major Helium-3 Source at 15°S on the East Pacific Rise. *Science*, 214(4516):13–18. Publisher: American Association for the Advancement of Science.

Marshall, A. G., Hendrickson, C. L., and Jackson, G. S. (1998). Fourier transform ion cyclotron resonance mass spectrometry: A primer. *Mass Spectrometry Reviews*, 17(1):1–35.

McCollom, T. M., Ritter, G., and Simoneit, B. R. T. (1999). Lipid Synthesis Under Hydrothermal Conditions by Fischer- Tropsch-Type Reactions. *Origins of Life and Evolution of the Biosphere*, 29:153–166.

McGinnis, D. F., Greinert, J., Artemov, Y., Beaubien, S. E., and Wüest, A. (2006). Fate of rising methane bubbles in stratified waters: How much methane reaches the atmosphere? *Journal of Geophysical Research: Oceans*, 111(C9).

Meier, W. N., Hovelsrud, G. K., van Oort, B. E., Key, J. R., Kovacs, K. M., Michel, C., Haas, C., Granskog, M. A., Gerland, S., Perovich, D. K., Makshtas, A., and Reist, J. D. (2014). Arctic sea ice in transformation: A review of recent observed changes and impacts on biology and human activity. *Reviews of Geophysics*, 52(3):2013RG000431.

Menzel, D. W. (1964). The distribution of dissolved organic carbon in the Western Indian Ocean. *Deep Sea Research and Oceanographic Abstracts*, 11(5):757–765.

Merder, J., Freund, J. A., Feudel, U., Hansen, C. T., Hawkes, J. A., Jacob, B., Klaproth, K., Niggemann, J., Noriega-Ortega, B. E., Osterholz, H., Rossel, P. E., Seidel, M., Singer, G., Stubbins, A., Waska, H., and Dittmar, T. (2020). ICBM-OCEAN: Processing Ultrahigh-Resolution Mass Spectrometry Data of Complex Molecular Mixtures. *Analytical Chemistry*, 92(10):6832–6838. Publisher: American Chemical Society.

Metcalf, W. W., Griffin, B. M., Cicchillo, R. M., Gao, J., Janga, S. C., Cooke, H. A., Circello, B. T., Evans, B. S., Martens-Habbena, W., Stahl, D. A., and van der Donk, W. A. (2012). Synthesis of Methylphosphonic Acid by Marine Microbes: A Source for Methane in the Aerobic Ocean. *Science*, 337(6098):1104–1107. Publisher: American Association for the Advancement of Science.

Michael, P. J., Langmuir, C. H., Dick, H. J. B., Snow, J. E., Goldstein, S. L., Graham, D. W., Lehnert, K., Kurras, G., Jokat, W., Mühe, R., and Edmonds, H. N. (2003). Magmatic and amagmatic seafloor generation at the ultraslow-spreading Gakkel ridge, Arctic Ocean. *Nature*, 423(6943):956–961.

Middelburg, J. J. (1989). A simple rate model for organic matter decomposition in marine sediments. *Geochimica et Cosmochimica Acta*, 53(7):1577–1581.

Middelburg, J. J. (2011). Chemoautotrophy in the ocean: CHEMOAUTOTROPHY IN THE OCEAN. *Geophysical Research Letters*, 38(24):n/a–n/a.

Mienert, J., Vanneste, M., Bünz, S., Andreassen, K., Haflidason, H., and Sejrup, H. P. (2005). Ocean warming and gas hydrate stability on the mid-Norwegian margin at the Storegga Slide. *Marine and Petroleum Geology*, 22(1):233–244.

Mopper, K., Stubbins, A., Ritchie, J. D., Bialk, H. M., and Hatcher, P. G. (2007). Advanced Instrumental Approaches for Characterization of Marine Dissolved Organic Matter: Extraction Techniques, Mass Spectrometry, and Nuclear Magnetic Resonance Spectroscopy. *Chemical Reviews*, 107(2):419–442.

Moran, M. A., Kujawinski, E. B., Stubbins, A., Fatland, R., Aluwihare, L. I., Buchan, A., Crump, B. C., Dorrestein, P. C., Dyhrman, S. T., Hess, N. J., Howe, B., Longnecker, K., Medeiros, P. M., Niggemann, J., Obernosterer, I., Repeta, D. J., and Waldbauer, J. R. (2016). Deciphering ocean carbon in a changing world. *Proceedings of the National Academy of Sciences*, 113(12):3143–3151.

Muller-Karger, F. E., Varela, R., Thunell, R., Luerssen, R., Hu, C., and Walsh, J. J. (2005). The importance of continental margins in the global carbon cycle. *Geophysical Research Letters*, 32(1). _eprint: https://onlinelibrary.wiley.com/doi/pdf/10.1029/2004GL021346.

Myhre, C. L., Ferré, B., Platt, S. M., Silyakova, A., Hermansen, O., Allen, G., Pisso, I., Schmidbauer, N., Stohl, A., Pitt, J., Jansson, P., Greinert, J., Percival, C., Fjaeraa, A. M., O'Shea, S. J., Gallagher, M., Le Breton, M., Bower, K. N., Bauguitte, S. J. B., Dalsøren, S., Vadakkepuliyambatta, S., Fisher, R. E., Nisbet, E. G., Lowry, D., Myhre, G., Pyle, J. A., Cain, M., and Mienert, J. (2016). Extensive release of

methane from Arctic seabed west of Svalbard during summer 2014 does not influence the atmosphere. *Geophysical Research Letters*, 43(9):2016GL068999.

Niemann, H., Steinle, L., Blees, J., Bussmann, I., Treude, T., Krause, S., Elvert, M., and Lehmann, M. F. (2015). Toxic effects of lab-grade butyl rubber stoppers on aerobic methane oxidation. *Limnology and Oceanography: Methods*, 13(1):40–52.

Ogawa, H., Amagai, Y., Koike, I., Kaiser, K., and Benner, R. (2001). Production of Refractory Dissolved Organic Matter by Bacteria. *Science*, 292(5518):917–920.

Ogawa, H. and Tanoue, E. (2003). Dissolved Organic Matter in Oceanic Waters. *Journal of Oceanography*, 59(2):129–147.

Olsen, M. S., Callaghan, T. V., Reist, J. D., Reiersen, L. O., Dahl-Jensen, D., Granskog, M. A., Goodison, B., Hovelsrud, G. K., Johansson, M., Kallenborn, R., Key, J., Klepikov, A., Meier, W., Overland, J. E., Prowse, T. D., Sharp, M., Vincent, W. F., and Walsh, J. (2011). The Changing Arctic Cryosphere and Likely Consequences: An Overview. *AMBIO: A Journal of the Human Environment*, 40(sp1):111–118.

Ortmann, A. and Suttle, C. (2005). High abundance of viruses in a deep-sea hydrothermal vent system indicates viral mediated microbial mortality. *Deep Sea Research Part I: Oceanographic Research Papers*, 52:1515–1527.

Oss, M., Kruve, A., Herodes, K., and Leito, I. (2010). Electrospray Ionization Efficiency Scale of Organic Compounds. *Analytical Chemistry*, 82(7):2865–2872. Publisher: American Chemical Society.

Osterholz, H. (2014). *From freshly produced compounds to refractory molecules-tracing sources and fate of dissolved organic matter in the ocean.* PhD thesis.

Osterholz, H., Dittmar, T., and Niggemann, J. (2014). Molecular evidence for rapid dissolved organic matter turnover in Arctic fjords. *Marine Chemistry*, 160:1–10.

Osterholz, H., Niggemann, J., Giebel, H.-A., Simon, M., and Dittmar, T. (2015). Inefficient microbial production of refractory dissolved organic matter in the ocean. *Nature Communications*, 6:7422.

Paliy, O. and Shankar, V. (2016). Application of multivariate statistical techniques in microbial ecology. *Molecular Ecology*, 25(5):1032–1057.

Panieri, G., Bünz, S., Fornari, D. J., Escartin, J., Serov, P., Jansson, P., Torres, M. E., Johnson, J. E., Hong, W., Sauer, S., Garcia, R., and Gracias, N. (2017). An integrated view of the methane system in the pockmarks at Vestnesa Ridge, 79°N. *Marine Geology*, 390:282–300.

Petersen, J. M., Zielinski, F. U., Pape, T., Seifert, R., Moraru, C., Amann, R., Hourdez, S., Girguis, P. R., Wankel, S. D., Barbe, V., Pelletier, E., Fink, D., Borowski, C., Bach, W., and Dubilier, N. (2011). Hydrogen is an energy source for hydrothermal vent symbioses. *Nature*, 476(7359):176–180.

Petras, D., Minich, J. J., Cancelada, L. B., Torres, R. R., Kunselman, E., Wang, M., White, M. E., Allen, E. E., Prather, K. A., Aluwihare, L. I., and Dorrestein, P. C. (2021). Non-targeted tandem mass spectrometry enables the visualization of organic matter chemotype shifts in coastal seawater. *Chemosphere*, 271:129450.

Pohlman, J., Bauer, J., Canuel, E., Grabowski, K., Knies, D., Mitchell, C., Whiticar, M., and Coffin, R. (2009). Methane sources in gas hydrate-bearing cold seeps: Evidence from radiocarbon and stable isotopes. *Marine Chemistry*, 115(1-2):102–109.

Pohlman, J. W., Bauer, J. E., Waite, W. F., Osburn, C. L., and Chapman, N. R. (2011). Methane hydrate-bearing seeps as a source of aged dissolved organic carbon to the oceans. *Nature Geoscience*, 4(1):37–41.

Pohlman, J. W., Greinert, J., Ruppel, C., Silyakova, A., Vielstädte, L., Casso, M., Mienert, J., and Bünz, S. (2017). Enhanced CO2 uptake at a shallow Arctic Ocean seep field overwhelms the positive warming potential of emitted methane. *Proceedings of the National Academy of Sciences*, 114(21):5355–5360.

Qian, J. and Mopper, K. (1996). Automated High-Performance, High-Temperature Combustion Total Organic Carbon Analyzer. *Analytical Chemistry*, 68(18):3090–3097.

Ramirez-Llodra, E., Shank, T., and German, C. (2007). Biodiversity and Biogeography of Hydrothermal Vent Species: Thirty Years of Discovery and Investigations. *Oceanography*, 20(1):30–41.

Reeburgh, W. S. (2007). Oceanic Methane Biogeochemistry. *Chemical Reviews*, 107(2):486–513.

Repeta, D. J. (2015). Chapter 2 - Chemical Characterization and Cycling of Dissolved Organic Matter. In Hansell, D. A. and Carlson, C. A., editors, *Biogeochemistry of Marine Dissolved Organic Matter (Second Edition)*, pages 21–63. Academic Press, Boston.

Repeta, D. J., Ferrón, S., Sosa, O. A., Johnson, C. G., Repeta, L. D., Acker, M., DeLong, E. F., and Karl, D. M. (2016). Marine methane paradox explained by bacterial degradation of dissolved organic matter. *Nature Geoscience*, 9(12):884–887.

Riedel, T. and Dittmar, T. (2014). A Method Detection Limit for the Analysis of Natural Organic Matter via Fourier Transform Ion Cyclotron Resonance Mass Spectrometry. *Analytical Chemistry*, 86(16):8376–8382. Publisher: American Chemical Society.

Rivas-Ubach, A., Liu, Y., Bianchi, T. S., Tolić, N., Jansson, C., and Paša-Tolić, L. (2018). Moving beyond the van Krevelen Diagram: A New Stoichiometric Approach for Compound Classification in Organisms. *Analytical Chemistry*, 90(10):6152–6160. Publisher: American Chemical Society.

Rossel, P. E., Stubbins, A., Hach, P. F., and Dittmar, T. (2015). Bioavailability and molecular composition of dissolved organic matter from a diffuse hydrothermal system. *Marine Chemistry*, 177:257–266.

Rossel, P. E., Stubbins, A., Rebling, T., Koschinsky, A., Hawkes, J. A., and Dittmar, T. (2017). Thermally altered marine dissolved organic matter in hydrothermal fluids. *Organic Geochemistry*, 110:73–86.

Rudels, B., Meyer, R., Fahrbach, E., Ivanov, V. V., Østerhus, S., Quadfasel, D., Schauer, U., Tverberg, V., and Woodgate, R. A. (2000). Water mass distribution in Fram Strait and over the Yermak Plateau in summer 1997. *Annales Geophysicae*, 18(6):687–705.

Sahling, H., Römer, M., Pape, T., Bergès, B., dos Santos Fereirra, C., Boelmann, J., Geprägs, P., Tomczyk, M., Nowald, N., Dimmler, W., Schroedter, L., Glockzin, M.,

and Bohrmann, G. (2014). Gas emissions at the continental margin west of Svalbard: mapping, sampling, and quantification. *Biogeosciences*, 11(21):6029–6046.

Scigelova, M., Hornshaw, M., Giannakopulos, A., and Makarov, A. (2011). Fourier Transform Mass Spectrometry. *Molecular & Cellular Proteomics*, 10(7):M111.009431.

Scranton, M. I. and Brewer, P. G. (1978). Consumption of dissolved methane in the deep ocean. *Limnology and Oceanography*, 23(6):1207–1213.

Serov, P., Vadakkepuliyambatta, S., Mienert, J., Patton, H., Portnov, A., Silyakova, A., Panieri, G., Carroll, M. L., Carroll, J., Andreassen, K., and Hubbard, A. (2017). Postglacial response of Arctic Ocean gas hydrates to climatic amelioration. *Proceedings of the National Academy of Sciences*, 114(24):6215–6220. Publisher: National Academy of Sciences Section: Physical Sciences.

Sert, M. F., D'Andrilli, J., Gründger, F., Niemann, H., Granskog, M. A., Pavlov, A. K., Ferré, B., and Silyakova, A. (2020). Compositional Differences in Dissolved Organic Matter Between Arctic Cold Seeps Versus Non-Seep Sites at the Svalbard Continental Margin and the Barents Sea. *Frontiers in Earth Science*, 8:552731. Publisher: Frontiers.

Sharp, J. H., Suzuki, Y., and Munday, W. L. (1993). A comparison of dissolved organic carbon in North Atlantic Ocean nearshore waters by high temperature combustion and wet chemical oxidation. *Marine Chemistry*, 41(1):253–259.

Sibson, R. (1972). Order Invariant Methods for Data Analysis. *Journal of the Royal Statistical Society: Series B (Methodological)*, 34(3):311–338. _eprint: https://onlinelibrary.wiley.com/doi/pdf/10.1111/j.2517-6161.1972.tb00910.x.

Silyakova, A., Jansson, P., Serov, P., Ferré, B., Pavlov, A. K., Hattermann, T., Graves, C. A., Platt, S. M., Myhre, C. L., Gründger, F., and Niemann, H. (2020). Physical controls of dynamics of methane venting from a shallow seep area west of Svalbard. *Continental Shelf Research*, 194:104030.

Simoneit, B. R. T., Lein, A. Y., Peresypkin, V. I., and Osipov, G. A. (2004). Composition and origin of hydrothermal petroleum and associated lipids in the sulfide

deposits of the Rainbow field (Mid-Atlantic Ridge at 36°N) 1 1Associate editor: G. A. Logan. *Geochimica et Cosmochimica Acta*, 68(10):2275–2294.

Sipler, R. E. and Bronk, D. A. (2015). Chapter 4 - Dynamics of Dissolved Organic Nitrogen. In Hansell, D. A. and Carlson, C. A., editors, *Biogeochemistry of Marine Dissolved Organic Matter (Second Edition)*, pages 127–232. Academic Press, Boston.

Skoog, D. A., Crouch, S. R., and Holler, F. J. (2007). *Principles of instrumental analysis*. Thomson Brooks/Cole, Belmont, CA. OCLC: 423542548.

Sleighter, R. L., Liu, Z., Xue, J., and Hatcher, P. G. (2010). Multivariate Statistical Approaches for the Characterization of Dissolved Organic Matter Analyzed by Ultrahigh Resolution Mass Spectrometry. *Environmental Science & Technology*, 44(19):7576–7582.

Stedmon, C. A. and Bro, R. (2008). Characterizing dissolved organic matter fluorescence with parallel factor analysis: a tutorial. *Limnology and Oceanography: Methods*, 6(11):572–579.

Stedmon, C. A., Markager, S., and Bro, R. (2003). Tracing dissolved organic matter in aquatic environments using a new approach to fluorescence spectroscopy. *Marine Chemistry*, 82(3):239–254.

Stedmon, C. A. and Nelson, N. B. (2015). Chapter 10 - The Optical Properties of DOM in the Ocean. In Hansell, D. A. and Carlson, C. A., editors, *Biogeochemistry of Marine Dissolved Organic Matter (Second Edition)*, pages 481–508. Academic Press, Boston.

Steele, M. and Dickinson, S. (2016). The phenology of Arctic Ocean surface warming. *Journal of Geophysical Research: Oceans*, 121(9):6847–6861. _eprint: https://onlinelibrary.wiley.com/doi/pdf/10.1002/2016JC012089.

Steinle, L., Graves, C. A., Treude, T., Ferré, B., Biastoch, A., Bussmann, I., Berndt, C., Krastel, S., James, R. H., Behrens, E., Böning, C. W., Greinert, J., Sapart, C.-J., Scheinert, M., Sommer, S., Lehmann, M. F., and Niemann, H. (2015). Water column methanotrophy controlled by a rapid oceanographic switch. *Nature Geoscience*, 8(5):378–382.

Steinle, L., Maltby, J., Treude, T., Kock, A., Bange, H. W., Engbersen, N., Zopfi, J., Lehmann, M. F., and Niemann, H. (2017). Effects of low oxygen concentrations on aerobic methane oxidation in seasonally hypoxic coastal waters. *Biogeosciences*, 14(6):1631–1645.

Sugimura, Y. and Suzuki, Y. (1988). A high-temperature catalytic oxidation method for the determination of non-volatile dissolved organic carbon in seawater by direct injection of a liquid sample. *Marine Chemistry*, 24(2):105–131.

Sánchez-González, J., García-Otero, N., Moreda-Piñeiro, A., and Bermejo-Barrera, P. (2012). Multi-walled carbon nanotubes — Solid phase extraction for isolating marine dissolved organic matter before characterization by size exclusion chromatography. *Microchemical Journal*, 102:75–82.

Theisen, A. R. and Murrell, J. C. (2005). Facultative Methanotrophs Revisited. *Journal of Bacteriology*, 187(13):4303–4305.

Valentine, D. L. and Reeburgh, W. S. (2000). New perspectives on anaerobic methane oxidation. *Environmental Microbiology*, 2(5):477–484. _eprint: https://onlinelibrary.wiley.com/doi/pdf/10.1046/j.1462-2920.2000.00135.x.

Valle, J., Gonsior, M., Harir, M., Enrich-Prast, A., Schmitt-Kopplin, P., Bastviken, D., Conrad, R., and Hertkorn, N. (2018). Extensive processing of sediment pore water dissolved organic matter during anoxic incubation as observed by high-field mass spectrometry (FTICR-MS). *Water Research*, 129:252–263.

van Krevelen, D. W. (1950). Graphical-statistical method for the study of structure and reaction processes of coal. *Fuel*, 26:269–284.

Vanreusel, A., Andersen, A., Boetius, A., Connelly, D., Cunha, M., Decker, C., Heeschen, K., Hilario, A., Kormas, K., Maignien, L., Olu, K., Pachiadaki, M., Ritt, B., Rodrigues, C., Sarrazin, J., Tyler, P., Van Gaever, S., and Vanneste, H. (2009). Biodiversity of Cold Seep Ecosystems Along the European Margins. *Oceanography*, 22(1):110–127.

Vähätalo, A. V., Aarnos, H., and Mäntyniemi, S. (2010). Biodegradability continuum and

biodegradation kinetics of natural organic matter described by the beta distribution. *Biogeochemistry*, 100(1):227–240.

Wang, W., He, C., Gao, Y., Zhang, Y., and Shi, Q. (2019). Isolation and characterization of hydrophilic dissolved organic matter in waters by ion exchange solid phase extraction followed by high resolution mass spectrometry. *Environmental Chemistry Letters*.

Westbrook, G. K., Thatcher, K. E., Rohling, E. J., Piotrowski, A. M., Pälike, H., Osborne, A. H., Nisbet, E. G., Minshull, T. A., Lanoisellé, M., James, R. H., Hühnerbach, V., Green, D., Fisher, R. E., Crocker, A. J., Chabert, A., Bolton, C., Beszczynska-Möller, A., Berndt, C., and Aquilina, A. (2009). Escape of methane gas from the seabed along the West Spitsbergen continental margin. *Geophysical Research Letters*, 36(15):n/a–n/a.

Whiticar, M. J. (1999). Carbon and hydrogen isotope systematics of bacterial formation and oxidation of methane. *Chemical Geology*, 161(1):291–314.

Wiesenburg, D. A. and Guinasso, N. L. (1979). Equilibrium solubilities of methane, carbon monoxide, and hydrogen in water and sea water. *Journal of Chemical & Engineering Data*, 24(4):356–360.

Åström, E. K. L., Carroll, M. L., Ambrose, W. G., Sen, A., Silyakova, A., and Carroll, J. (2018). Methane cold seeps as biological oases in the high-Arctic deep sea. *Limnology and Oceanography*, 63(S1):S209–S231.

Chapter 2

Paper I

Compositional Differences in Dissolved Organic Matter Between Arctic Cold Seeps Versus Non-Seep Sites at the Svalbard Continental Margin and the Barents Sea

frontiers in Earth Science

ORIGINAL RESEARCH
published: 07 December 2020
doi: 10.3389/feart.2020.552731

Compositional Differences in Dissolved Organic Matter Between Arctic Cold Seeps Versus Non-Seep Sites at the Svalbard Continental Margin and the Barents Sea

Muhammed Fatih Sert[1], Juliana D'Andrilli[2], Friederike Gründger[1,3], Helge Niemann[1,4,5], Mats A. Granskog[6], Alexey K. Pavlov[7,8], Bénédicte Ferré[1] and Anna Silyakova[1]*

[1]CAGE - Centre for Arctic Gas Hydrate, Environment and Climate, Department of Geosciences, UiT the Arctic University of Norway, Tromsø, Norway, [2]Louisiana Universities Marine Consortium, Chauvin, LA, United States, [3]Arctic Research Centre, Department of Biology, Aarhus University, Aarhus, Denmark, [4]NIOZ Royal Institute for Sea Research, Department of Marine Microbiology and Biogeochemistry, and Utrecht University, Texel, Netherlands, [5]Department of Earth Sciences, Faculty of Geosciences, Utrecht University, Utrecht, Netherlands, [6]Norwegian Polar Institute, Fram Centre, Tromsø, Norway, [7]Institute of Oceanology, Polish Academy of Sciences, Sopot, Poland, [8]Akvaplan-niva, Fram Centre, Tromsø, Norway

OPEN ACCESS

Edited by:
Martin Scherwath,
University of Victoria, Canada

Reviewed by:
Kai Mangelsdorf,
Helmholtz Centre Potsdam, Germany
Dong Feng,
Shanghai Ocean University, China

***Correspondence:**
Muhammed Fatih Sert
Muhammed.f.sert@uit.no

Specialty section:
This article was submitted to Biogeoscience, a section of the journal Frontiers in Earth Science

Received: *16 April 2020*
Accepted: *09 November 2020*
Published: *07 December 2020*

Citation:
Sert MF, D'Andrilli J, Gründger F, Niemann H, Granskog MA, Pavlov AK, Ferré B and Silyakova A (2020) Compositional Differences in Dissolved Organic Matter Between Arctic Cold Seeps Versus Non-Seep Sites at the Svalbard Continental Margin and the Barents Sea. Front. Earth Sci. 8:552731. doi: 10.3389/feart.2020.552731

Dissociating gas hydrates, submerged permafrost, and gas bearing sediments release methane to the water column from a multitude of seeps in the Arctic Ocean. The seeping methane dissolves and supports the growth of aerobic methane oxidizing bacteria (MOB), but the effect of seepage and seep related biogeochemical processes on water column dissolved organic matter (DOM) dynamics is not well constrained. We compared dissolved methane, nutrients, chlorophyll, and particulate matter concentrations and methane oxidation (MOx) rates from previously characterized seep and non-seep areas at the continental margin of Svalbard and the Barents Sea in May and June 2017. DOM molecular composition was determined by Electrospray Ionization Fourier-transform ion cyclotron resonance mass spectrometry (FT-ICR MS). We found that the chemical diversity of DOM was 3 to 5% higher and constituted more protein- and lipid-like composition near methane seeps when compared to non-seep areas. Distributions of nutrients, chlorophyll, and particulate matter however, were essentially governed by the water column hydrography and primary production. We surmise that the organic intermediates directly derived from seepage or indirectly from seep-related biogeochemical processes, e.g., MOx, modifies the composition of DOM leading to distinct DOM molecular-level signatures in the water column at cold seeps.

Keywords: methane hydrate, methane oxidation, methane oxidizing bacteria, arctic ocean, Fourier-transform ion cyclotron resonance mass spectrometry, nutrients

INTRODUCTION

Dissolved organic matter (DOM) is the operationally defined mixture of organic compounds that passes through a 0.7 μm pore size filter (Repeta, 2015) and constitutes the largest reservoir of organic carbon in the oceans. Marine DOM has not been chemically characterized explicitly to date but 60–70% of the structural variability has been classified as major functional groups (Carlson and

Hansell, 2015). The distribution and the composition of DOM are mainly controlled by the bioavailability of these groups. The major part (humic acids, condensed aromatics, black carbon etc.) is considered refractory and remains in the water for years or even millennia (Williams and Druffel, 1987; Amon and Benner, 1994; Lechtenfeld et al., 2014). More biologically reactive DOM in the ocean, considered as bio-labile DOM (amino acids, sugars, proteins etc.), is available to heterotrophic microorganisms and rapidly remineralized by prokaryotes in the upper layers of the water column (Carlson et al., 1994; Carlson et al., 2010; Koch et al., 2014). Bio-labile DOM is produced and transformed by numerous biological processes including extracellular release, excretion, cell lysis, solubilisation and chemosynthetic processes (Carlson and Hansell, 2015).

DOM in the ocean is predominantly derived from biological processes, carrying a unique signature, which may comprise a fingerprint of the surrounding ecosystems. One distinct ecosystem of the Arctic Ocean involves cold seeps and methane bearing sediments in which methane emanates from seeps due to dissociation of methane hydrates (Westbrook et al., 2009; Ferré et al., 2012; Berndt et al., 2014; Sahling et al., 2014). Only a limited portion of the seeping methane reaches the atmosphere (Graves et al., 2015; Myhre et al., 2016; Steinle et al., 2016), while the major part remains in the water column as dissolved gas. Concentrations of methane may reach up to thousands times higher than background levels at seeps, yet decreases rapidly with the distance from the point source predominantly as a result of bacterial oxidation, lateral diffusion, and upward mixing (Graves et al., 2015; Silyakova et al., 2020). Microbial oxidation of methane (MOx), performed by methane oxidizing bacteria (MOB) which convert methane into methanol and formaldehyde, is the major removal mechanism of dissolved methane in ocean waters (Reeburgh, 2007; Murrell, 2010). Formaldehyde is then further used in the catabolism (i.e., oxidized to carbon dioxide to supply energy) or in the anabolism (i.e., incorporated into organic compounds to be used as building blocks for growth) (Hanson and Hanson, 1996). Previous culture experiments suggest that MOB produces a variety of organic acids and chemical products as intermediates (Kalyuzhnaya et al., 2013).

The contribution of cold seeps into marine DOM has never been documented despite its potential importance in waters receiving methane from seeps. The main objective of this study is to document the effect of methane seeps on DOM composition at cold seep sites at the continental margins of Svalbard and in the Barents Sea. Our main hypothesis is that methane-driven microbial processes such as MOx and/or seep-associated microbial modifications result in microbial discharge of metabolic intermediates that alter the molecular composition of DOM in the water column at cold seeps.

METHODS

Study Area

We collected samples near methane seepages with various hydrographic properties and bathymetric features during two research expeditions with R/V Helmer Hanssen between 16–29 May (CAGE-17-1) and 23–28 June 2017 (CAGE-17-2). Samples were collected at 18 stations at six different sites (**Figure 1** and **Table 1**) comprising two deep water stations at the Vestnesa Ridge (VR) and Yermak Plateau (YP), eight stations at the shallow shelf west of Prins Karls Forland (PKF), two stations at the southern end of Storfjordrenna (SS), three stations at Storfjordrenna pingos (SP) and three stations at the Olga Basin (OB) in the Barents Sea (**Figure 1**). At all sites, non-seepage stations were also sampled as a control that had similar water masses but only background methane concentrations. Active seeps were located with the ship-mounted EK60 single-beam echosounder. Based on echosounder data, we defined sampling stations that were literally located above active seeps. These stations are considered seep stations, while the others are considered non-seep stations (**Table 1**). The only exception was station PKF-1 which was not exactly located above seeps but surrounded by numerous seeps and located in the flow direction of many others (**Figure 1**).

Sampling and Storage

Seawater was sampled from discrete water depths (**Table 1**) during up-casts of a rosette sampler with 12 × 5 L PTFE lined Niskin bottles and a Sea-Bird 911 plus CTD (Conductivity Temperature Depth) with accuracies of 0.3 db, 0.001°C, and 0.002 for pressure, temperature and salinity, respectively. Dissolved oxygen data were collected using an SBE 43 oxygen sensor (calibrated by Winkler (1888) titration) attached to the CTD. Distribution of chlorophyll fluorescence and turbidity were determined at all stations by Setpoint sensors. All sensor measurements were averaged in 1 m depth bins. Methane and MOx samples were collected immediately after recovery of the rosette on-board. Samples for methane analysis were carefully filled (to prevent bubble formation) into 120 ml (1250 ml for non-seep surface samples) serum bottles amended with 1 M sodium hydroxide solution to stop microbial activity and crimped with butyl rubber septa. Samples were vigorously shaken and stored at 4°C until analysis.

For MOx rate measurements, 20 ml crimp top vials were filled bubble-free with seawater sample, capped with bromobutyl rubber stoppers that do not impede MOx activity (Niemann et al., 2015). Samples were processed immediately after sampling.

Samples for DOM, particulate matter, chlorophyll *a* (Chl *a*), and nutrients were collected in acid-washed (2% HCl) glass bottles (4 × 1000 ml) and stored at 4°C in the dark before processing. Samples were filtered within 6 hours after collection by applying low-pressure vacuum (50 mmHg). Triplicates of particulate matter and Chl *a* samples were collected on GF/F filters (Whatman) using 1 L of water for each sample. Particulate matterfilters were dried and stored at 25°C until X-ray fluorescence analysis. Chl *a* filters were folded twice in half, placed in 10 mL high density polyethylene tubes (HDPE), and stored at −80°C. The filtrate was collected into pre-rinsed 60 ml HDPE bottles, stored at −20°C, and used for the determination of the concentrations of nitrate, nitrite, phosphate, silicate, ammonia, dissolved organic carbon (DOC), total dissolved nitrogen, and total dissolved phosphorus.

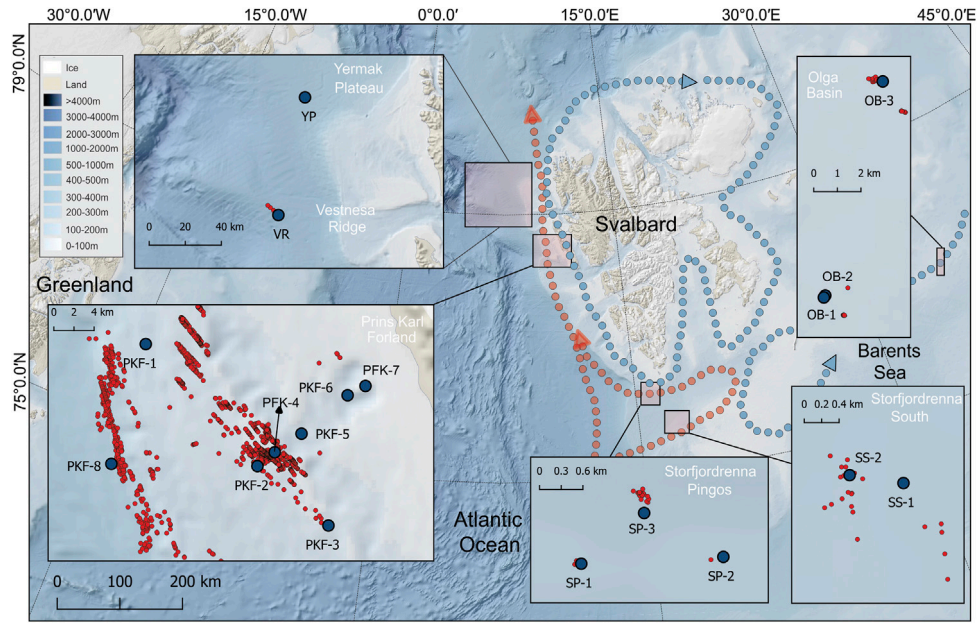

FIGURE 1 | Bathymetric map of sampling areas around Svalbard. Pale red and blue dotted lines show directions of the warm West Spitzbergen Current and cold polar currents, respectively. Five insets are shown to magnify the sampling areas with individual spatial scales along with known methane seeps indicated by the red dots. Sampling stations within the insets are indicated by the blue dots and further information is provided in **Table 1**.

For solid phase extraction DOM 1 L of filtrate was extracted on 500 mg styrene divinyl benzene polymer type cartridges (PPL, BondElut, Agilent Technologies) using a procedure modified from Dittmar et al. (2008). Briefly, filtrates were acidified to pH 2 by HCl (37% v/v, Merck) and transferred into pre-conditioned (6 ml methanol + 12 ml water) solid phase extraction cartridges. Next, 12 ml pH 2 water were flushed through the cartridge and cartridges were dried under air vacuum for 30 min. Concentrated DOM samples were eluted into combusted, Teflon capped amber glass vials by 2 ml methanol and stored at −20°C in the dark until FT-ICR MS analysis.

Biochemical Analyses

Nitrate + nitrite (further nitrate), silicate, phosphate, ammonium, total dissolved nitrogen and total dissolved phosphorus

TABLE 1 | Detailed information of the sampled stations listing sample regions, sampling stations, station location, methane seep characteristic, water depth, and sampling depth of water samples.

Region	Station	Latitude N	Longitude E	Methane seep	Water depth (m)	Sampling depths (m)
Prins Karls Forland	PKF-1	78° 40' 02''	09° 35' 33''	Yes	195	5, 25, 171, 192
	PKF-2	78° 33' 09''	10° 05' 53''	Yes	110	5, 25, 88, 108
	PKF-3	78° 29' 46''	10° 24' 53''	Yes	117	5, 25, 93, 113
	PKF-4	78° 33' 56''	10° 10' 33''	Yes	81	5, 25, 56, 78
	PKF-5	78° 34' 58''	10° 17' 48''	No	122	5, 25, 100, 120
	PKF-6	78° 37' 08''	10° 30' 21''	No	125	5, 25, 103, 123
	PKF-7	78° 37' 39''	10° 35' 13''	No	76	5, 26, 53, 73
	PKF-8	78° 33' 15''	09° 26' 31''	Yes	405	5, 25, 380, 402
Yermak Plateau	YP	79° 37' 33''	07° 30' 12''	No	822	5, 50,131,400,774,817
Vestnesa ridge	VR	79° 00' 05''	06° 56' 49''	Yes	1207	5, 50, 600, 1150, 1195
Storfjorrenna south	SS-1	75° 50' 20''	16° 38' 49''	No	345	5, 50, 170, 295, 340
	SS-2	75° 50' 25''	16° 37' 29''	Yes	350	5, 49, 170, 295, 347
Storfjordrenna pingos	SP-1	76° 06' 24''	15° 58' 05''	Yes	383	7.5, 28, 357, 375
	SP-2	76° 06' 21''	16° 02' 29''	No	386	5, 25, 363, 384
	SP-3	76° 06' 47''	16° 00' 12''	No	387	5, 25, 365, 384
Olga basin	OB-1	76° 46' 53''	35° 11' 28''	No	158	5, 25, 135, 155
	OB-2	76° 46' 51''	35° 11' 15''	No	159	5, 25, 60, 100, 135, 155
	OB-3	76° 51' 04''	35° 25' 57''	Yes	154	5, 25, 60, 130, 150

concentrations were measured colorimetrically (Grasshoff et al., 1999) by a segmented flow nutrient analyzer system (ALPKEM Flow Solution IV, OI Analytical). Dissolved organic nitrogen (DON) and dissolved organic phosphorus (DOP) concentrations were calculated by subtracting concentrations of nitrate + ammonium (DIN; dissolved inorganic nitrogen) from total dissolved nitrogen and phosphate from total dissolved phosphorus.

DOC concentrations were measured based on a high-temperature combustion technique (Qian and Mopper, 1996; Peterson et al., 2003). Unthawed samples were allowed to equilibrate at room temperature and acidified to pH 2 with HCl (37%). 15 ml of sample were then transferred into pre-combusted glass vials of the TOC analyzer (MQ-1001). Deep Ocean DOC samples (Hansell Laboratory, University of Miami) were used as reference material.

Particulate nutrient analyses were measured in triplicates using a method based on wavelength dispersive X-ray fluorescence with a detection limit < 0.1 µg per filter (Paulino et al., 2013) for particulate carbon C, nitrogen (N), and phosphorus (P).

The filters for Chl *a* concentration stored at −80°C were added to 10 ml methanol (Holm-Hansen and Riemann, 1978) and stored overnight at 4°C. Methanol extracted samples were transferred into pre-cleaned vials and maintained at room temperature. Fluorescence of the sample was measured against methanol blanks with recently calibrated Turner Design fluorometer at 440 nm before and after adding two drops of 5% HCl (Holm-Hansen et al., 1965). Final concentrations were determined using a calibration curve of Chl *a* standards.

Quantification of dissolved methane in seawater samples was conducted on-board using headspace gas chromatography (ThermoScientific, GC Trace 1310, FID detector, MSieve 5A column). 5 ml from the 120 ml (1250 ml for low concentration surface waters) sample bottles was replaced with high purity nitrogen and allowed to equilibrate at least for 24 hours. For Headspace GC measurement hydrogen was used as a carrier gas and oven temperature was set to 150°C (isothermal). 500 µl headspace was injected with a gas-tight syringe resulting in a detection limit of 1 ppm and 5% standard deviation. Dissolved methane concentration (nmol/L) was calculated using previously published solubility coefficients (Wiesenburg and Guinasso, 1979). Reproducibility of measurements was controlled with 2 ppm and 100 ppm methane containing air standards.

MOx rates was quantified by tritium labelled incubations (Niemann et al., 2015; Steinle et al., 2015) with modifications as described in Ferré et al. (2020). Briefly, hexaplicates of seawater samples were amended with trace amounts of ^{3}H-methane (10 µl gaseous $C^{3}H_4/N_2$, ~25 kBq, <50 pmol CH_4, American Radiolabeled Chemicals, United States) and incubated for 72 hours at *in situ* temperature in the dark. After following the procedure described in aforementioned publications, MOx rates were calculated from the fractional tracer turnover and *in situ* methane concentrations assuming first order reaction kinetics (Valentine et al., 2001; Reeburgh, 2007). All incubations were corrected for (insubstantial) tracer turnover in killed controls (Steinle et al., 2015).

Fourier-Transform Ion Cyclotron Resonance Mass Spectrometry Analysis and Molecular Formula Assignments

DOM mass spectra were obtained with a custom-built 9.4 T Fourier transform ion cyclotron resonance mass spectrometer (FT-ICR MS) instrument (National High Magnetic Field Laboratory [NHMFL], Tallahassee, Florida, United States). Mass spectra were generated in positive and negative ion electrospray ionization (ESI) mode with the following settings: flow rate 0.5 µL/min, needle voltage ± 2.5 kV, tube lens ± 250 V, heated metal capillary operated at 11.2 W, octopole frequency 2 MHz, frequency sweep rate of 50 Hz/ls and temperature 21.7°C. To generate mass spectra, 50 scans (time domain acquisitions) were co-added for each sample, Hanning apodized, and zero-filled once before fast Fourier transformation and magnitude calculation (Marshall and Verdun, 1990). NHMFL software was used to calibrate the data and generate peak lists for each sample prior to molecular formula assignment. Peak lists were generated with a signal to noise ratio threshold of 6x the baseline root mean square noise and internally calibrated with commonly known DOM methylene ($-CH_2$) compounds spanning across the 200–900 Da mass spectral range. DOM molecular compositions were assigned by PetroOrg (Corilo, 2014). Molecular formula assignments included all possible naturally occurring molecular combinations of C, H, N, O, and S within these ranges: $^{12}C_{1-100}$, $^{1}H_{1-200}$, $^{14}N_{0-2}$, $^{16}O_{1-50}$, and $^{34}S_{0-1}$. Formula confirmation was based on individual monoisotopic mass spectral peaks, error < 1 ppm, and homologous series inclusion, as has been conducted previously for manual composition assignments (D'Andrilli et al., 2015). Sodium and chlorine adducts were also considered during the molecular formula assignment procedure for positive and negative mode, respectively. Assigned molecular formulas were generated for each sample as negative and positive mode except samples PKF-1 at 195 m and SP-1 at 344 m which could not be calibrated in positive mode with acceptable error (<1 ppm). Positive and negative molecular assignments per sample were combined to analyze DOM composition and chemical characterization. For each sample containing duplicate molecular formulas in positive and negative mode, one was discarded from further analysis.

Chemical characterizations for the combined positive and negative formula lists of each sample were conducted to get percentages of 1) atomic heterogeneous contents – CHO, CHNO, CHOS, CHNOS – and 2) H:C and O:C atomic ratios and ranges on van Krevelen diagrams (Kim et al., 2003). Based on the elemental compositions of major biochemical compound groups, specific H:C and O:C ratio ranges were related to four compound classes: 1) lipid- & protein-like (LPD), 2) amino sugar- & carbohydrate-like (CAR), 3) unsaturated hydrocarbon- and condensed aromatic-like (UHC), and 4) lignin- & tannin-like (LGN), whose boundaries were obtained from Hockaday et al. (2009) and Hodgkins et al. (2016) (**Supplementary Table S1**). Samples were also interpreted by the percentages of the formulas above the molecular lability boundary (MLB_L; H:C ≥ 1.5) to compare more bioavailable DOM composition with less bioavailable material across all samples (D'Andrilli et al., 2015).

The aromaticity (or the aromatic fraction) of the samples were calculated using the equation given in Hockaday et al. (2009).

Statistical Analyses

Statistical analyses and data visualization were performed using R (R Core Team, 2018) with built-in functions and external packages: Vegan (Oksanen et al., 2018), FactoMineR (Lê et al., 2008), MASS (Venables and Ripley, 2002), and indicspecies (De Cáceres and Legendre, 2009).

Principal component analysis was applied on measured environmental variables to obtain multiple correlation between samples and variables.

Chemical diversity of the DOM molecular formulas for each sample was calculated by the 'diversity' function in R, which is analogue to biodiversity in ecology, i.e., the Shannon-Weaver index (Oksanen et al., 2018):

$$H = -\sum P_i * log_n(P_i)$$

where P is the relative abundance of formula i.

Non-metric multidimensional scaling (NMDS) analysis was applied in three steps on the molecular formula lists to determine the variation of DOM between samples. First, a presence/absence matrix was constructed (samples on rows and formulas on columns). Second, a dissimilarity matrix was calculated based on Jaccard formulation (Jaccard, 1912) on binary (0 or 1) data (e.g., *[A + B-2*J]/[A + B-J]* where *A* and *B* are number of formulas in two compared samples and *J* is the number of formulas that is common in both samples (Oksanen et al., 2018). Third, an NMDS ordination plot was depicted on two sets of scores in which the separation between the samples was largest. Distribution on the biplot states that closer samples are likely to be more similar than the ones further apart.

Permutational multivariate analysis of variance (PERMANOVA) was calculated on Jaccard distance matrices by using the 'adonis' function in the Vegan package in R (Oksanen et al., 2018). PERMANOVA was used to interpret how DOM compositions were influenced by categorical variables such as regional distribution, water masses and seep/non-seep association.

Indicator value indices (IndVal) of all detected formulas were calculated following a method developed by De Cáceres and Legendre (2009). IndVal is a product of two quantities (*A: group specificity; B: group fidelity*) that allow to define lists of formulas that associated to the predefined groups of sites. Statistical significance (p) of the group association were then tested by permutation test against the null hypothesis that a formula is not more frequently found at a group of sites than at sites not belonging to that group (De Cáceres and Legendre, 2009). A threshold of IndVal ≥ 0.7 and $p \leq 0.01$ were taken under 1000 permutations for group association.

RESULTS

Distribution of Water Masses and Environmental Variables

The studied sites were characterized by five main water masses (**Figure 2**). Three of them were classified within the window of σ_t density 27.70 and 27.97 kg/m^3 (Rudels et al. 2000), with the

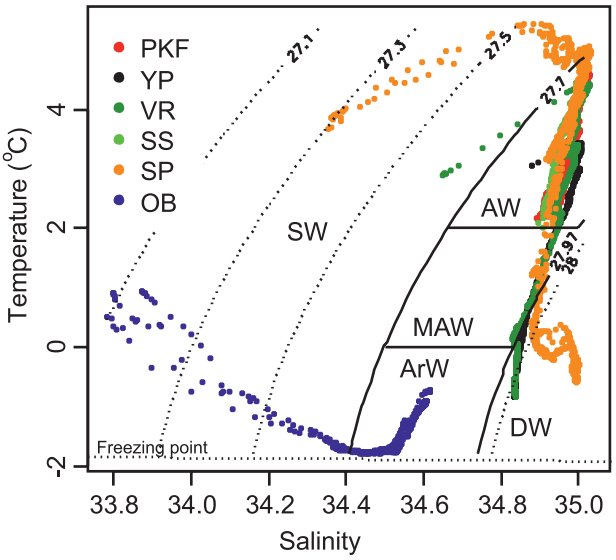

FIGURE 2 | Water mass definitions on temperature vs. salinity diagram from the CTD profiles. 27.70–27.97 kg/m^3 σ_t isoclines separate Surface water (SW) and Deep Water (DW) and 0–2°C horizontal temperature lines separate Atlantic Water (AW) and Arctic Water (ArW) from Modified Atlantic Water (MAW). Colored data points indicate the sample data for each region listed in **Table 1**.

temperature ranges of > 2°C (Atlantic Water; AW), 0–2°C (Modified Atlantic Water; MAW) and < 0°C (Arctic Water; ArW). Waters with $\sigma_t \leq 27.70$ kg/m^3 were considered as surface water (SW) with a wide range of temperature and salinity. Waters that have $\sigma_t > 27.97$ kg/m^3 were classified as Arctic deep water (DW). DW reveals two distinct influences depending on the site location (lower right corner in **Figure 2**). At VR and YP stations the water column was composed of DW that has formed in the polar region and sank below the AW layer. At the lower part of the SP, on the other hand, DW was characterized by higher salinity which were formed in Storfjorden and sank underneath the MAW layer at the southern tip of Spitsbergen (Quadfasel et al., 1988; Loeng, 1991; Fer et al., 2003; Skogseth et al., 2005).

The water column profiles were depicted in **Figure 3** by a selected station from each region that represents typical biogeochemical features. As is shown in the figure, the water column was well-mixed at the shallow stations in the PKF, where AW was the dominant water mass with temperature 2°C and salinity 34.9 throughout the water column (**Figure 3A**). Vertical profiles exhibited clear site-specific patterns for temperature, salinity and density (**Figure 3A**). At VR and YP, AW occupied the 300–350 m upper layer (**Figure 3A**). Underneath, the temperature decreased to 0°C with a strong thermocline and MAW extended to the depth of 500 m in YP and 600 m in VR. Underneath MAW, DW displayed a uniform salinity profile (~34.85) with 0 to −1°C temperature range. Temperature and salinity profiles were distinct in SS and SP despite their proximity (~30 km). SS was fully occupied with AW (4.3°C, ~35 salinity) from the surface down to 150 m; at greater depth, temperature

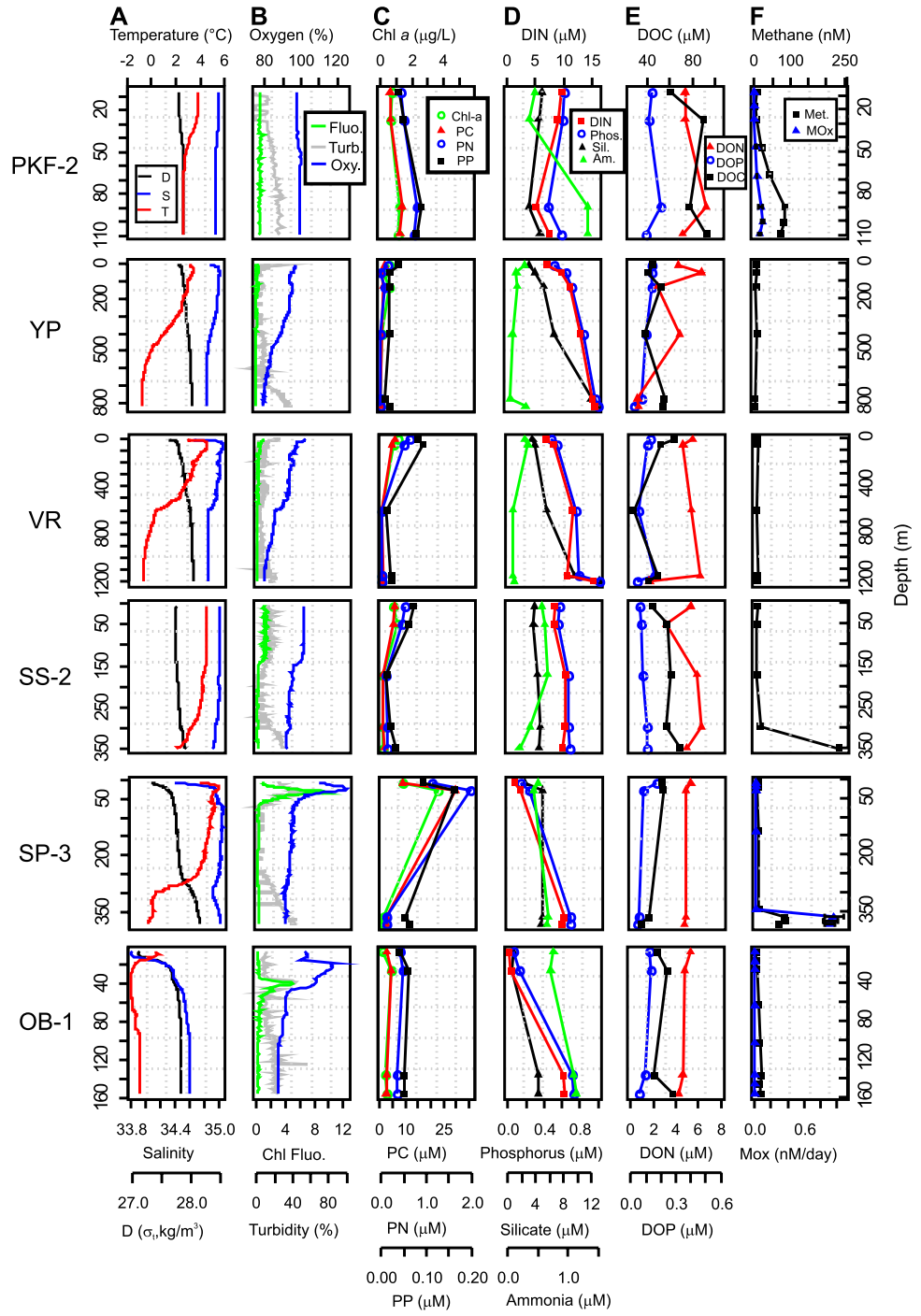

FIGURE 3 | Depth profiles of selected stations. Each row of profiles represents the typical features from regions listed in **Table 1**. Abbreviations are PC, PN, PP, particulate carbon, nitrogen and phosphorus; DOC, DON, DOP, dissolved organic carbon, nitrogen and phosphorus; DIN, dissolved inorganic nitrogen; D, density; T, temperature; S, salinity; Chl Fluo., Chlorophyll fluorescence; Mox, methane oxidation.

decreased slightly to 2°C at the bottom (**Figure 3A**). Three distinct layers were characterized at SP: a cold, fresh surface layer at the top 20–30 m, a warm and saline AW layer from 30 to 300 m, and cold and saline DW from 300 m to the bottom (**Figure 3A**). At the OB site strong Arctic influence was prominent with a two-layered structure, consisting of SW (top 20 m) above a sharp pycnocline and ArW from 30 m to the bottom at ~150 m (**Figure 3A**).

Chl fluorescence did not exhibit any clear peak and were around zero in the water column for May 2017 (CAGE-17-1

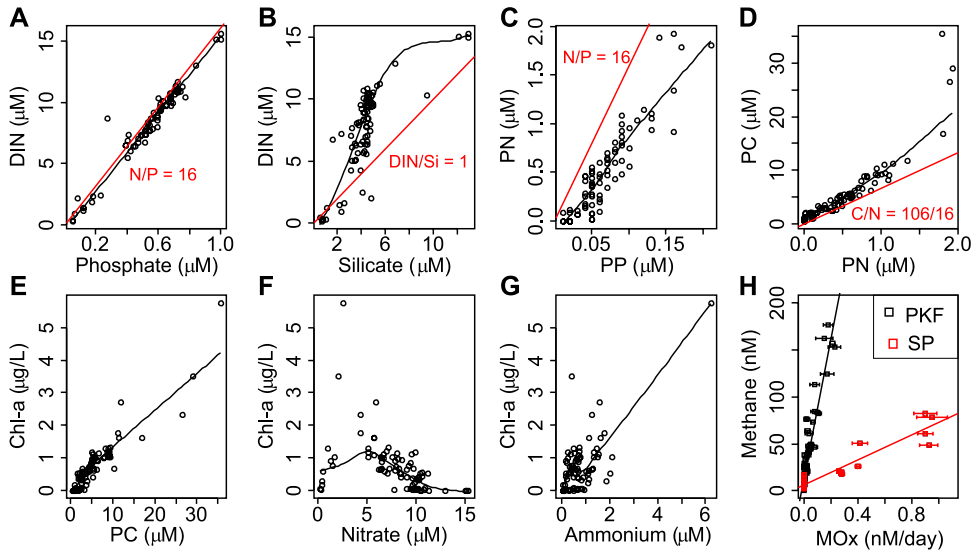

FIGURE 4 | Individual relationships between biogeochemical parameters. The black lines show local polynomial regressions between the variables. Redfield ratios are provided in red at the top panel. The relationship between methane and methane oxidation rates (MOx) and corresponding linear regression lines are provided in black and red corresponding to Prins Karl Forland (PKF) and Storfjordrenna Pingos (SP). Error bars represent standard deviation of MOx measurements. Abbreviations are PC, PN, PP, particulate carbon, nitrogen and phosphorus; DIN, dissolved inorganic nitrogen; Chl-a, Chlorophyll a.

cruise) whereas distinct maxima were detected at SP and OB at 40 m depth in late June (CAGE-17-2 cruise) (**Figure 3B**). This difference in Chl fluorescence signal between the cruises was also detected in surface Chl *a* concentration averages retrieved from satellite data (**Supplementary Figure S1**). To depict a relative distribution of oxygen more accurately, dissolved oxygen concentrations were converted into oxygen saturation assuming that 100% saturation at 1 atm and 4°C corresponds to 10.92 mg/L. Oxygen saturation varied in 92–102% range within AW that occupied PKF and upper layers of VR, YP, and SS and uniformly decreased to 80–85% at the bottom in DW. Along with the peaks in Chl fluorescence signal, oxygen saturation increased up to 110–125% at the upper layers of OB and SP and dropped back to 85–90% in ArW at the bottom layers (**Figure 3B**). Turbidity was elevated at the bottom of the water column at all stations and its profiles were analogous to the fluorescence profiles at the upper layers (**Figure 3B**).

Chl *a* concentrations ranged from 0.00 to 5.75 µg/L (average 0.75 µg/L) (**Supplementary Table S2**) with the highest concentration in SP corresponding with the CTD Chl fluorescence peak at 40 m at this site (**Figure 3C**). Particulate matter concentrations were always in line with the Chl *a* concentrations (**Figure 3C**). Maximum concentrations were measured at SP-1 (28 m) for particulate C (35.64 µM) and particulate N (1.93 µM) and in PKF for particulate P (0.21 µM). Chl *a* vs particulate C, N and P displayed positive linear correlations in all samples (r = 0.93, 0.84, and 0.76, respectively, $p < 0.001$) (**Figures 4C–E**).

Maximum dissolved nutrient concentrations were detected in the DW layer (<800 m; 15.3 µM, 1.00 µM, and 13.0 µM for nitrate, phosphate, and silicate respectively) implying a marked regeneration at depth (**Figure 3D**). We found lowest concentrations at the OB surface likely due to the dilution by sea-ice meltwaters and earlier surface bloom (**Figure 3D**). Here, concentrations dropped to 0.19 µM, 0.05 µM, and 0.54 µM for nitrate, phosphate, and silicate, respectively (**Supplementary Table S2**). Ammonium concentrations varied in a narrow range from 0.04 µM to 2.08 µM in all samples (**Supplementary Table S2**) except the maximum value (6.21 µM) measured at SP-1 (28 m). DIN and phosphate ratios were close to the Redfield ratio (1958) (ratio of carbon: nitrogen: phosphorus as 106:16:1 often found in marine phytoplankton soft tissue) in all samples (**Figure 4**). DIN to silicate ratio however, was higher than one in most of the samples.

Our measurements showed that the variation of DOC, DON, and DOP was low comparing all sites (**Figure 3E** and **Supplementary Table S2**). The DOC concentration range was from 26.9 to 104.0 µM however, 80% of the measurements were between 40 and 80 µM. The highest DOC concentration was measured at the surface layer (0–5 m) of PKF and the minimum concentration was at the surface of the OB. Similar vertical profiles were observed for DON and DOP concentrations with ranges of 0.00–7.43 µM and 0.00–0.60 µM, respectively (**Supplementary Table S2**). On average, DON and DOP contributed 39% and 20% of the total dissolved nitrogen and phosphorus pool, respectively, and highest contributions were measured for OB surface water.

Methane concentrations were often elevated in the vicinity of seeps (**Figure 3F** and **Supplementary Figure S2**). Dissolved methane resulted in high concentrations in the bottom waters and decreased rapidly to atmospheric equilibrium levels except at PKF (**Figure 3F**). Here, numerous seeps were located in shallow waters and methane concentrations were ~five times higher at the surface (14.9 nM) compared to the atmospheric equilibrium (3.2 nM at 34.8 psu and 6°C; (Wiesenburg and Guinasso, 1979)). The highest methane concentration (263 nM) was

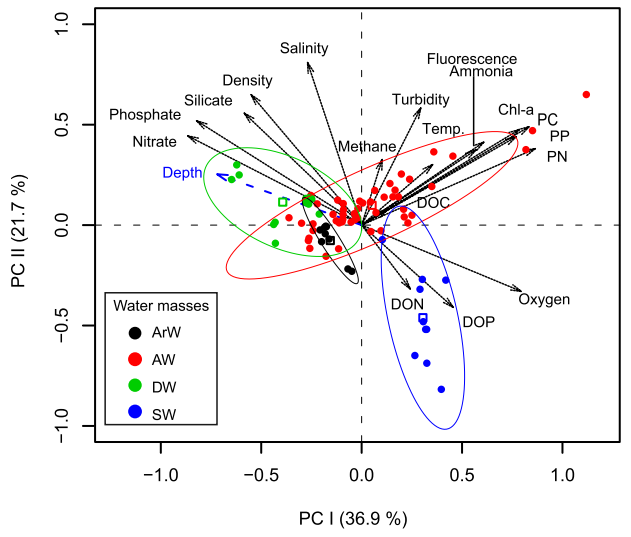

FIGURE 5 | Principle Component Analysis biplot of the biochemical parameters. The explained variances are provided on the x- and y-axis in parentheses. Coloured ellipses represent 95% confidence interval for water mass group centroids of Surface water (SW), Deep Water (DW), Atlantic Water (AW), and Arctic Water (ArW). Centroids are represented by open square symbols. Abbreviations are PC, PN, PP, particulate carbon, nitrogen and phosphorus; DIN, dissolved inorganic nitrogen; DOC, DON, DOP, dissolved organic carbon, nitrogen and phosphorus; Chl-a, Chlorophyll a.

measured at the bottom of SS-2 (**Figure 3F**). Average methane concentrations for all stations were 63 nM (bottom), 39 nM (25 m above seafloor) and 9 nM (5 m below surface).

We measured MOx rates at 96 sampling points at PKF, SP, and OB (**Supplementarys Table S2 and Figure S2A**). Average MOx rates were almost 10 times higher at SP (0.31 nM/day) compared to PKF (0.04 nM/day) and there was no detectable MOx activity at OB (**Figure 3** and **Supplementary Figure S2B**). MOx rates were positively correlated with the methane concentrations in PKF (correlation coefficient r = 0.91, $p < 0.001$, number of sub-samples $n = 64$) and SP (r = 0.94, $p < 0.001$, $n = 32$) separately and showed two different responses (**Figure 4H**).

A principal component analysis of the biochemical parameters displayed a correspondence with the water mass characteristics of the samples within the first two principal components (PC) as 36.9 and 21.7% variance explained, respectively (**Figure 5**). Primary production related parameters (Chl *a*, particulate C, N, P, Chl fluorescence, ammonium) and dissolved nutrients were the main components on the PC-1 which partially represent the separation between DW and AW, whereas SW largely represented by DON, DOP and oxygen concentrations on the PC-2 axis (**Figure 5**).

Dissolved Organic Matter Molecular Composition

From all the sampling sites, 19,641 distinct formulas were obtained after removing the duplicate formulas in positive and negative mode ESI samples with the molecular mass range of 211 to 989 Da (**Figure 6A**). From all assigned formulas, 6,947and 2,356 were unique to seep and non-seep samples respectively (**Figure 6B**), and 10,338 formulas were found in both (**Figure 6C**). All assigned elemental composition varied in the range of $C_{7\text{-}75}H_{6\text{-}74}N_{0\text{-}2}O_{1\text{-}25}S_{0\text{-}1}$ with the percentages of 41% CHO, 39% CHNO, 13% CHNOS, 7% CHOS for seep and 41% CHO, 36% CHNO, 15% CHNOS, 8% CHOS for non-seep samples. Using our modified characterization classification criteria based on H:C and O:C groupings on van Krevelen diagrams, molecular formulas averaged 74% LGN, 8% UHC, 14% LPD, 4% CAR for seep and 76% LGN, 9% UHC, 11% LPD, 4% CAR for non-seep chemical species (**Figure 6B**).

IndVal analysis for seep versus non-seep comparisons of all molecular formulas determined that 922 and 129 formulas were associated with the seep and non-seep samples respectively (**Figure 6D**). That is, the formulas that are more frequently observed in a compound class group (**Supplementary Table S1**) considered as associated. Given that, seep associated formulas (IndVal ≥ 0.7; $p \leq 0.01$) were composed of 72% LGN, 23% LPD, and 5% UHC. Non-seep associated formulas (IndVal ≥ 0.7; $p \leq 0.01$) were predominantly composed of LGN (52%), UHC (43%), and only 6 formulas were assigned CAR (5%) chemical species (**Figure 6D**).

The number of formulas in seep and non-seep samples ranged from 3,211 to 9,534 and from 3,120 to 6,815 respectively (**Figure 7A**). The lowest number of formulas were obtained in the PKF-7 (non-seep) and the highest number of formulas were obtained in PKF-3 (seep) (**Figure 7A**). Samples on the seepage sites of PKF and SS were higher in MLB_L (18 to 27%) compared to the other samples and had characteristically higher LPD chemical species (12 to 21%) (**Figures 7B,C**). CAR and UHC contents were highest in non-seep PKF-7 station (8%) and YP station (14%) comparatively and the greatest percentages of LGN (82%) were observed in OB-1 station (**Figures 7D–F**).

Percentages in CHO and CHOS based formulas were varied in a range from 34 to 49% and 3 to 12%, respectively except the YP bottom sample in which CHOS composition percent was 25% (**Figures 7G–I** and **Supplementary Figure S2**). CHON composition percentages were highest in the PKF and SS seep stations (35 to 43%). CHONS composition percentages were highest (23%) in non-seep PKF-7 station (**Figure 7J**).

NMDS analysis from Jaccard distances based on DOM composition revealed a high level of association at two dimensions (stress = 0.12). Samples from the same site/station displayed similar DOM composition (**Figure 8**). PERMANOVA test on Jaccard distances revealed that DOM compositions were most significantly ($p < 0.001$) associated with station (coefficient of determination $R^2 = 0.59$), site ($R^2 = 0.35$) and seep influence ($R^2 = 0.17$). Environmental variables that showed linear correlation to NMDS ordination scores were temperature, salinity, density, oxygen ($p < 0.001$), methane ($p < 0.019$), and DOC concentrations ($p < 0.028$). NMDS scores displayed significant correlations with chemical diversity, number of formulas, heteroatomic compositions and molecular species compositions of the samples ($p < 0.001$). The most variable DOM composition was found at the PKF seep sites explained by number of formulae and chemical diversity. NMDS biplot revealed that DOM composition of PKF seep samples displayed

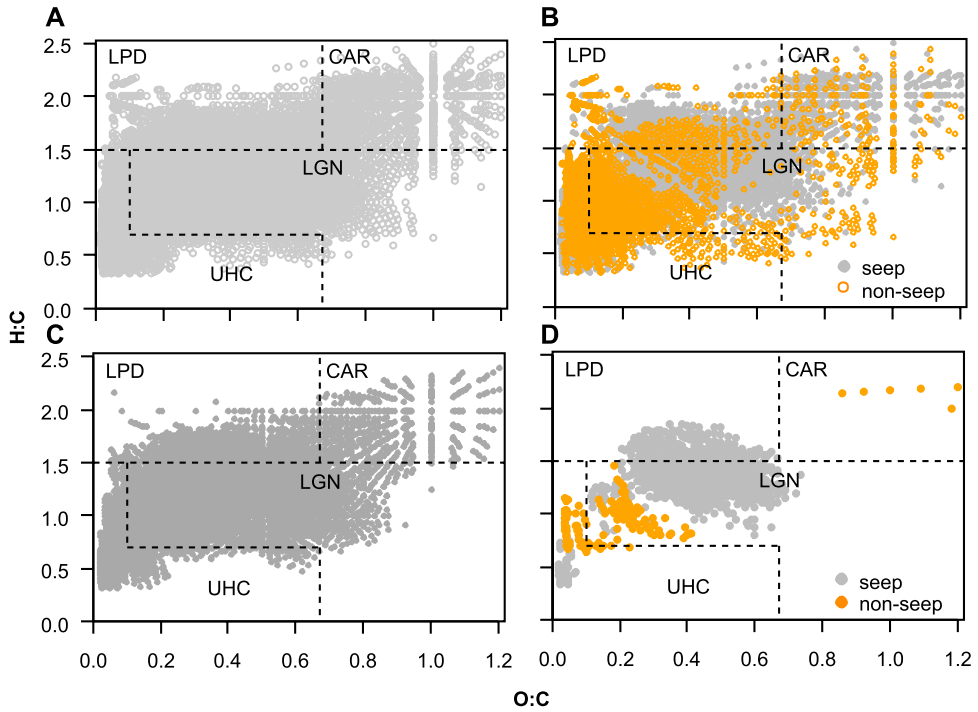

FIGURE 6 | (A) All assigned dissolved organic matter formulas in all samples **(B)** unique molecular formulas that are found in seep (grey) and non-seep (orange) samples **(C)** molecular formulas commonly found in seep and non-seep samples **(D)** Seep versus non-seep associated formulas based on comparisons by IndVal analysis (IndVal ≥ 0.7; $p \leq 0.01$). Each point in the diagrams represents a single formula assigned from one resolved mass spectral peak. Note: these van Krevelen diagrams contain molecular formulas from combined positive and negative mode ESI FT-ICR MS assignments. Abbreviations are LPD, lipid- and protein-like; CAR, carbohydrate-like; LGN, lignin- &tannin-like; UHC, unsaturated hydrocarbon- &condensed aromatic-like; O:C, oxygen to carbon ratio; H:C, hydrogen to carbon ratio.

positive correlation with the percentages of MLB_L, LPD, and CHON compositions (Student's t-test, $p < 0.01$) and OB samples were associated with higher aromaticity, LGN, and CHOS composition (Student's t-test, $p < 0.01$) (**Figure 8**).

DISCUSSION

Oceanographic Characteristics of the Study Sites

As the main driver of the hydrography, the West Spitsbergen Current (WSC) brings AW which gradually mixes with the locally formed cold fjord and shelf waters over the West Spitsbergen Shelf and the Arctic waters in Storfjordrenna and Barents Sea (Loeng, 1991; Harris et al., 1998). Therefore, the water column mainly comprises AW in PKF, VR, YP, SS, and SP sites (**Figure 2**). DW was dominant in the bottom part of YP, VR, SS, and SP (**Figure 3**). OB was the only region that was fully occupied by ArW. SW was present in all regions, except at PKF where the well-mixed water column was entirely occupied by AW.

Nutrients and Chl *a* concentrations were consistent with previous observations in the study sites (Hodal et al., 2012; Tremblay et al., 2015; Randelhoff et al., 2018). Higher nitrate/silicate ratios were apparent in AW (**Figure 4B**) implying earlier diatom uptake based on 1/1 demand on nitrate and silicate (Erga et al., 2014). Nevertheless, AW seems to be the main source of nutrients in virtue of higher average concentrations and well-developed Chl *a* sub-surface maxima in the stratified SP region. Ratio of particulate C/N/P – 83/7.6/1 **Figures 4A–D** in comparison to 106/16/1 - C/N/P Redfield ratio (Redfield, 1958) implies that the nitrogen was the limiting factor on primary production. Yet, the elevation of Chl *a* and the depletion of nitrate were associated with the increase in ammonia presumably by remineralisation and restored DIN/phosphate ratio back to the Redfield ratio of 16 (**Figure 4A**). This is also in agreement with the previous findings (Olsen et al. 2003) that defines depletion of nitrate as an indicator of blooms in AW, whereas phosphate and silicate ranges in similar pattern of variability.

Silicate demanding diatoms are the dominant producer in the upper layer of the ArW during the retraction of sea-ice and gradually sink to the deeper layers (Loeng and Drinkwater, 2007). Accordingly, minimum levels of nitrate/silicate ratios were found in ArW as average 2.57 ± 0.7 with depleted surface nutrients indicating a diatom bloom prior to sampling. As the Chl fluorescence peak at 40 m at OB indicates (**Figure 3B**), the active community of diatoms might have moved along the nitricline in late June.

Bulk concentrations of the dissolved organic matter (DOC, DON, DOP) did not indicate any distinct trend within the studied samples (**Figure 3E**). High percentages of LPD content and N-containing formulas at PKF were not directly correlated with the

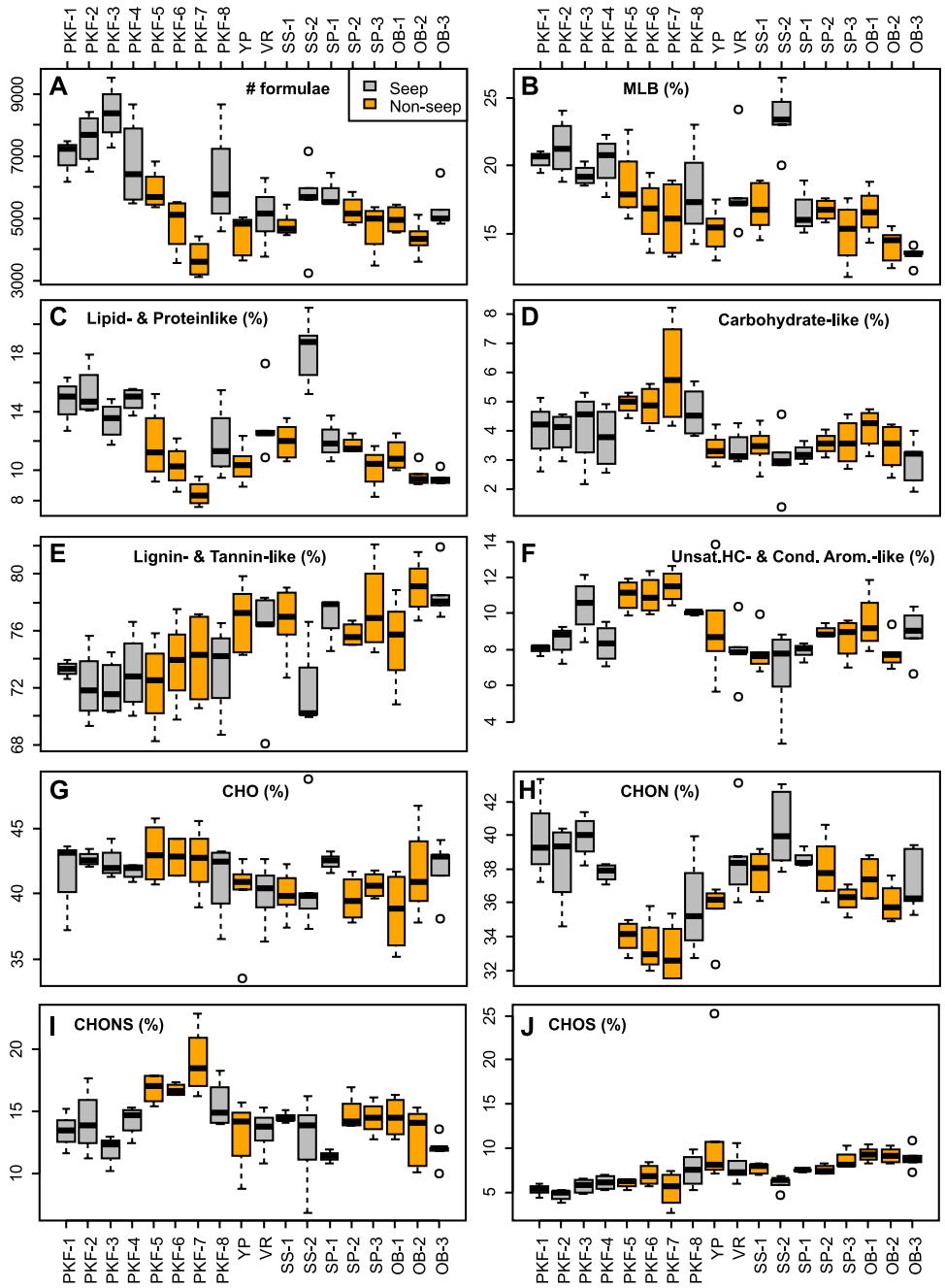

FIGURE 7 | Dissolved organic matter composition data determined by ESI FT-ICR MS organized by sampling stations shown as boxplots for **(A)** number of molecular formulas, **(B)** percentages of chemical lability (MLB_L; D'Andrilli et al., 2015) **(C–F)** chemical groups based on modified regions of characterization classes on van Krevelen diagrams (**Figure 2**), and **(G–J)** and heteroatomic content. Seep and non-seep stations are colored by grey and orange, respectively. Stations are abbreviated as given in **Table 1**.

bulk DON concentrations. As a proxy to primary production, Chl *a* concentrations did not show any detectable correlation with the DOM compositions. Chl peaks at SP and the previous diatom bloom at OB were not linked with any unique DOM composition. A similar DOM molecular composition can arise from many biotic processes and these findings may be due to the simultaneous bacterial consumption that follows bio-labile, autochthonous production of DOM. This result is consistent with the previous observation by Osterholz et al. (2014) in Arctic fjords which suggested rapid transformation of DOM by the microbial community without any detectable imprint in neither DOM compositions nor bulk concentrations.

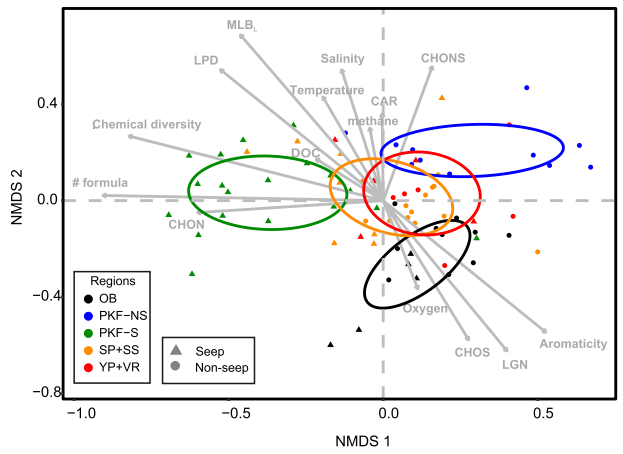

FIGURE 8 | Non-metric multidimensional scaling (NMDS) biplot of Jaccard distances from the presence/absence matrix of dissolved organic matter molecular formula compositions containing $C_cH_hN_nO_oS_s$ by ESI FT-ICR MS. Samples are coded by colour and shape for site and seepage influence, respectively. Arrow vectors represent environmental variables (oxygen, DOC, temperature, salinity, and methane concentration), numerical observations (number of formulas, chemical diversity, aromaticity (Hockaday et al., 2009)) and molecular percentages (CHOS, CHON, CHONS, LPD, LGN, CAR, MLB_L,) that show significant correlation ($p < 0.05$) with the NMDS scores. Coloured ellipses represent 95% confidence interval of the group centroids. Abbreviations are LPD, lipid- and protein-like; CAR, carbohydrate-like; LGN, lignin-&tannin-like; UHC, unsaturated hydrocarbon- &condensed aromatic-like; DOC, dissolved organic carbon; MLB_L, percentages of formulas above the molecular lability boundary (D'Andrilli et al. 2015).

Effect of Hydrography on Methane Concentrations and Methane Oxidation Distributions

Spatial and temporal variability of MOx was shown to be high on the continental margin of Svalbard and at PKF in previous studies where MOx rates were reported between 0.001 and up to 3.2 nM/day (Steinle et al., 2015; Ferré et al., 2020). Our MOx rates from the PKF site (max 0.23 nM/day) were low compared to overall ranges (**Supplementary Table S2**). Rather than elevated methane concentrations, which were not entirely related to high MOx rates, the size of a MOB community may be the more relevant factor of an active MOB community (Steinle et al., 2015). Moreover, the succession of MOB communities depends largely on circulation patterns and water column hydrography (Steinle et al., 2015; Silyakova et al., 2020). In accordance with this, we observed in our study site-specific positive correlations between methane concentrations and MOx rates at PKF and SP (**Figure 4H**). MOx was 10 times more efficient at SP (rate constant $k_{MOx} = 6 \times 10^{-3}\,day^{-1}$) than in PKF ($k_{MOx} = 6 \times 10^{-4}\,ay^{-1}$), presumably due to the difference in the hydrography or the size of methanotrophic community. At SP, a well-defined pycnocline (**Figure 4A** SP-3 panel) hindered the transport of gas bubbles to upper layers (Damm et al., 2005; Damm et al., 2008; Gentz et al., 2014; Jansson et al., 2019) whereas the vertical transport of methane was easier in uniform and shallow water column at PKF (**Figure 4A** PKF-2 panel).

Notably, water column stratification and the size of the MOB were possibly not the only parameters affecting MOB efficiency. Since MOx activity was rapidly exhausted at the bottom of SP well before reaching the pycnocline (~100 m above bottom; **Figure 3F** SP-3 panel). Water mass distribution and current regimes were different between sites. DW occupied the bottom of SP, whereas PKF was entirely composed of AW (**Figure 3A**). As previously reported, PKF is influenced by WSC with a strong monthly mean current velocity of 0.2 m/s (von Appen et al., 2016) continuously transporting MOB populations northwards out of the PKF area (Graves et al., 2015; Steinle et al., 2015). In contrast, the mean geostrophic velocity at SP is in the range of 0.02–0.07 m/s (Skogseth et al., 2005; Skogseth et al., 2007). Longer residence times possibly facilitates MOB to metabolize methane more efficiently, therefore higher MOx rates were observed at SP (**Figure 3F**). MOx was undetected in OB even above the seeps with high methane concentrations (**Figure 3F**) indicating that a substantial active population of MOB in OB was not present (note that we did not determine MOB community sizes in our survey).

Evaluation of Dissolved Organic Matter Compositions

Analysis of DOM with ESI FT-ICR MS provides a qualitative assessment of molecular-level elemental composition linked to the ionization efficiency of polar constituents of the sample and experimental settings. Using ESI FT-ICR MS, we determined chemical composition, interpreted chemical characteristics, and evaluated the presence or absence of molecular formulas to qualitatively understand DOM composition in the water column at the different sampling sites.

DOM molecular composition patterns were consistent with those of previous reports (Hertkorn et al., 2013; Osterholz et al., 2014; D'Andrilli et al., 2015; Kujawinski et al., 2016), having characteristically large percentages of LGN compounds (68–82%, **Figures 6**, **7E**). Although the FT-ICR MS instrument does not generate structural DOM data, naturally occurring chemical possibilities of CHNOS molecular formula indicate the potential for polycarboxylated substances such as lignins, tannins, terpenes, and carboxyl-rich alicyclic molecules (CRAM) that share similar structural information with a wide range of eukaryotic and prokaryotic membrane constituents and secondary metabolites (Hertkorn et al., 2006). These groups of chemical species are derived from decades of accumulated microbial degradation products which ultimately lead to similar compositional patterns in many marine environments (Koch et al., 2005).

Formulas interpreted as LPD and CAR (12 to 27%, **Figures 6**, **7B–D**) with more hydrogen saturation (H:C ≥ 1.5) are considered to comprise of bio-labile species (D'Andrilli et al., 2015) and likely indicate recent autochthonous microbial production (hours to days). Bio-labile DOM is considered to be most energetically favorable for microbial uptake or for extracellular degradation (Koch et al., 2014; Carlson and Hansell, 2015) and therefore its chemical composition provides insight about the potential biological patterns of seep versus non-seep sites. Accordingly, LPD chemical species were found with greater atomic heterogeneity in seep sites (**Figures 7G–J**) indicating higher

potential for seep-driven microbial activity (Kujawinski, 2011; D'Andrilli et al., 2019).

Three to 14% of the formulas were interpreted as UHC in all samples and similarly represented in seep and non-seep stations (**Figure 7F**). DOM of this type is most likely generated by legacy sinking of refractory materials (from a microbial perspective), undergoing no further biological degradation, e.g., the end-products of biomass combustion or petrogenic/pyrogenic origin, which were thermally fused in the deep layers of sediment and mechanically brought up into the water column by bubbles and seeping fluids.

All DOM sample molecular compositions were predominantly grouped by site and seep influence (**Figure 8**). The largest dissimilarity in molecular composition was between the PKF-S (seep stations in PKF) and PKF-NS (non-seep stations in PKF) sites across NMDS-1 axis which correlated with the number of formulas, N-containing composition (see **Figure 7H**) and chemical diversity (**Figure 8**). On the diagonal axis between NMDS-1 and NMDS-2, OB DOM composition grouped separately with explained differences positively correlating with the aromaticity, oxygen, CHOS content, and LGN composition. That diagonal axis also implies the correlation of MLB_L and LPD composition with the seep samples in PKF and SS. Therefore, we relate higher number of molecular formulas, chemical diversity, CHON composition, and LPD chemical species to unique DOM production at the seep sites. This pattern was most pronounced at PKF-S possibly due to prevalent seepage activity combined with strong ventilation at the shallow water column. We observed a similar pattern also at SS-2 where DOM composition displayed considerably high percentages of bio-labile nature (LPD) compared to the non-seep station SS-1 (**Figure 7C**). This provides evidence that seep-related microbial processes may have a significant influence on DOM composition with more bio-labile and nitrogen composition.

We suggest that the combination of positive and negative mode ESI contributed greatly to identifying distinct DOM molecular formulas at seep and non-seep sites. CHO and CHON chemical species were more efficiently ionized in positive ESI (**Supplementary Figure S5**) and provided a more comprehensive analysis of the DOM composition of all samples. Negative ESI is more frequently used in marine DOM research due to its better ionization efficiency of acidic and carboxylic compounds (Sleighter and Hatcher, 2007). However, more information about the polar fraction of marine DOM as well as other natural environments is gained by combining positive and negative ESI FT-ICR MS data sets (Hertkorn et al., 2013; Ohno et al., 2016).

In addition, positive ESI FT-ICR MS also detected unique CHOS composition near the bottom of the YP station (**Supplementary Figure S4**). These chemical species can be considered as 'black sulphur' due to compositional similarity with black carbon and black nitrogen in the condensed aromatics region of the van Krevelen diagram having large hydrogen deficiency and limited oxygenation (Hertkorn et al., 2013; Hertkorn et al., 2016). Although the origin of these chemical species is not known, high sulfur content suggests that anoxic sedimentary microbial processes may play a role in their production.

Do Cold Seeps Alter Dissolved Organic Matter Composition?

Cold seeps in the Arctic Ocean originate from a variety of sources and geochemical mechanisms (Bünz et al., 2012; Sahling et al., 2014; Serov et al., 2015; Andreassen et al., 2017; Panieri et al., 2017). Seeping fluids consist of predominantly methane (99.7–99.9%), yet other hydrocarbons and sulphurous compounds may also migrate with seeping fluids and methane, all of which provide a source for chemosynthetic organisms (Levin, 2005; Vanreusel et al., 2009; Panieri et al., 2017; Sen et al., 2018; Åström et al., 2018). Seeping gases form bubbles and rise up through the water column (Westbrook et al., 2009; Berndt et al., 2014). Along its trajectory towards the upper layers, methane exchanges with more abundant dissolved gases such as nitrogen, enriched in the surrounding water and promotes MOx (James et al., 2016; Steinle et al., 2016; Jansson et al., 2019). Hydroacoustic surveys demonstrated that seeps can stay active for weeks to decades (Gentz et al., 2014; Veloso-Alarcón et al., 2019) however, the fate of methane at active flares sites is highly dependent on bubble size, salinity, and water velocity (Jansson et al., 2019). Therefore, considering the effects of ocean currents, upwelling, or redox changes, availability of methane for MOB can be sporadic and the potential rates may not be maintained persistently (Reeburgh, 2007; Mau et al., 2013; Steinle et al., 2015; Steinle et al., 2016; Steinle et al., 2017). For this reason, seep influence on DOM composition was not always directly linked to methane concentration, and seep versus non-seep definition was solely based on echosounder data. Since MOx is the main removal mechanism of dissolved methane in the water column, low concentration of methane at seep stations (e.g., VR) may indicate efficient microbial filtering which eliminates methane simultaneous to its dispersion. Oppositely, high concentration of methane at non-seep stations (e.g., SP-3, PKF-5, and PKF-6; see **Supplementary Figure S2A**) may indicate inefficiency of MOx or advection of MOB by currents.

We found a significant correlation between seep activity and DOM composition in terms of its bio-lability, chemical diversity, number of formulas and LPD as well as CHON formula contents (**Figures 7**, **8**). Naturally, MOx is a likely mechanism driving variation in DOM compositions at seep and non-seep stations. However, correlation between seep activity and DOM composition was not observed directly by MOx rates or methane concentrations (**Supplementary Figure S2**). For instance, despite the differences in DOM compositions, non-seep stations in PKF and SP had similar ranges of MOx rates with the seep stations in the same sites (**Supplementary Figure S2B**). One possible explanation may be the dynamic hydrography and consequent elimination of MOx in the region (Steinle et al., 2015). All observed ranges of methane concentrations and MOx rates were low during our survey compared to the results reported at Berndt et al. (2014) and Steinle et al. (2015) and slightly higher than Ferré et al. (2020). However, it is possible that distinct DOM composition associated with MOx activity would persist even if MOB communities diminished, MOx rates decreased, and lower concentrations of methane were measured. In effect, this may lead to a "legacy" fingerprint of methane-influenced DOM composition in the water column, which may be considerably diverse. Therefore, we

attribute the largest variety of DOM compositions for seep vs. non-seep comparisons to a multitude of biogeochemical factors rather than one driving variable such as MOx rates or methane concentration. This effect was most noticeable at PKF where the contrast in seepage activity (number of active seeps; see **Figure 1**) and DOM composition was highly variable from seep to non-seep locations.

Although we hypothesised that MOx would be the main cause of the compositional differences of DOM in seep sites to non-seep sites, other mechanisms may contribute to DOM signatures such as seep-driven primary production. Pohlman et al. (2017) showed that the carbon dioxide uptake rate was two times higher at the seep site of PKF than at the non-seep coastal site. They suggested that stimulation of primary production and consequent decrease of the carbon dioxide level were enhanced with the contribution of methane-enriched bottom waters. The compositional differences we observed might support this hypothesis since more bio-labile and heterogeneous composition may be an indication of fresh primary production at the seep site. However, similar to the MOx rates and methane concentrations, Chl *a* concentration, Chl fluorescence, or nutrient concentrations did not display any noticeable trend from seep to non-seep sites (**Supplementary Figure S1**).

Seeping DOM is another possible mechanism for the compositional differences at seep and non-seep sites. Sedimentary methanotrophic microbes are predominantly anaerobic (Knittel and Boetius, 2009) and likely produce chemical species, different from the metabolites released from active MOB in the overlaying methane-rich water masses. Sedimentary-derived metabolites reach the upper water layers by ventilation due to the upstream of bubbles and vertical mixing, thereby potentially modifying the DOM composition at seep sites. Seeping DOM and consequent compositional differences were previously shown in hydrothermal vents by stable carbon isotope analyses, highlighting the role of crustal microbial communities in DOM synthesis, strong enough to change the compositional character of the overlying ocean (McCarthy et al., 2011). Similarly, Pohlman et al., (2011) showed the contribution of sedimentary DOC flux from methane hydrate seeps to the deep seawater. However, both studies indicated that carbon flux from the sediment was ^{14}C-depleted, considerably aged (5,000 to 15,000 years) and possibly consisting of recalcitrant nature which may be contributing to the LGN chemical species observed at the seep sites.

Lastly, DOM composition may be affected by seep-driven microbial modifications. For instance, continuous methane flow from the seafloor might disturb higher trophic level organisms which feed on DOM consumers and autochthonous DOM producers enumerate rapidly above seeps. To our knowledge, this theory has not been previously studied at seep sites. However, in glucose augmented incubation experiments, Kujawinski et al. (2016) showed that organisms larger than 1.0 μm dominantly affected the bacterial diversity and the DOM composition in seawater. They found that the DOM composition was comprised of lipid- and peptide-like chemical species in <1.0 μm filtered surface sea water during the nine days incubation. Unfortunately, despite the number of studies on MOB taxonomy (Kalyuzhnaya et al., 2019), DOM composition coupling with other microbes and higher organisms remains unknown.

Overall, the mechanisms of different DOM compositions at seep and non-seep sites are likely a combination of many factors. MOx, seep fertilization, seep-driven microbial modifications, and seeping of sedimentary DOM are identified here as possible factors. DOM reflects a number of geochemical and molecular processes on different timescales and potentially years of aggregation whereas seep-driven processes are site specific and may only persist on shorter timescales. Therefore, the modification of DOM by seep-driven processes and relative contribution on total water column biogeochemistry is difficult to capture *in situ* when the other factors are not constrained. Controlled experiments with constrained effects may target the exact products more specifically.

SUMMARY AND CONCLUSION

Cold seeps are being studied intensively due to the possible influence of escaping methane on atmospheric gas compositions and consequent effect on global climate change. Our investigation in the water column showed that the direct and indirect impacts of seeping fluids are also evident for water column biogeochemical concentrations and DOM composition. Our findings at cold seeps of the continental shelf of Svalbard and in the Barents Sea revealed that DOM composition is associated with methane influenced water column activity and spatial distribution of active seeps. DOM appeared more bio-labile and had higher chemical diversity and LPD composition at seeps compared to non-seep areas. Compositional differences of DOM between seep and non-seep sites might be related to a multitude of environmental factors such as MOx, seep fertilization, seep-driven microbial modifications, and seeping of sedimentary DOM. However, no single process was identified as the sole mechanism for unique DOM composition at these sites. DOM composition did not directly correlate to Chl *a*, nutrient concentration, or water temperature, but the hydrography and the nutrient distributions confirmed the local influences of main water masses and primary production cycles.

The underlying mechanisms of seep influence on DOM compositions are yet to be elaborated in controlled laboratory experiments. In order to link the production and consumption of DOM composition to certain seep-specialized microbial groups, incubation experiments with controlled variables (e.g., microbial cultures, temperatures, methane and nutrient concentrations) and further metabolomics analyses on microbe vs. DOM interactions are needed. Expectedly, combinations of all ongoing processes and co-occurring microbial consortia are extremely complex and possibly hinder identifiable interactions on DOM compositions, however in our study, we showed that unique seep DOM compositions and character can be identified. We recommend the analysis technique of ultrahigh resolution mass spectrometry that we used for our analyses as a

promising tool to decipher methane seep associated patterns at the molecular level. Moreover, our combination of biological and chemical techniques provided insight into methane-driven biogeochemical DOM processes in the ocean water column.

DATA AVAILABILITY STATEMENT

The data and the code for statistical analyses are available in the UiT Open Research Data repository in Sert et al. (2020).

AUTHOR CONTRIBUTIONS

MS, FG, AS, and HN designed the study. MS, FG, and HN collected samples. FG and HN measured methane oxidation rates. JD analyzed dissolved organic matter samples, generated formula lists and wrote mass spectrometry methodology. MS wrote the paper with considerable input from JD, FG, HN, MG, AP, BF, and AS.

FUNDING

This study is funded by the Research Council of Norway through CAGE (Centre for Gas Hydrate, Environment and Climate) project number 223259. The publication charges for this article have been funded by a grant from the publication fund of UiT The Arctic University of Norway. AP and MG were supported by the Norwegian Polar Institute and the Polish-Norwegian Research Programme operated by the National Centre for Research and Development under the Norwegian Financial Mechanism 2009–2014 in the frame of project contract Pol–Nor/197511/40/ 2013, CDOM-HEAT.

ACKNOWLEDGMENTS

We would like to acknowledge the crew of R/V Helmer Hanssen during the cruises CAGE-17-1 and CAGE-17-2 and chief scientists Tine Rasmussen and Giuliana Panieri. We thank Colin A. Stedmon for DOC concentration analyses and valuable discussion on DOM dynamics. Authors would like to thank Jorun Karin Egge, Sigrid Øygarden, Matteus Lindgren, and Linda Fonnes Lunde for the analyses of particulate matter, chlorophyll *a*, methane and nutrients. FT-ICR mass spectra were generated at the National High Magnetic Field Laboratory (NHMFL), Tallahassee, FL, United States, supported by funding through the National Science Foundation Division of Materials Research 1644779 and the State of Florida. We acknowledge Dr. Rebecca Ware and the Ion Cyclotron Resonance Facility Staff at the NHMFL for FT-ICR MS instrument support and data processing challenges.

SUPPLEMENTARY MATERIAL

The Supplementary Material for this article can be found online at: https://www.frontiersin.org/articles/10.3389/feart.2020.552731/full#supplementary-material.

REFERENCES

Amon, R. M. W., and Benner, R. (1994). Rapid cycling of high-molecular-weight dissolved organic matter in the ocean. *Nature* 369, 549–552. doi:10.1038/369549a0

Andreassen, K., Hubbard, A., Winsborrow, M., Patton, H., Vadakkepuliyambatta, S., Plaza-Faverola, A., et al. (2017). Massive blow-out craters formed by hydrate-controlled methane expulsion from the Arctic seafloor. *Science* 356, 948–953. doi:10.1126/science.aal4500

Åström, E. K. L., Carroll, M. L., Ambrose, W. G., Sen, A., Silyakova, A., and Carroll, J. (2018). Methane cold seeps as biological oases in the high-Arctic deep sea. *Limnol. Oceanogr.* 63, S209–S231. doi:10.1002/lno.10732

Berndt, C., Feseker, T., Treude, T., Krastel, S., Liebetrau, V., Niemann, H., et al. (2014). Temporal constraints on hydrate-controlled methane seepage off svalbard. *Science* 343, 284–287. doi:10.1126/science.1246298

Bünz, S., Polyanov, S., Vadakkepuliyambatta, S., Consolaro, C., and Mienert, J. (2012). Active gas venting through hydrate-bearing sediments on the vestnesa ridge, offshore w-svalbard. *Mar. Geol.* 332-334, 189–197. doi:10.1016/j.margeo.2012.09.012

Carlson, C. A., Ducklow, H. W., and Michaels, A. F. (1994). Annual flux of dissolved organic carbon from the euphotic zone in the northwestern Sargasso Sea. *Nature* 371, 405–408. doi:10.1038/371405a0

Carlson, C. A., Hansell, D. A., Nelson, N. B., Siegel, D. A., Smethie, W. M., Khatiwala, S., et al. (2010). Dissolved organic carbon export and subsequent remineralization in the mesopelagic and bathypelagic realms of the north atlantic basin. *Deep Sea Res. Part II Top. Stud. Oceanogr.* 57, 1433–1445. doi:10.1016/j.dsr2.2010.02.013

Carlson, C. A., and Hansell, D. A. (2015). "Chapter 3 - DOM sources, sinks, reactivity, and budgets," in *Biogeochemistry of marine dissolved organic matter*. 2nd Edn, Editors D. A. Hansell and C. A. Carlson (Boston, MA: Academic Press), 65–126.

Corilo, Y. (2014). *PetroOrg software*. Tallahassee, FL: Florida State University, Omics LLC.

Damm, E., Mackensen, A., Budéus, G., Faber, E., and Hanfland, C. (2005). Pathways of methane in seawater: plume spreading in an Arctic shelf environment (SW-Spitsbergen). *Continent. Shelf Res.* 25, 1453–1472. doi:10.1016/j.csr.2005.03.003

Damm, E., Kiene, R. P., Schwarz, J., Falck, E., and Dieckmann, G. (2008). Methane cycling in Arctic shelf water and its relationship with phytoplankton biomass and DMSP. *Mar. Chem.* 109, 45–59. doi:10.1016/j.marchem.2007.12.003

De Cáceres, M., and Legendre, P. (2009). Associations between species and groups of sites: indices and statistical inference. *Ecology* 90, 3566–3574. doi:10.1890/08-1823.1

Dittmar, T., Koch, B., Hertkorn, N., and Kattner, G. (2008). A simple and efficient method for the solid-phase extraction of dissolved organic matter (SPE-DOM) from seawater. *Limnol. Oceanogr. Methods* 6, 230–235. doi:10.4319/lom.2008.6

D'Andrilli, J., Cooper, W. T., Foreman, C. M., and Marshall, A. G. (2015). An ultrahigh-resolution mass spectrometry index to estimate natural organic matter lability: FTICRMS organic matter molecular lability index. *Rapid Commun. Mass Spectrom.* 29, 2385–2401. doi:10.1002/rcm.7400

D'Andrilli, J., Junker, J. R., Smith, H. J., Scholl, E. A., and Foreman, C. M. (2019). DOM composition alters ecosystem function during microbial processing of isolated sources. *Biogeochemistry* 142 (2), 281–298. doi:10.1007/s10533-018-00534-5

Erga, S. R., Ssebiyonga, N., Hamre, B., Frette, Ø., Rey, F., and Drinkwater, K. (2014). Nutrients and phytoplankton biomass distribution and activity at the Barents Sea polar front during summer near hopen and storbanken. *J. Mar. Syst.* 130, 181–192. doi:10.1016/j.jmarsys.2012.12.008

Fer, I., Skogseth, R., Haugan, P. M., and Jaccard, P. (2003). Observations of the storfjorden overflow. *Deep Sea Res. Oceanogr. Res. Pap.* 50, 1283–1303. doi:10.1016/S0967-0637(03)00124-9

Ferré, B., Jansson, P. G., Moser, M., Serov, P., Portnov, A., Graves, C. A., et al. (2020). Reduced methane seepage from Arctic sediments during cold bottom-water conditions. *Nat. Geosci.* 13, 144–148. doi:10.1038/s41561-019-0515-3

Ferré, B., Mienert, J., and Feseker, T. (2012). Ocean temperature variability for the past 60 years on the norwegian-svalbard margin influences gas hydrate stability on human time scales: bottom water temperature and gas hydrate. *J. Geophys. Res. Oceans* C10017. doi:10.1029/2012jc008300

Gentz, T., Damm, E., Schneider von Deimling, J., Mau, S., McGinnis, D. F., and Schlüter, M. (2014). A water column study of methane around gas flares located at the West Spitsbergen continental margin. *Continent. Shelf Res.* 72, 107–118. doi:10.1016/j.csr.2013.07.013

Grasshoff, K., Kremling, K., and Ehrhardt, M. (1999). *Methods of seawater analysis. 3rd, completely revised and enlarged edition*. New York, NY: Wiley VCH.

Graves, C. A., Steinle, L., Rehder, G., Niemann, H., Connelly, D. P., Lowry, D., et al. (2015). Fluxes and fate of dissolved methane released at the seafloor at the landward limit of the gas hydrate stability zone offshore western svalbard: dissolved methane OFF western svalbard. *J. Geophys. Res. Oceans* 120, 6185–6201. doi:10.1002/2015JC011084

Hanson, R. S., and Hanson, T. E. (1996). Methanotrophic bacteria. *Microbiol. Rev.* 60, 439–471. doi:10.1128/mmbr.60.2.439-471

Harris, C. L., Plueddemann, A. J., and Gawarkiewicz, G. G. (1998). Water mass distribution and polar front structure in the western Barents Sea. *J. Geophys. Res.* 103, 2905–2917. doi:10.1029/97JC02790

Hertkorn, N., Benner, R., Frommberger, M., Schmitt-Kopplin, P., Witt, M., Kaiser, K., et al. (2006). Characterization of a major refractory component of marine dissolved organic matter. *Geochem. Cosmochim. Acta* 70, 2990–3010. doi:10.1016/j.gca.2006.03.021

Hertkorn, N., Harir, M., Koch, B. P., Michalke, B., and Schmitt-Kopplin, P. (2013). High-field NMR spectroscopy and FTICR mass spectrometry: powerful discovery tools for the molecular level characterization of marine dissolved organic matter. *Biogeosciences* 10, 1583–1624. doi:10.5194/bg-10-1583-2013

Hertkorn, N., Harir, M., Cawley, K. M., Schmitt-Kopplin, P., and Jaffé, R. (2016). Molecular characterization of dissolved organic matter from subtropical wetlands: a comparative study through the analysis of optical properties, NMR and FTICR/MS. *Biogeosciences* 13, 2257–2277. doi:10.5194/bg-13-2257-2016

Hockaday, W. C., Purcell, J. M., Marshall, A. G., Baldock, J. A., and Hatcher, P. G. (2009). Electrospray and photoionization mass spectrometry for the characterization of organic matter in natural waters: a qualitative assessment. *Limnol. Oceanogr. Methods* 7, 81–95. doi:10.4319/lom.2009.7.81

Hodal, H., Falk-Petersen, S., Hop, H., Kristiansen, S., and Reigstad, M. (2012). Spring bloom dynamics in Kongsfjorden, Svalbard: nutrients, phytoplankton, protozoans and primary production. *Polar Biol.* 35, 191–203. doi:10.1007/s00300-011-1053-7

Hodgkins, S. B., Tfaily, M. M., Podgorski, D. C., McCalley, C. K., Saleska, S. R., Crill, P. M., et al. (2016). Elemental composition and optical properties reveal changes in dissolved organic matter along a permafrost thaw chronosequence in a subarctic peatland. *Geochem. Cosmochim. Acta* 187, 123–140. doi:10.1016/j.gca.2016.05.015

Holm-Hansen, O., Lorenzen, C. J., Holmes, R. W., and Strickland, J. D. H. (1965). Fluorometric determination of chlorophyll. *ICES J. Mar. Sci.* 30, 3–15. doi:10.1093/icesjms/30.1.3

Holm-Hansen, O. and Riemann, B. (1978). Chlorophyll a determination: improvements in methodology. *Oikos* 30, 438–447. doi:10.2307/3543338

Jaccard, P. (1912). The distribution of the flora in the alpine zone.1. *New Phytol.* 11, 37–50. doi:10.1111/j.1469-8137.1912.tb05611.x

James, R. H., Bousquet, P., Bussmann, I., Haeckel, M., Kipfer, R., Leifer, I., et al. (2016). Effects of climate change on methane emissions from seafloor sediments in the Arctic Ocean: a review. *Limnol. Oceanogr.* 61, S283–S299. doi:10.1002/lno.10307

Jansson, P., Ferré, B., Silyakova, A., Dølven, K. O., and Omstedt, A. (2019). A new numerical model for understanding free and dissolved gas progression toward the atmosphere in aquatic methane seepage systems: marine two-phase gas model in one dimension. *Limnol. Oceanogr. Methods* 17, 223. doi:10.1002/lom3.10307

Kalyuzhnaya, M. G., Gomez, O. A., and Murrell, J. C. (2019). "The methane-oxidizing bacteria (methanotrophs)," in *Taxonomy, genomics and ecophysiology of hydrocarbon-degrading microbes handbook of hydrocarbon and lipid microbiology*. Editor T. J. McGenity (Cham, Switzerland: Springer International Publishing), 1–34.

Kalyuzhnaya, M. G., Yang, S., Rozova, O. N., Smalley, N. E., Clubb, J., Lamb, A., et al. (2013). Highly efficient methane biocatalysis revealed in a methanotrophic bacterium. *Nat. Commun.* 4, 2785. doi:10.1038/ncomms3785

Kim, S., Kramer, R. W., and Hatcher, P. G. (2003). Graphical method for analysis of ultrahigh-resolution broadband mass spectra of natural organic matter, the van krevelen diagram. *Anal. Chem.* 75, 5336–5344. doi:10.1021/ac034415p

Knittel, K., and Boetius, A. (2009). Anaerobic oxidation of methane: progress with an unknown process. *Annu. Rev. Microbiol.* 63, 311–334. doi:10.1146/annurev.micro.61.080706.093130

Koch, B. P., Kattner, G., Witt, M., and Passow, U. (2014). Molecular insights into the microbial formation of marine dissolved organic matter: recalcitrant or labile?. *Biogeosciences* 11, 4173–4190. doi:10.5194/bg-11-4173-2014

Koch, B. P., Witt, M., Engbrodt, R., Dittmar, T., and Kattner, G. (2005). Molecular formulae of marine and terrigenous dissolved organic matter detected by electrospray ionization Fourier transform ion cyclotron resonance mass spectrometry. *Geochem. Cosmochim. Acta* 69, 3299–3308. doi:10.1016/j.gca.2005.02.027

Kujawinski, E. B. (2011). The impact of microbial metabolism on marine dissolved organic matter. *Annu. Rev. Mar. Sci.* 3, 567–599. doi:10.1146/annurev-marine-120308-081003

Kujawinski, E. B., Longnecker, K., Barott, K. L., Weber, R. J. M., and Kido Soule, M. C. (2016). Microbial community structure affects marine dissolved organic matter composition. *Front. Mar. Sci.* 3. doi:10.3389/fmars.2016.00045

Lê, S., Josse, J., and Husson, F. (2008). FactoMineR: a package for multivariate analysis. *J. Stat. Software* 25, 1–18. doi:10.18637/jss.v025.i01

Lechtenfeld, O. J., Kattner, G., Flerus, R., McCallister, S. L., Schmitt-Kopplin, P., and Koch, B. P. (2014). Molecular transformation and degradation of refractory dissolved organic matter in the Atlantic and Southern Ocean. *Geochem. Cosmochim. Acta* 126, 321–337. doi:10.1016/j.gca.2013.11.009

Levin, L. A. (2005). Ecology of cold seep sediments: interactions of fauna with flow, chemistry and microbes. *Oceanogr. Mar. Biol.* 43, 1–46. doi:10.1201/9781420037449-3

Loeng, H., and Drinkwater, K. (2007). An overview of the ecosystems of the Barents and Norwegian Seas and their response to climate variability. *Deep Sea Res. Part II Top. Stud. Oceanogr.* 54, 2478–2500. doi:10.1016/j.dsr2.2007.08.013

Loeng, H. (1991). Features of the physical oceanographic conditions of the Barents Sea. *Polar Res.* 10, 5–18. doi:10.3402/polar.v10i1.6723

Marshall, A. G., and Verdun, F. R. (1990). *Fourier transforms in NMR, optical, and mass spectrometry*. Amsterdam, Netherlands: Elsevier.

Mau, S., Blees, J., Helmke, E., Niemann, H., and Damm, E. (2013). Vertical distribution of methane oxidation and methanotrophic response to elevated methane concentrations in stratified waters of the arctic fjord storfjorden (Svalbard, Norway). *Biogeosciences* 10, 6267–6278. doi:10.5194/bg-10-6267-2013

McCarthy, M. D., Beaupré, S. R., Walker, B. D., Voparil, I., Guilderson, T. P., and Druffel, E. R. M. (2011). Chemosynthetic origin of 14C-depleted dissolved organic matter in a ridge-flank hydrothermal system. *Nat. Geosci.* 4, 32–36. doi:10.1038/ngeo1015

Murrell, J. C. (20101953–1966). "The aerobic methane oxidizing bacteria (methanotrophs)," in *Handbook of hydrocarbon and lipid microbiology*. Editor K. N. Timmis (Berlin, Heidelberg: Springer).

Myhre, C. L., Ferré, B., Platt, S. M., Silyakova, A., Hermansen, O., Allen, G., et al. (2016). Extensive release of methane from Arctic seabed west of Svalbard during summer 2014 does not influence the atmosphere. *Geophys. Res. Lett.* 43, 4624. doi:10.1002/2016GL068999

Niemann, H., Steinle, L., Blees, J., Bussmann, I., Treude, T., Krause, S., et al. (2015). Toxic effects of lab-grade butyl rubber stoppers on aerobic methane oxidation. *Limnol. Oceanogr. Methods* 13, 40–52. doi:10.1002/lom3.10005

Ohno, T., Sleighter, R. L., and Hatcher, P. G. (2016). Comparative study of organic matter chemical characterization using negative and positive mode electrospray ionization ultrahigh-resolution mass spectrometry. *Anal. Bioanal. Chem.* 408, 2497–2504. doi:10.1007/s00216-016-9346-x

Oksanen, J., Blanchet, F. G., Friendly, M., Kindt, R., Legendre, P., McGlinn, D., et al. (2018). Vegan: community ecology package. Available at: https://CRAN.R-project.org/package=vegan.

Olsen, A., Johannessen, T., and Rey, F. (2003). On the nature of the factors that control spring bloom development at the entrance to the Barents Sea and their interannual variability. *Sarsia* 88, 379–393. doi:10.1080/00364820310003145

Osterholz, H., Dittmar, T., and Niggemann, J. (2014). Molecular evidence for rapid dissolved organic matter turnover in Arctic fjords. *Mar. Chem.* 160, 1–10. doi:10.1016/j.marchem.2014.01.002

Panieri, G., Bünz, S., Fornari, D. J., Escartin, J., Serov, P., Jansson, P., et al. (2017). An integrated view of the methane system in the pockmarks at Vestnesa Ridge, 79°N. *Mar. Geol.* 390, 282–300. doi:10.1016/j.margeo.2017.06.006

Paulino, A. I., Heldal, M., Norland, S., and Egge, J. K. (2013). Elemental stoichiometry of marine particulate matter measured by wavelength dispersive X-ray fluorescence (WDXRF) spectroscopy. *J. Mar. Biol. Ass.* 93, 2003–2014. doi:10.1017/S0025315413000635

Peterson, M. L., Lang, S. Q., Aufdenkampe, A. K., and Hedges, J. I. (2003). Dissolved organic carbon measurement using a modified high-temperature combustion analyzer. *Mar. Chem.* 81, 89–104. doi:10.1016/S0304-4203(03)00011-2

Pohlman, J. W., Bauer, J. E., Waite, W. F., Osburn, C. L., and Chapman, N. R. (2011). Methane hydrate-bearing seeps as a source of aged dissolved organic carbon to the oceans. *Nat. Geosci.* 4, 37–41. doi:10.1038/ngeo1016

Pohlman, J. W., Greinert, J., Ruppel, C., Silyakova, A., Vielstädte, L., Casso, M., et al. (2017). Enhanced CO2 uptake at a shallow Arctic Ocean seep field overwhelms the positive warming potential of emitted methane. *Proc. Natl. Acad. Sci. U.S.A.* 114, 5355–5360. doi:10.1073/pnas.1618926114

Qian, J., and Mopper, K. (1996). Automated high-performance, high-temperature combustion total organic carbon analyzer. *Anal. Chem.* 68, 3090–3097. doi:10.1021/ac960370z

Quadfasel, D., Rudels, B., and Kurz, K. (1988). Outflow of dense water from a svalbard fjord into the fram strait. *Deep Sea Res. Part A. Oceanogr. Res. Papers* 35, 1143–1150. doi:10.1016/0198-0149(88)90006-4

R Core Team (2018). *R: a language and environment for statistical computing*. Vienna, Austria: R Foundation for Statistical Computing.

Randelhoff, A., Reigstad, M., Chierici, M., Sundfjord, A., Ivanov, V., Cape, M., et al. (2018). Seasonality of the physical and biogeochemical hydrography in the inflow to the arctic ocean through fram strait. *Front. Mar. Sci.* 5, 224. doi:10.3389/fmars.2018.00224

Redfield, A. (1958). The biological control of chemical factors in the environment. *Sci. Prog.* 11, 150–170.

Reeburgh, W. S. (2007). Oceanic methane biogeochemistry. *Chem. Rev.* 107, 486–513. doi:10.1021/cr050362v

Repeta, D. J. (2015). "Chapter 2–chemical characterization and cycling of dissolved organic matter," in *Biogeochemistry of marine dissolved organic matter*. 2nd Edn, Editors D. A. Hansell and C. A. Carlson (Boston, MA: Academic Press), 21–63.

Rudels, B., Meyer, R., Fahrbach, E., Ivanov, V. V., Østerhus, S., Quadfasel, D., et al. (2000). Water mass distribution in fram strait and over the Yermak Plateau in summer 1997. *Ann. Geophys.* 18, 687–705. doi:10.1007/s00585-000-0687-5

Sahling, H., Römer, M., Pape, T., Bergès, B., dos Santos Fereirra, C., Boelmann, J., et al. (2014). Gas emissions at the continental margin west of Svalbard: mapping, sampling, and quantification. *Biogeosciences* 11, 6029–6046. doi:10.5194/bg-11-6029-2014

Sen, A., Åström, E. K. L., Hong, W.-L., Portnov, A., Waage, M., Serov, P., et al. (2018). Geophysical and geochemical controls on the megafaunal community of a high Arctic cold seep. *Biogeosciences* 15, 4533–4559. doi:10.5194/bg-15-4533-2018

Serov, P., Portnov, A., Mienert, J., Semenov, P., and Ilatovskaya, P. (2015). Methane release from pingo-like features across the South Kara Sea shelf, an area of thawing offshore permafrost. *J. Geophys. Res. Earth Surf.* 120, 1515–1529. doi:10.1002/2015JF003467

Sert, M. F., D'Andrilli, J., Gründger, F., Niemann, H., Granskog, M. A., Pavlov, A. K., et al. (2020). Replication data for: arctic cold seeps alter dissolved organic matter composition at the svalbard continental margin and the barents Sea. doi:10.18710/JHB371

Silyakova, A., Jansson, P., Serov, P., Ferré, B., Pavlov, A. K., Hattermann, T., et al. (2020). Physical controls of dynamics of methane venting from a shallow seep area west of svalbard. *Continent. Shelf Res.* 194, 104030. doi:10.1016/j.csr.2019.104030

Skogseth, R., Haugan, P. M., and Jakobsson, M. (2005). Watermass transformations in storfjorden. *Continent. Shelf Res.* 25, 667–695. doi:10.1016/j.csr.2004.10.005

Skogseth, R., Sandvik, A. D., and Asplin, L. (2007). Wind and tidal forcing on the meso-scale circulation in Storfjorden, Svalbard. *Continent. Shelf Res.* 27, 208–227. doi:10.1016/j.csr.2006.10.001

Sleighter, R. L., and Hatcher, P. G. (2007). The application of electrospray ionization coupled to ultrahigh resolution mass spectrometry for the molecular characterization of natural organic matter. *J. Mass Spectrom.* 42, 559–574. doi:10.1002/jms.1221

Steinle, L., Graves, C. A., Treude, T., Ferré, B., Biastoch, A., Bussmann, I., et al. (2015). Water column methanotrophy controlled by a rapid oceanographic switch. *Nat. Geosci.* 8, 378–382. doi:10.1038/ngeo2420

Steinle, L., Maltby, J., Treude, T., Kock, A., Bange, H. W., Engbersen, N., et al. (2017). Effects of low oxygen concentrations on aerobic methane oxidation in seasonally hypoxic coastal waters. *Biogeosciences* 14, 1631–1645. doi:10.5194/bg-14-1631-2017

Steinle, L., Schmidt, M., Bryant, L., Haeckel, M., Linke, P., Sommer, S., et al. (2016). Linked sediment and water-column methanotrophy at a man-made gas blowout in the North Sea: implications for methane budgeting in seasonally stratified shallow seas: linked sediment and water methanotrophy. *Limnol. Oceanogr.* 61, S367–S386. doi:10.1002/lno.10388

Tremblay, J.-É., Anderson, L. G., Matrai, P., Coupel, P., Bélanger, S., Michel, C., et al. (2015). Global and regional drivers of nutrient supply, primary production and CO2 drawdown in the changing arctic ocean. *Prog. Oceanogr.* 139, 171–196. doi:10.1016/j.pocean.2015.08.009

Valentine, D. L., Blanton, D. C., Reeburgh, W. S., and Kastner, M. (2001). Water column methane oxidation adjacent to an area of active hydrate dissociation, Eel River Basin. *Geochem. Cosmochim. Acta* 65, 2633–2640. doi:10.1016/s0016-7037(01)00625-1

Vanreusel, A., Andersen, A., Boetius, A., Connelly, D., Cunha, M., Decker, C., et al. (2009). Biodiversity of cold seep ecosystems along the european margins. *Oceanography* 22, 110–127. doi:10.5670/oceanog.2009.12

Veloso-Alarcón, M. E., Jansson, P., Batist, M. D., Minshull, T. A., Westbrook, G. K., Pälike, H., et al. (2019). Variability of acoustically evidenced methane bubble emissions offshore western svalbard. *Geophys. Res. Lett.* 46, 9072–9081. doi:10.1029/2019GL082750

Venables, W. N., and Ripley, B. D. (2002). *Modern applied statistics with S. Fourth*. New York, NY: Springer.

von Appen, W.-J., Schauer, U., Hattermann, T., and Beszczynska-Möller, A. (2016). Seasonal cycle of mesoscale instability of the West spitsbergen current. *J. Phys. Oceanogr.* 46, 1231–1254. doi:10.1175/JPO-D-15-0184.1

Westbrook, G. K., Thatcher, K. E., Rohling, E. J., Piotrowski, A. M., Pälike, H., Osborne, A. H., et al. (2009). Escape of methane gas from the seabed along the West Spitsbergen continental margin. *Geophys. Res. Lett.* 36 L15608. doi:10.1029/2009gl039191

Wiesenburg, D. A., and Guinasso, N. L. (1979). Equilibrium solubilities of methane, carbon monoxide, and hydrogen in water and sea water. *J. Chem. Eng. Data* 24, 356–360. doi:10.1021/je60083a006

Williams, P. M., and Druffel, E. R. M. (1987). Radiocarbon in dissolved organic matter in the central north pacific ocean. *Nature* 330, 246–248. doi:10.1038/330246a0

Winkler, L. W. (1888). Die bestimmung des im wasser gelösten sauerstoffes. *Ber. Dtsch. Chem. Ges.* 21, 2843–2854. doi:10.1002/cber.188802102122

Conflict of Interest: The authors declare that the research was conducted in the absence of any commercial or financial relationships that could be construed as a potential conflict of interest.

frontiers

Supplementary Material

1 Supplementary Figures and Tables

Table S1. Classification of the assigned molecular formulas based on O:C and H:C ratio ranges (Hockaday et al., 2009; Hodgkins et al., 2016). See Fig. 6 for boundaries on van Krevelen diagram.

Classification on O:C and H:C ratios

Compound class	O:C range	H:C range
Lipid- & protein-like (LPD)	≤ 0.67	≥ 1.5
Aminosugar- and carbohydrate-like (CAR)	> 0.67	≥ 1.5
Unsaturated hydrocarbon- & condensed aromatic-like (UHC)	0.1< & <0.67	0.7-1.5 & <0.7
Lignin- & tannin-like (LGN)	> 0.1 & >0.7	0.7-1.5 & <1.5

Table S2. Summary table of the obtained measurements demonstrating number of measurements (n), minimum (min), maximum (max), mean and median values.

	n	Min	Max	Mean	Median
Depth (m)	5410	6	1196	287.5	193
Temperature (°C)	5410	-1.78	5.43	2.22	2.74
Salinity	5410	33.78	35.03	34.90	34.95
Density (σ_t, kg/m^3)	5410	27.08	28.13	27.85	27.85
Oxygen (%)	5410	78.58	125.54	92.86	93.24
Chl Fluo.	5410	0.00	12.38	0.34	0.06
Turbidity (%)	5410	0.00	0.65	0.11	0.09
Chl *a* (µg/l)	80	0.00	5.75	0.75	0.61
PC (µM)	80	0.51	35.64	5.57	4.22
PN (µM)	80	0.00	1.93	0.51	0.45
PP (µM)	80	0.01	0.21	28.04	11.90
DIN (µM)	80	0.35	15.64	8.39	8.91
Nitrate (µM)	80	0.19	15.34	7.61	8.14
Phosphorus (µM)	80	0.05	1.00	0.55	0.59
Silicate (µM)	80	0.54	12.96	4.27	4.35
Ammonia (µM)	80	0.04	6.21	0.77	0.64
DOC (µM)	80	26.90	104.00	56.90	56.30
DON (µM)	80	0.00	7.43	4.65	4.89
DOP (µM)	80	0.00	0.60	0.12	0.10
Methane (nM)	133	0.70	230.80	28.11	13.60
MOx (nM/day)	96	0.00	0.95	0.08	0.01

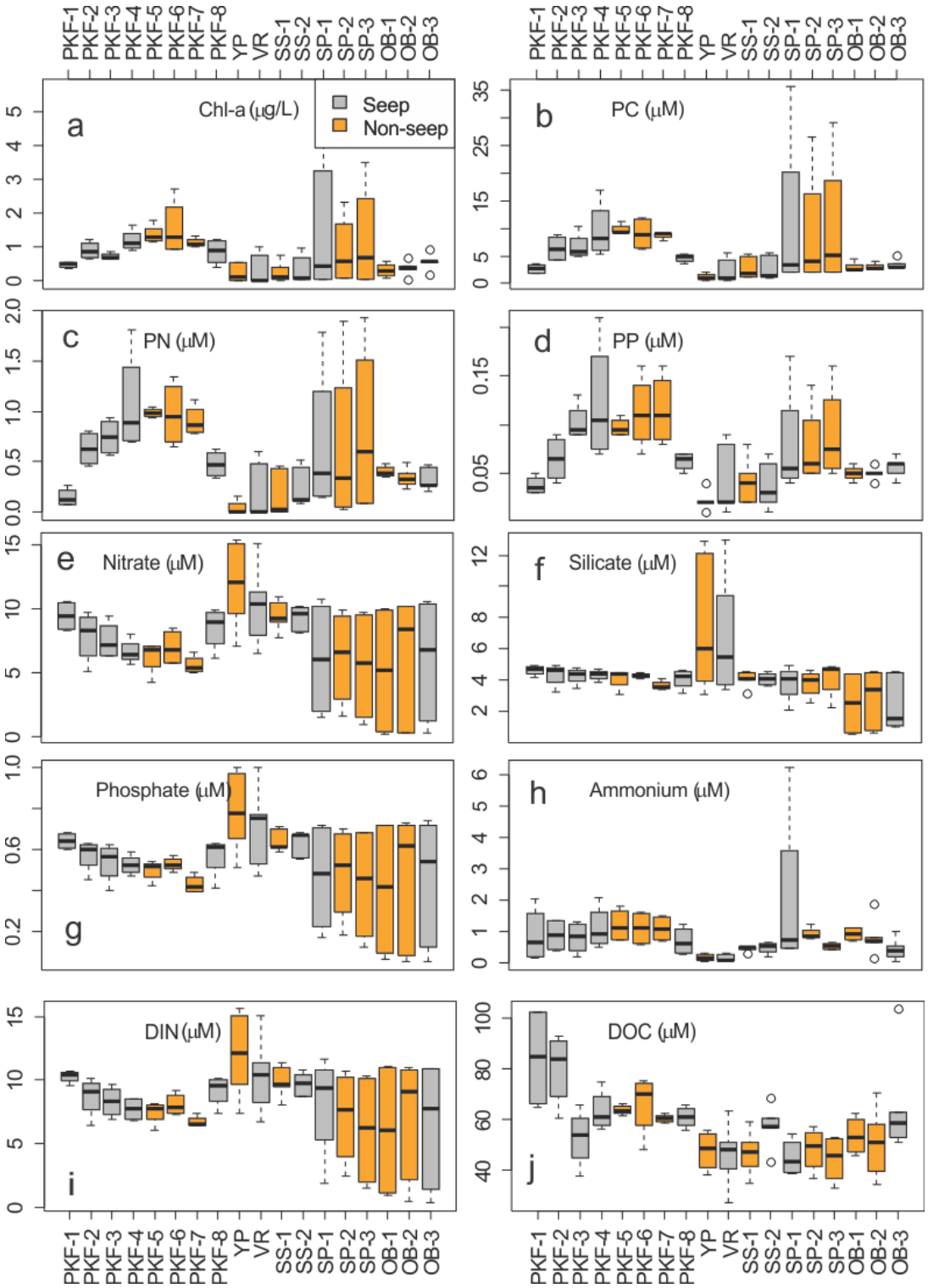

Figure S1: Distribution of environmental parameters organized by sampling stations shown as boxplots. Seep and non-seep stations are colored by grey and orange, respectively. Abbreviations are PC, PN, PP: particulate carbon, nitrogen and phosphorus, DIN: dissolved inorganic nitrogen, DOC: dissolved organic carbon, Chl-a.: Chlorophyll a. Stations are abbreviated as given in Table 1.

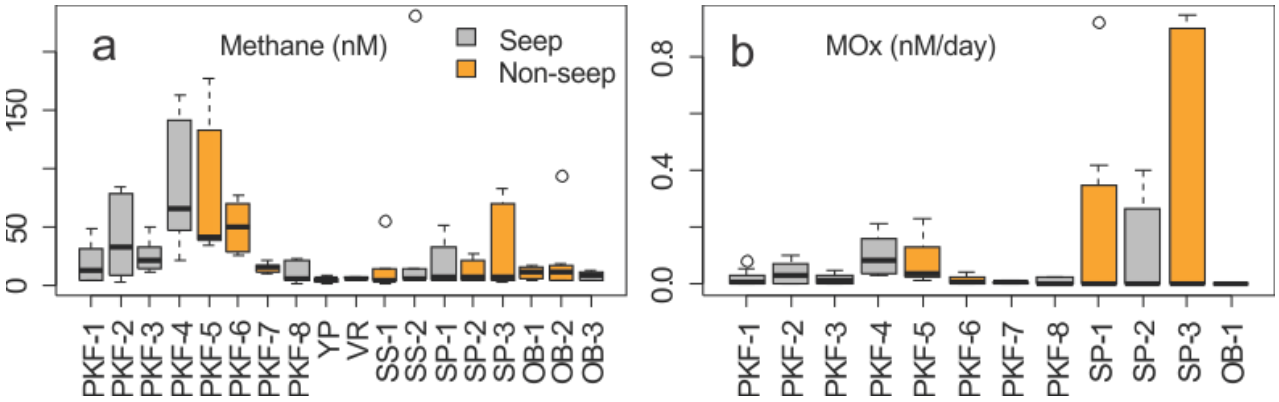

Figure S2: (a) Methane concentrations and (b) methane oxidation rates (MOx) at sampling stations. Seep and non-seep stations are colored by grey and orange, respectively. Stations are abbreviated as given in Table 1.

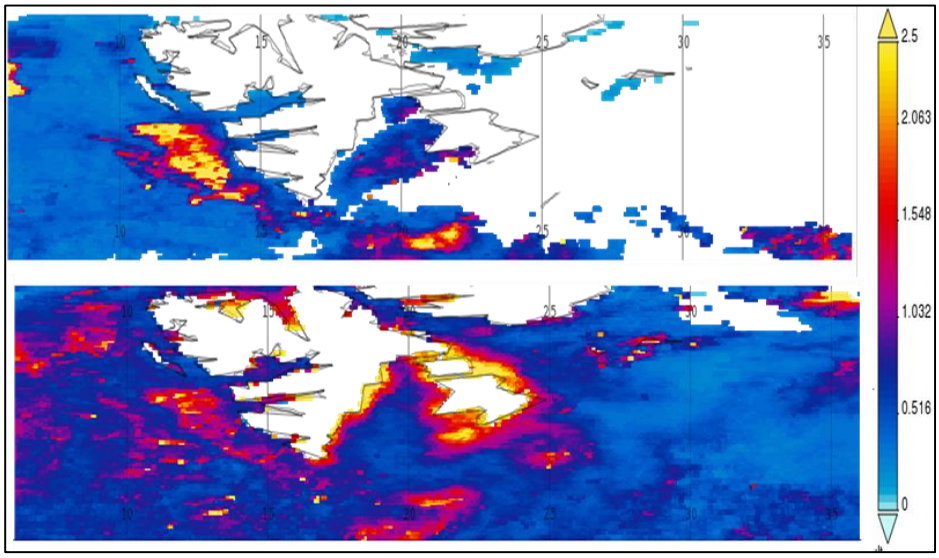

Figure S3. Satellite images of surface Chl*a* concentration (mg m^{-3}) averages around Svalbard (6-36 E, 75-80 N) in 9 May -2 June (top) and 18 June – 4 July (down). Level -3 MODIS-Aqua data retrieved from https://giovanni.gsfc.nasa.gov/giovanni/ with using Giovanni v 4.28 (Acker and Leptoukh, 2007).

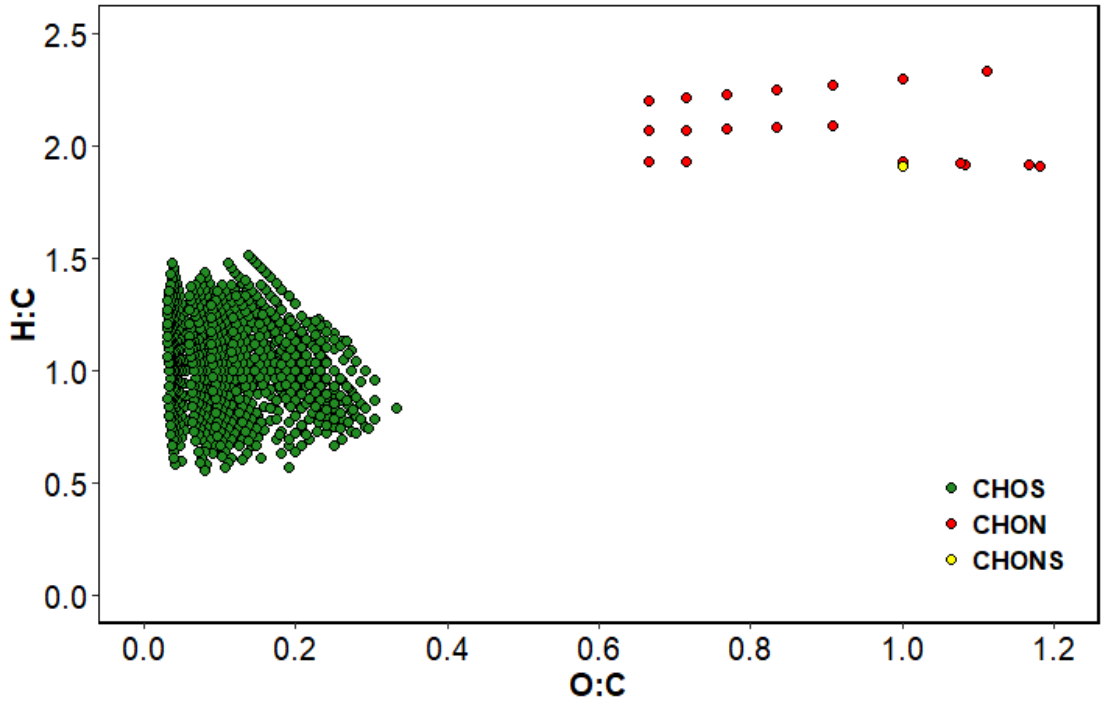

Figure S4: Unique formulas that are detected in the deepest sample at YP station indicating a link to a black sulphur presence.

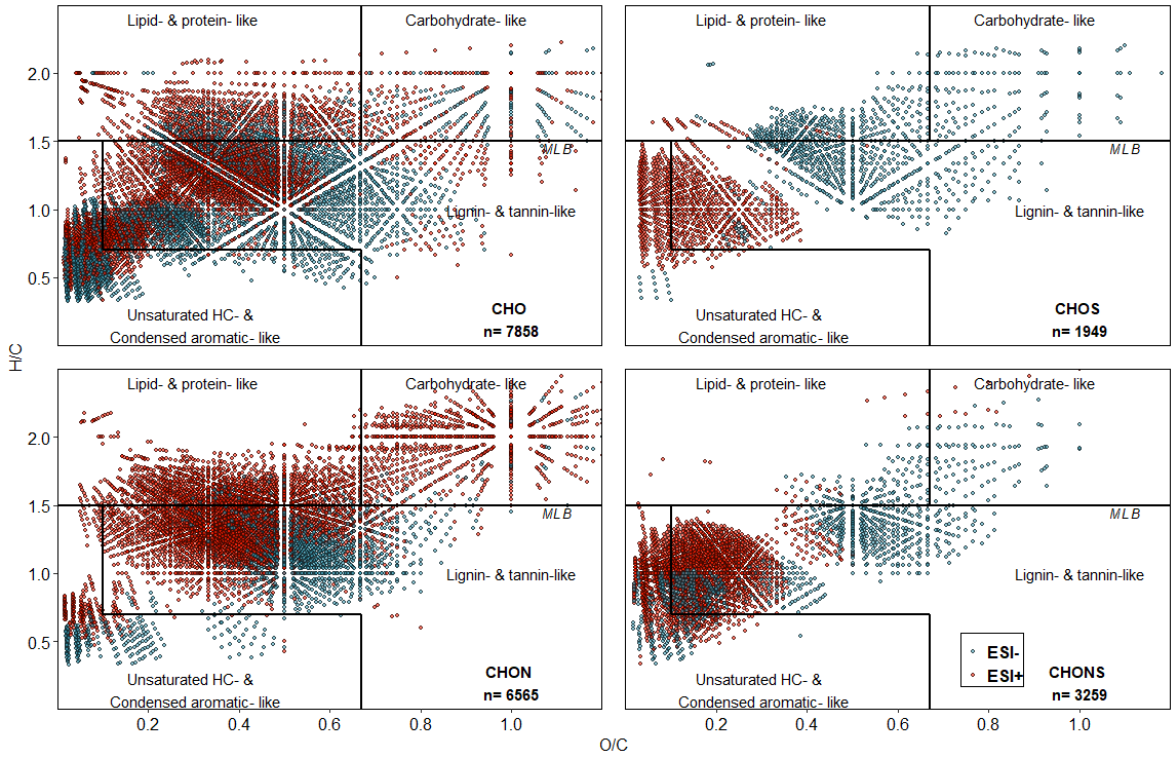

Figure S5: van Krevelen diagram for 19,641 unique formulas detected in positive (red) and negative (blue) ESI modes. Each point in the diagrams represents a single formula assigned from one resolved mass spectral peak. Each diagram represents one of the heteroatomic classes: CHO, CHON, CHOS and CHONS and the number of formulas for each heteroatomic class are given in the right corners. Dashed lines separate molecular classes and molecular lability boundary (MLB; D'Andrilli et al., 2015).

2 References

Acker, J. G., and Leptoukh, G. (2007). Online analysis enhances use of NASA Earth science data. *Eos, Transactions American Geophysical Union* 88, 14–17. doi:10.1029/2007EO020003.

D'Andrilli, J., Cooper, W. T., Foreman, C. M., and Marshall, A. G. (2015). An ultrahigh-resolution mass spectrometry index to estimate natural organic matter lability: FTICRMS organic matter molecular lability index. *Rapid Communications in Mass Spectrometry* 29, 2385–2401. doi:10.1002/rcm.7400.

Hockaday, W. C., Purcell, J. M., Marshall, A. G., Baldock, J. A., and Hatcher, P. G. (2009). Electrospray and photoionization mass spectrometry for the characterization of organic matter in natural waters: a qualitative assessment. *Limnology and Oceanography: Methods* 7, 81–95.

Hodgkins, S. B., Tfaily, M. M., Podgorski, D. C., McCalley, C. K., Saleska, S. R., Crill, P. M., et al. (2016). Elemental composition and optical properties reveal changes in dissolved organic matter along a permafrost thaw chronosequence in a subarctic peatland. *Geochimica et Cosmochimica Acta* 187, 123–140. doi:10.1016/j.gca.2016.05.015.

Chapter 3

Paper II

Composition of dissolved organic matter in the ice-covered water column above hydrothermal vents at the Aurora Seamount, Gakkel Ridge, Arctic Ocean

Biogeosciences, 19, 2101–2120, 2022
https://doi.org/10.5194/bg-19-2101-2022

Biogeosciences Open Access EGU

Compositions of dissolved organic matter in the ice-covered waters above the Aurora hydrothermal vent system, Gakkel Ridge, Arctic Ocean

Muhammed Fatih Sert[1], Helge Niemann[1,2,3], Eoghan P. Reeves[4], Mats A. Granskog[5], Kevin P. Hand[6], Timo Kekäläinen[7], Janne Jänis[7], Pamela E. Rossel[8], Bénédicte Ferré[1], Anna Silyakova[1], and Friederike Gründger[9]

[1]Centre for Arctic Gas Hydrate, Environment and Climate (CAGE), Department of Geosciences, UiT The Arctic University of Norway, Tromsø, Norway
[2]Department of Marine Microbiology and Biogeochemistry, NIOZ Royal Institute for Sea Research, Texel, the Netherlands
[3]Department of Earth Sciences, Faculty of Geosciences, Utrecht University, Utrecht, the Netherlands
[4]Department of Earth Science and Centre for Deep Sea Research, University of Bergen, Bergen, Norway
[5]Norwegian Polar Institute, Fram Centre, Tromsø, Norway
[6]Jet Propulsion Laboratory, California Institute of Technology, Pasadena, USA
[7]Department of Chemistry, University of Eastern Finland, Joensuu, Finland
[8]Interface Geochemistry, GFZ German Research Centre for Geosciences, Potsdam, Germany
[9]Arctic Research Centre, Department of Biology, Aarhus University, Aarhus, Denmark

Correspondence: Muhammed Fatih Sert (muhammed.f.sert@uit.no)

Received: 22 December 2021 – Discussion started: 3 January 2022
Revised: 7 March 2022 – Accepted: 13 March 2022 – Published: 20 April 2022

Abstract. Hydrothermal vents modify and displace subsurface dissolved organic matter (DOM) into the ocean. Once in the ocean, this DOM is transported together with elements, particles, dissolved gases and biomass along with the neutrally buoyant plume layer. Considering the number and extent of actively venting hydrothermal sites in the oceans, their contribution to the oceanic DOM pool may be substantial. Here, we investigate the dynamics of DOM in relation to hydrothermal venting and related processes at the as yet unexplored Aurora hydrothermal vent field within the ultraslow-spreading Gakkel Ridge in the Arctic Ocean at 82.9° N. We examined the vertical distribution of DOM composition from sea ice to deep waters at six hydrocast stations distal to the active vent and its neutrally buoyant plume layer. In comparison to background seawater, we found that the DOM in waters directly affected by the hydrothermal plume was molecularly less diverse and 5 %–10 % lower in number of molecular formulas associated with the molecular categories related to lipid and protein-like compounds. On the other hand, samples that were not directly affected by the plume were chemically more diverse and had a higher percentage of chemical formulas associated with the carbohydrate-like category. Our results suggest that hydrothermal processes at Aurora may influence the DOM distribution in the bathypelagic ocean by spreading more thermally and/or chemically induced compositions, while DOM compositions in epipelagic and mesopelagic layers are mainly governed by the microbial carbon pump dynamics and surface-ocean–sea-ice interactions.

1 Introduction

Dissolved organic matter (DOM) in the vicinity of high-temperature hydrothermal vents shows discrepancies in concentration compared to ocean background concentrations, mainly due to thermal decomposition of DOM during hydrothermal circulation (Hawkes et al., 2015; Lang et al., 2006). During the formation of hot hydrothermal fluids in convective circulation systems, cold deep ocean water

percolates through permeable pathways (faults/fissures) in the crust and is progressively heated and modified during high-temperature alteration of igneous (e.g., mafic, ultramafic) rocks (German and Seyfried, 2014; Simoneit et al., 2004). Continuous exposure to extremes of temperature (up to 400 °C) and low pH either completely degrade DOM to volatile species (e.g., CO_2, methane) (Lang et al., 2006) or alters originally stable, high-molecular-weight, refractory DOM to highly aromatic, unsaturated, oxygen-poor, petroleum-like compositions in the hydrothermal vent fluids (Hawkes et al., 2015, 2016; Rossel et al., 2015, 2017). In relatively low temperature hydrothermal systems (< 150 °C), DOM is not degraded by cracking (Lang et al., 2006), and production of DOM may be more prevalent (Hawkes et al., 2015). DOM may therefore be a significant source of mixed forms of complex reduced carbon in the vent fluids, which can include dissolved free amino acids (Fuchida et al., 2014; Haberstroh and Karl, 1989; Horiuchi et al., 2004), lipids (McCollom et al., 1999, 2015) and bio-labile organic carbon (Hansen et al., 2019; Longnecker et al., 2018; Rossel et al., 2015). Considering that the deep-ocean DOM is refractory (e.g., Dittmar and Stubbins, 2014; Hansell, 2013) or primarily inaccessible for organisms (e.g., Arrieta et al., 2015), specialized microbial communities may therefore utilize hydrothermally modified DOM as a carbon source and support hydrothermal fauna in the vicinity of hydrothermal vents (Bart et al., 2020; Folkers and Rombouts, 2020; Hestetun et al., 2016; Yahel et al., 2003).

The chemical composition and temperature of venting fluids emanating at the seafloor and contributing to hydrothermal plume formation are mainly controlled by the geological setting and physicochemical constraints including phase separation, water–rock interaction (mineral precipitation/dissolution) and biological processes (German and Seyfried, 2014; Nakamura and Takai, 2014). Hydrothermal fluids emitted from the vents are diluted with ambient water by factors of 10^4–10^5 and form a hydrothermal plume that rises hundreds of meters until reaching neutral buoyancy in the water column (Baker et al., 1995). Previous field observations, as well as models, show that rising, neutrally buoyant plumes can disperse horizontally at isopycnal surfaces for tens to even thousands of kilometers (Baker et al., 1995; Lupton and Craig, 1981; Rudnicki and Elderfield, 1993; Speer and Rona, 1989; Tao et al., 2013). Thereby, they form environmental gradients (also called ecotones) conducting particles, nutrients, organic matter, trace elements and biomass (Levin et al., 2016; Ramirez-Llodra et al., 2010).

These neutrally buoyant hydrothermal plumes in deep oceans are areas of active chemical cycling that sustain life in the hyper-oligotrophic bathypelagic zones. Plumes fuel chemosynthetic and heterotrophic prokaryotes, archaea, viruses and zooplankton that grow in this ecosystem in a spatiotemporal succession (Burd and Thomson, 1994; Dick, 2019; Levin et al., 2016). Morphological evidence suggests that heterotrophic deep-sea communities take over chemosynthetic vent-derived communities along the path of the dispersing plume layer. The heterotrophs use DOM in the plume in which subsequent lysis of their cells further amplifies heterotrophic bacteria and DOM release (Ortmann and Suttle, 2005). Controlled incubation experiments showed that the thermal degradation of deep-sea recalcitrant DOM elevates the microbially accessible composition and stimulates the growth of prokaryotic communities (Hansen et al., 2019).

More than 300 high-temperature venting sites have been identified at mid-ocean ridges (Hannington et al., 2011; Nakamura and Takai, 2014), and around 800 are estimated to exist, roughly half of which are expected to be found in slow/ultraslow-spreading mid-ocean ridges (Beaulieu et al., 2015). Because of the limited number of expeditions in the ice-covered Arctic Ocean, surveys of hydrothermal vents at very high latitudes have been extremely rare. However, considering the amount of fluid venting at hydrothermal vents and the far-reaching area of impact through plume dispersion, their influence on marine DOM may be substantial in the oligotrophic Arctic Ocean. There, hydrothermally derived DOM could potentially influence mesopelagic and epipelagic layers, as well as surface-ocean–sea-ice interactions.

In this paper, we investigate the influence of hydrothermal activity on the DOM composition in the Arctic Ocean water column at the Aurora hydrothermal vent system. We suggest that the hydrothermal plume distributes thermally altered DOM to greater areas, where its composition will be altered through admixture with background seawater and through microbial processes. We characterize the water column DOM composition from the seafloor to the sea ice to assess the vertical extent of hydrothermal intrusion and its confluence with hydrophysical and chemical parameters.

2 Methods

2.1 Study area

The Aurora seamount (82.897 N, 6.255 W) is located at the southern tip of the ultraslow-spreading ($< 12.0\,\mathrm{mm\,yr^{-1}}$) Gakkel Ridge that extends for 1800 km across the Eurasian Basin in the Arctic Ocean (DeMets et al., 2010). The seamount has a height of 300 m above the seafloor (m a.s.f.) and is elongated in a southeast–northwest direction (Fig. 1). The water column at the mount's summit has a depth of 3800 m, and it reaches 4500 m at the southern side of the ridge flank. The sea surface in this region is capped by a perennial ice cover. The Aurora seamount was explored by two research icebreakers in 2001 (expedition AMORE); evidence for high levels of hydrothermal activity was observed (fresh sulfide chimney structures, shimmering water, abundant biological activity); and anomalies in temperature, dissolved manganese and light scattering were detected (Ed-

monds et al., 2003; Michael et al., 2003). An active "black smoker" hydrothermal vent at the Aurora site (named after Aurora seamount) was later located ∼ 100 m southwest of the summit in 2014, and high methane concentrations and temperature anomalies were documented along with a plume layer extending towards northwest of vent field (Boetius et al., 2014, 2015; German and Boetius, 2017). As a continuation of the investigation in the area, and to further understand the role of the Gakkel Ridge in the scope of the global biogeography of chemosynthetic ecosystems (Vanreusel et al., 2009), the first HACON (Hot vents in an ice-covered ocean, HACON19) expedition attempted to reach the site again in 2019 (Bünz et al., 2020). During the cruise, both active and inactive hydrothermal vents at the vent site were visually observed in much greater detail, using a towed camera system (Ocean Floor Observation and Bathymetry System, OFOBS; Purser et al., 2019). The active vent area is evidently characterized by several vigorously venting black smokers, sulfide mounds, bacterial mats, thinly sedimented outcrops, and benthic communities typical of hydrothermal vent ecosystems (Bünz et al., 2020).

2.2 Water sampling and analyses

2.2.1 Sampling/sub-sampling

We collected water samples from six stations near the Aurora hydrothermal vent field during the HACON19 research cruise on board R/V *Kronprins Haakon* (September–October 2019) (Fig. 1). Sea ice and the upper 1000 m of the water column were sampled at the upper layer (UL) station southwest of the vents. Plume (PL) and non-plume (NP1, NP2, NP3) stations were designated to observe the spreading of the hydrothermal plume and were measured from 2000 m depth down to 10 m a.s.f. (< 4500 m water depth). A background station (BG) was sampled further away from the seamount (Fig. 1e). At this station, measurements were done from 2000–4500 m water depth similarly to the PL and NP stations (Table 1).

Seawater samples were collected at selected sampling depths using Niskin bottles attached to a rosette (Table 1). Sea ice was sampled at the surface of UL, thawed in a high-density polyethylene (HDPE) container at room temperature and further treated similarly to the seawater samples collected with the rosette sampler.

Duplicate samples for methane concentration and stable C isotope ratios (δ^{13}C-CH_4) were collected immediately after the recovery of the rosette sampler into 120 mL airtight syringes and pre-evacuated rubber-stoppered serum vials, respectively. Care was taken to purge sampling lines of any bubbles, and methane samples were typically the first collected upon opening of Niskin bottles. Methane concentrations from two independent samples (i.e., Niskin bottles closed at the same depth) typically agreed to within ±10 %–20 % (two standard deviations; note that we could take duplicate samples only occasionally). For DOM and nutrient characterization, seawater was first transferred into acid-washed (2 % HCl) glass bottles (2 × 1135 mL) and filtered through pre-combusted (400 °C, 5 h) GF/F filters (Whatman) within 2 h after collection using a low-pressure vacuum. Nitrate, phosphate, silicate, ammonium, total nitrogen, total phosphorus, and dissolved organic carbon (DOC) samples were collected in 60 mL HDPE bottles from the filtrate and stored at −20 °C. Samples for dissolved inorganic carbon (DIC) and δ^{13}C-DIC measurement were taken and poisoned with 10 µL $HgCl_2$ and stored at 4 °C. Seawater aliquots for δ^{18}O-H_2O analysis were sampled in 20 mL clear glass vials and stored at 4 °C. For solid phase extraction of DOM, 1 L of filtrate was acidified to pH 2 with HCl (37 % v/v, Merck) and extracted with preconditioned (with 6 mL methanol + 12 mL pH 2 water) 500 mg PPL cartridges (Bond Elut, Agilent Technologies) as described previously (Dittmar et al., 2008). Loaded cartridges were dried under air vacuum for ∼ 30 min, and any organics retained in the cartridges were then eluted into pre-combusted, amber glass vials with 2 mL methanol and stored at −20 °C until analysis in Fourier-transform ion cyclotron resonance mass spectrometer (FT-ICR MS).

2.2.2 CTD and LADCP measurements

Sensor-based profiling of the water column was conducted with a Sea-Bird SBE 911 plus CTD (conductivity–temperature–depth) profiler (accuracies of 0.3 db, 0.001 °C, 0.002 for salinity (practical salinity scale, unitless)), an SBE 43 coupled with a dissolved oxygen sensor (calibrated by Winkler (1888) titration), a Wet Labs ECO chlorophyll fluorometer (excitation/emission: 470/695 nm; sensitivity and limit of detection 0.01 µg L^{-1}) and a Wet Labs C-Star beam transmissometer. As a proxy for turbidity, the beam attenuation coefficient (c, m^{-1}) at 650 nm was determined by post calibration (see Fig. S1 in the Supplement). The sampling rosette was equipped with a HiPAP (High Precision Acoustic Positioning, Kongsberg Maritime) acoustic beacon to obtain real-time positioning at depth. Two Lowered Acoustic Doppler Current Profilers (LADCP) were mounted on the CTD rosette in downward- and upward-looking configurations. The CTD rosette was stopped at predefined depths for 10 min for LADCP measurements, and the raw data were corrected against the continuous drift of the vessel based on HiPAP data (see Fig. S2 in the Supplement).

2.2.3 Analysis of seawater constituents and dissolved gases

Nitrate, nitrite, silicate, phosphate, ammonium, total phosphorus, and total nitrogen concentrations were measured with a segmented flow nutrient analyzer (Alpkem Flow Solution IV, OI Analytical), based on colorimetry, with associated detection limits and precision for nitrate (0.5 ± 0.1 µM), nitrite (0.05 ± 0.01 µM), phosphate (0.06 ± 0.01 µM), silicate

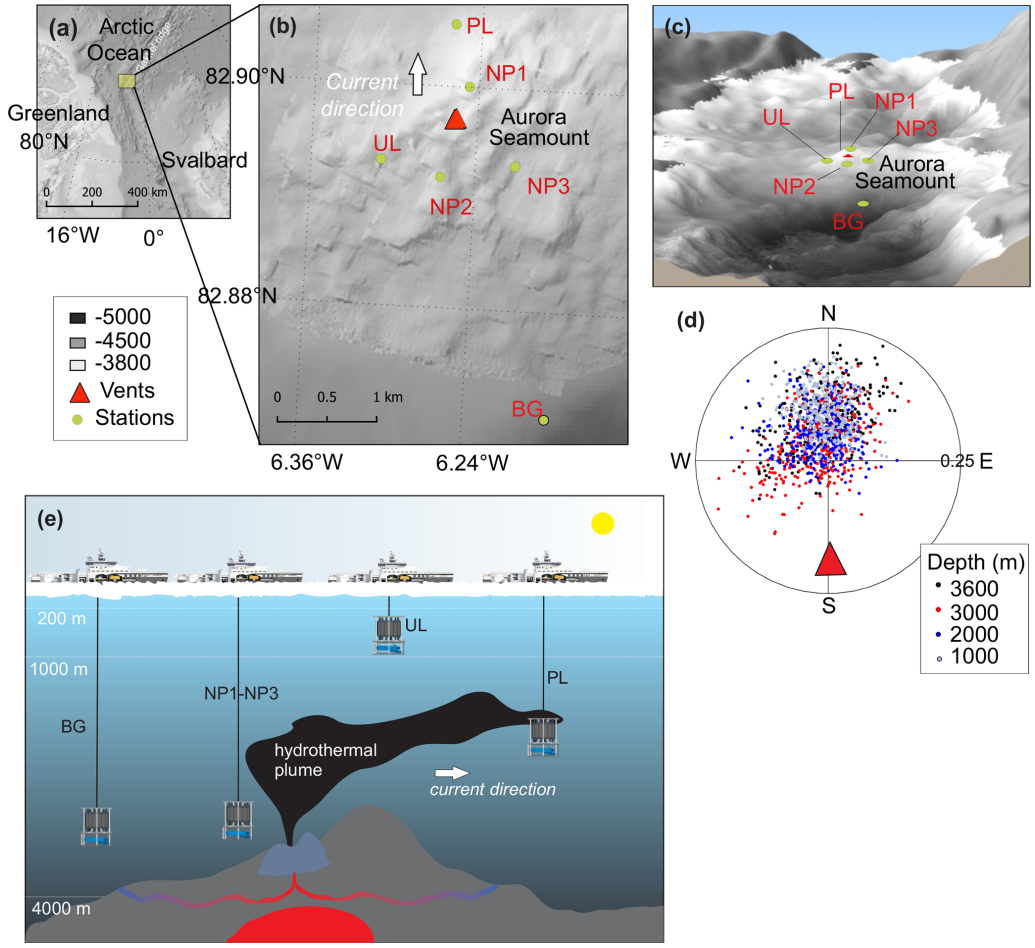

Figure 1. **(a)** Study site in the Arctic Ocean. **(b, c)** Close-up of the study site showing the locations of the background station (BG), plume layer station (PL), non-plume stations (NP1 to NP3) and upper layer station (UL) on a bathymetric map (IBCAO; Jakobsson et al., 2008). **(d)** Direction and the current velocity obtained from the LADCP (lowered acoustic Doppler current profiler) at the PL station where each point represents an average of a depth bin calculated from east and north velocity components. **(e)** The graphical representation of station locations with respect to the dispersion of the hydrothermal plume, current direction and the oceanic layers.

Table 1. Sampling stations, positions, water depth and measured parameters at corresponding sampling depths for methane, δ^{13}C-CH_4, dissolved organic matter (DOM) composition and nutrients (see text for details).

Category	Station name	Latitude N	Longitude W	Water depth (m)	Sampling depths (m) and measured parameters
Background station	BG	82.916	6.255	4407	$2000^{1,2,3}$, 2750^{1}, $3250^{1,2,3}$, $3750^{1,3}$, 4200^{1}, 4300^{1}, $4400^{1,2,3}$
Upper layer station	UL	82.891	6.324	3982	Sea ice^{3,4}, $5^{3,4}$, $25^{3,4}$, $40^{3,4}$, $100^{3,4}$, $250^{3,4}$, $500^{3,4}$, $1000^{3,4}$
Plume layer station	PL	82.899	6.330	4026	$2500^{1,3,4}$, $3000^{1,2,3}$, $3250^{1,2}$, $3300^{1,2}$, $3350^{1,2}$, $3400^{1,2,3}$, $3450^{1,2}$, $3500^{1,2,3}$, $3550^{1,2}$, 3600^{1}, $4015^{1,3,4}$
Non-plume stations	NP1	82.892	6.243	3870	$2000^{1,4}$, 3000^{1}, $3075^{1,2}$, $3150^{1,2,4}$, $3225^{1,2}$, $3300^{1,2}$, $3865^{1,4}$
	NP2	82.894	6.265	4026	$2850^{1,2}$, $2950^{1,2}$, $3090^{1,2}$, $3240^{1,2,3}$, $3530^{1,2,3}$, $3970^{1,2}$
	NP3	82.900	6.247	4075	2000^{1}, 2800^{1}, 3000^{1}, 3150^{1}, 3300^{1}, 4070^{1}

[1] Methane concentration. [2] δ^{13}C-CH_4. [3] DOM composition. [4] Nutrients.

($0.4 \pm 0.1\,\mu M$), and ammonium ($0.01 \pm 0.01\,\mu M$). Dissolved organic nitrogen (DON) was determined from total dissolved nitrogen by subtracting the concentrations of dissolved inorganic nitrogen (nitrate + nitrite + ammonium). Similarly, dissolved organic phosphorus (DOP) was calculated from total dissolved phosphorus by subtracting phosphate concentration. Dissolved organic carbon (DOC) concentrations were measured with a TOC analyzer (MQ-1001) utilizing a high-temperature combustion technique (Qian and Mopper, 1996). Deep-ocean DOC reference samples (Hansell Laboratory, University of Miami) were used to monitor precision and accuracy. DIC concentrations, δ^{13}C-DIC and δ^{18}O-H_2O were measured on a Thermo Scientific MAT253 isotope ratio mass spectrometry (IRMS) and presented in the delta notation as δ^{13}C relative to Vienna Pee Dee Belemnite (VPDB) and δ^{18}O relative to Vienna Standard Mean Ocean Water (VSMOW). The IRMS was calibrated with international standards VSMOW2, GISP (Greenland ice sheet precipitation), SLAP2 (Standard Light Antarctic Precipitation 2), and VPDB, and the uncertainty of single measurements is $\leq 0.01\,‰$. Dissolved methane concentrations were measured on board following headspace extraction with nitrogen using a gas chromatograph (GC) equipped with a flame ionization detector following the procedure used in German et al. (2010). For δ^{13}C-CH_4 measurements, samples were quantified on board by a Picarro cavity ring-down spectrometer instrument (as per McDermott et al., 2017).

2.3 Fourier-transform ion cyclotron resonance mass spectrometry analyses and molecular formula assignments

FT-ICR MS analyses to evaluate the composition of DOM samples were carried out with a 12T Bruker solariX FT-ICR mass spectrometer (Bruker Daltonics, Bremen, Germany), equipped with a dynamically harmonized ICR cell (ParaCell) and an Apollo-II electrospray ionization (ESI) source, operated in both positive-ion and negative-ion modes. For the MS analyses, 100 µL aliquots of DOM samples were diluted 1 : 10 (v/v) with methanol (HPLC grade). ESI was selected as the ionization technique due to its ability to ionize polar, oxygen-containing compounds present in the DOM samples (Mopper et al., 2007). The samples were directly infused into the ion source by a syringe pump, operating at a flow rate $2\,\mu L\,min^{-1}$. Dry nitrogen was used as the drying and nebulizing gas. The ESI-generated ions were accumulated in the hexapole ion trap and transferred into the ICR cell for trapping, excitation and detection. For each spectrum, 100 scans were co-added over a mass / charge ratio (m/z) range of 150–2000. The Bruker Compass ftmsControl 2.1 software package was used for instrument control and data acquisition.

Initial spectral post-processing was done with the Bruker DataAnalysis 5.0 SR1 software, including an internal mass re-calibration with an in-house calibration list for the DOM samples. The data were then transferred to the PetroOrg IS-18.0.3 software (Omics LLC, Tallahassee, FL, USA) for molecular formula assignments. Only mass peaks with a signal-to-noise ratio (S/N) $\geq$ 5 were considered. In the assignments of the molecular formulas, monoisotopic compositions were limited to $^{12}C_{1-100}{}^{1}H_{1-200}{}^{14}N_{0-4}{}^{16}O_{0-30}{}^{32}S_{0-2}$ with a double bond equivalent (DBE) of 0–50 and a mass error of ≤ 1.0 ppm. Relative intensities were calculated by normalization with the most abundant ion in each mass spectrum (Kujawinski et al., 2009). Assigned molecular formulas were then generated for each sample at positive- and negative-ion modes and combined to obtain a single molecular formula list. In case of duplicate formula, relative intensity obtained from the negative ESI was considered. The combination of negative and positive mode ESI provides a better representation of DOM composition for the carboxylic and acidic compounds (negative ESI) and hydrogen-saturated aliphatic compounds (positive ESI) (Ohno et al., 2016; Sert et al., 2020).

From the combined formula lists, chemical characterization of DOM compositions was conducted to obtain percentages of (i) three categories of heterogeneous atomic content as CHO, CHON, and CHOS and (ii) H : C and O : C atomic ratios and ranges on van Krevelen diagrams (Kim et al., 2003). Considering the H : C and O : C atomic ratios of major biomolecules, ranges of H : C and O : C were generically associated with four biochemical compound categories, disregarding structural differences and atomic compositions of individual formulas in the group. These categories are (a) lipid- and protein-like (LPD) for H : C $\geq$ 1.5, O : C $\leq$ 0.67; (b) carbohydrates and amino-sugar-like (CAR) for H : C $\geq$ 1.5, O : C $>$ 0.67; (c) unsaturated hydrocarbons and condensed aromatics (UHC) for H : C $<$ 1.5, O : C $<$ 0.1 and H : C $<$ 0.7, O : C $<$ 0.67; and (d) lignin- and tannin-like (LGN) for 1.5 $<$ H : C $<$ 0.7, O : C $>$ 0.67. Boundaries were modified from Hockaday et al. (2009) and Hodgkins et al. (2016) as explained previously (Sert et al., 2020). For calculating percentages, the number of formulas that associated with a given category was divided by the total number of formulas in the sample and multiplied by 100. For example, the sum of the percentages of LPD, CAR, LGN and UHC is equal to 100 %, and, similarly, the sum of the percentages of CHO, CHON and CHOS is equal to 100 % for each sample.

2.4 Statistical analyses of DOM samples

Statistical analyses were performed in R (R Core Team, 2018). Diversity indices for DOM samples were calculated by the "diversity" function analogous to biodiversity in ecology using the Shannon–Weaver formulation (Oksanen, 2020) as explained previously (Sert et al., 2020). A Bray–Curtis dissimilarity (distance) matrix (Bray and Curtis, 1957) was constructed by using relative intensities of formulas from 11 DOM samples that were collected $>$ 2000 m in stations BG, PL and NP2. Hierarchical cluster analysis was applied for DOM compositions using a Ward clustering algorithm

("hclust" function in vegan) on a Bray–Curtis dissimilarity matrix. A heat map was constructed to visualize the sample clusters and the relative dissimilarities. Principal coordinate analysis (PCoA) was applied by using "pcoa" function in the R package APE (Paradis and Schliep, 2019) on the Bray–Curtis dissimilarity matrix. The ordination plot was constructed from the first two main axes that represent the highest variation between samples. Percentages of explained variances on two main axes were calculated by dividing the two highest eigenvalues to the sum of all eigenvalues.

3 Results and discussion

3.1 Water column physical and chemical properties

Water circulation in the Eurasian part of the Arctic Ocean is mainly characterized by Atlantic inflow and Arctic outflow through the Fram Strait, with a monthly mean volume of 9.5 and 11 Sv, respectively (Fahrbach et al., 2001). We categorize the water column in three water layers as epipelagic (0–200 m), mesopelagic (200–1000 m) and bathypelagic (1000–4000 m) considering the depth and the four water masses that are defined by the density layers of $\sigma_t \leq 27.7$ for Polar Surface Water (PSW), $27.7 < \sigma_t \leq 27.97$ for Arctic Atlantic Water (AAW), $\sigma_t > 27.97$ and $\sigma_{0.5} \leq 30.444$ for Arctic Intermediate Water (AIW), and $\sigma_{0.5} > 30.444$ for Deep Water (DW) (Marnela et al., 2008; Rudels et al., 2005). The epipelagic layer contains PSW until 165 m depth with temperatures ranging between −1.7 and 0.4 °C and salinity from 31.6 to 34.65 (Fig. 2a–e). AAW exists beneath PSW from the bottom of the epipelagic layer down to 450 m and includes a temperature maximum of 1.27 °C at 350 m. From 450 to 1400 m, the temperature decreases from 0.9 to −0.5 °C in a steep thermocline, forming AIW. AAW and AIW together form the East Greenland Current that carries Arctic waters southwest along the Greenland coasts and gradually mixes with the convected surface waters (Rudels et al., 1995). Below the AIW layer, water temperature decreases to −0.73 °C at around 2500 m, where DW fills the Eurasian Basin. Here, the density is largely controlled by salinity rather than temperature, and the shape of the density profile is almost identical to the salinity profile (Fig. 2b and c). Despite the dominant sea ice cover at our study area, preventing solar radiation from reaching the water column, a chlorophyll *a* (Chl *a*) fluorescence signal was detected down to 200 m depth (Fig. 2d). At all stations, the first 40 m below the sea surface showed a Chl *a* maximum with an average concentration of 0.17 $\mu g L^{-1}$, followed by a decrease to 0.10 $\mu g L^{-1}$ at 50 m. From this depth, concentrations gradually decreased further until the detection limit (0.01 $\mu g L^{-}$) was reached at the bottom of the epipelagic layer (Fig. 2d).

Nutrient profiles, nutrient ratios, δ^{13}C-DIC and δ^{18}O all display a typical deep-ocean surface-to-bottom gradient and were identical at all stations (Fig. 3). Nitrate, phosphate, and silicate concentrations were lowest at the surface (5 m) with 1, 0.44, and 6.1 µM, respectively, and increased gradually to average bathypelagic concentrations of 14.8, 0.96 and 12.0 µM at 2000 m (Fig. 3a–c). On the contrary, dissolved organic nutrients were highest in the epipelagic layer with the maximum concentrations of 92 µM for DOC at 100 m and 6.2 µM for DON at the surface (Fig. 3e and f). Similarly, ammonium and DOP were detectable only in the epipelagic layer with average concentrations of 0.2 and 0.1 µM, respectively (see Fig. 3d for ammonium; DOP is not plotted). Nitrate, phosphate, and silicate concentrations in sea ice were below the detection limit; however, detectable concentrations of ammonium (0.6 µM), DOC (4.0 µM) and DON (0.6 µM) were measured in sea ice.

δ^{18}O values were obtained in three different concentration ranges that changed with depth. Sea ice had a δ^{18}O value of −4.53 ‰. At the top 100 m, δ^{18}O had an average value of −2.24 ‰. From 250 m to bottom δ^{18}O was uniform with an average of 0.36 ‰ (Fig. 3h). This corresponds to water mass properties with contributions from sea ice melt waters and Arctic river runoff with negative δ^{18}O values in the upper 100 m within PSW, compared to highly uniform deep-water ratios. Our δ^{18}O measurements are comparable to previous measurements in the area that reported ∼ 0.3 ‰ in deep water and −2.6 ‰ to −1.6 ‰ in the upper 100 m (Bauch et al., 1995; Östlund and Hut, 1984).

A δ^{13}C-DIC value of −13 ‰ was measured in sea ice. δ^{13}C-DIC values decreased from 0.86 ‰ at the surface to 0.44 ‰ at 250 m and gradually increased to 0.62 ‰ at 1000 m. δ^{13}C-DIC changed in a narrow range from 2000 m to bottom with an average composition of 1.03 ‰ (Fig. 3g). Sea ice coverage in the Arctic Ocean has been decreasing by ∼ 9 % per decade, leading to a longer growing period for phytoplankton and associated increase in net primary production (Arrigo and van Dijken, 2015, and references therein). Taken together with the imprint of the anthropogenic CO_2 (with a δ^{13}C value of ca. −8.5 ‰), δ^{13}C-DIC values obtained at the sea ice and the upper layer of the water column are linked to contributions of several factors, including biological productivity, air–sea gas exchange and sea ice or brine formation, which admixes DIC with a lighter δ^{13}C signature compared to that of deep waters. For example, deep-water δ^{13}C-DIC values of 1.0 ‰ ± 0.2 ‰ were found in the Canada Amundsen and Nansen basins (Bauch et al., 2015; de la Vega et al., 2019). At the time of sampling, the net growth of phytoplankton seems to decelerate at the top 50 m layer of the water column considering the nutrient depletion and the subsurface maxima of Chl *a* at ∼ 40 m water depth. During the Arctic summer (from March to September), this layer gets depleted in inorganic nutrients and enriched in dissolved organic matter (Thingstad et al., 1997). In the deeper layers, nitrate / phosphate and nitrate / silicate ratios are almost identical to the Redfield ratios of 16 : 1 and 1 : 1, respectively (Redfield, 1958) (Fig. 3i and j). Ratios of nitrate / phosphate (2.3 : 1–5.2 : 1) and nitrate / silicate

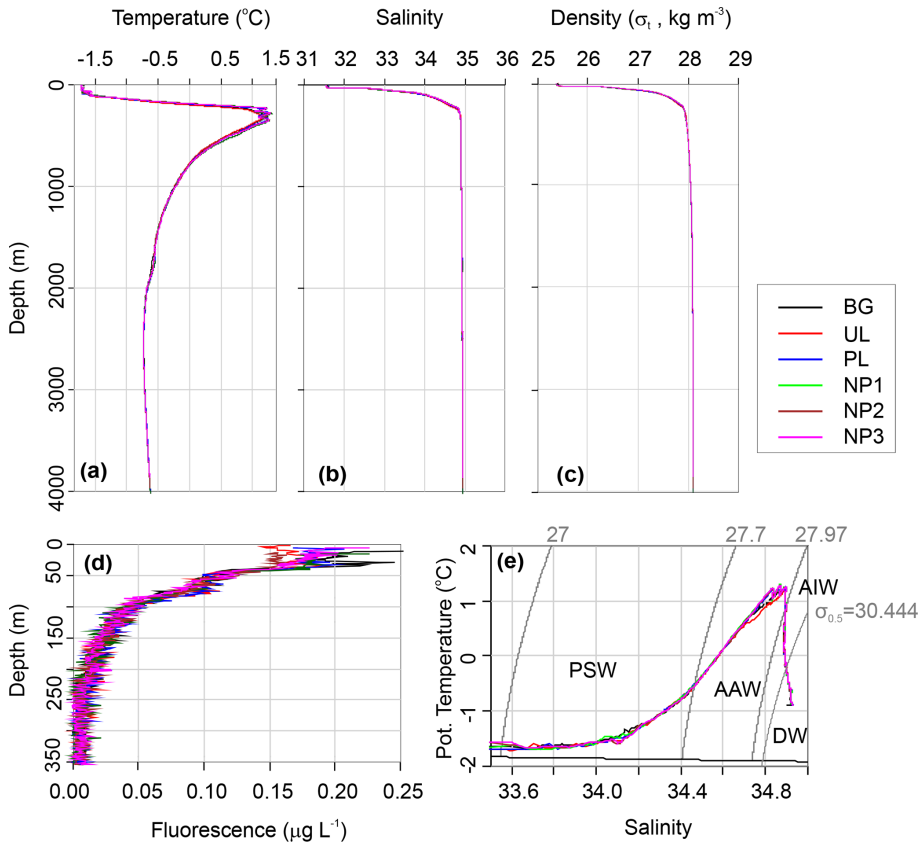

Figure 2. Depth profiles of **(a)** in situ temperature, **(b)** salinity on the practical salinity scale, **(c)** potential density, **(d)** Chl *a* fluorescence, and **(e)** potential temperature vs. salinity profile along with the characterized water masses, Polar Surface Water (PSW), Arctic Atlantic Water and Arctic Intermediate Water (AAW/AIW), Arctic Deep Water (DW) in the background (BG), upper layer (UL), plume (PL) and non-plume (NP1–NP3) stations.

(1 : 5–1 : 2.5) in the 0–100 m layer indicate that nitrate limits primary production. With the contribution of the epipelagic DON, however, surface/subsurface TDN / phosphate (16.3 : 1) and TDN / silicate (1.2 : 1) ratios became comparable with the mesopelagic / bathypelagic ratios (Fig. 3l). This indicates that DON may be used as a nitrogen source to support bacterial growth, considering that such low primary production cannot sustain the bacterial demand in relation to limited light and low water temperature (Fouilland et al., 2018). Besides nitrogen, silicate was also limiting at the surface waters when compared to phosphate (silicate / phosphate ratios of $\sim$ 13 : 1). Thus, perhaps due to diatom growth, silicate demand accompanies bacterial phosphate regeneration below the surface, lowering the silicate / phosphate ratios (7.6 : 1–9.6 : 1) compared to the deep ocean (12.4 : 1) (Fig. 3k).

3.2 Dispersion of the hydrothermal plume

Turbidity anomalies, elevated methane concentrations and varying δ^{13}C-CH$_4$ values in the vertical profiles imply that the plume rises from the $\sim$ 3900 m deep vent up to $\sim$ 3000 m in the water column and spreads laterally northward in the direction of the prevailing water current (Fig. 1d). Irrespective of the vent setting, tectonic structure, and background currents, previous studies and models imply that the fundamental physics behind the spreading of hydrothermal plumes are commonly characterized by buoyant flow dynamics that have been described in depth for atmospheric systems (Tao et al., 2013). Upon entering the water column, a multi-phase plume rises and spreads laterally and carries dissolved gases and entrained particles that alter turbidity and methane concentrations in the non-buoyant plume layer (Fig. 4). Fundamental anomalies of venting fluids such as elevated temperature or low salinity can, on the other hand, become rapidly overprinted by ambient seawater background hydrography, making potential anomalies in these parameters undetectable with our instrumentation (Fig. 2). Similarly, parameters that are not strongly influenced by the vent plume intrusion (i.e., nutrients, DOC and DON concentrations) do not indicate any anomaly in relation to plume dispersion distant from the vent due to dilution with seawater (Fig. 3). This seems contradictory to molecular changes in DOM compositions (as detailed further in Sect. 3.3.3); however, it must be stated that solid phase extractable DOM represents only a portion of bulk

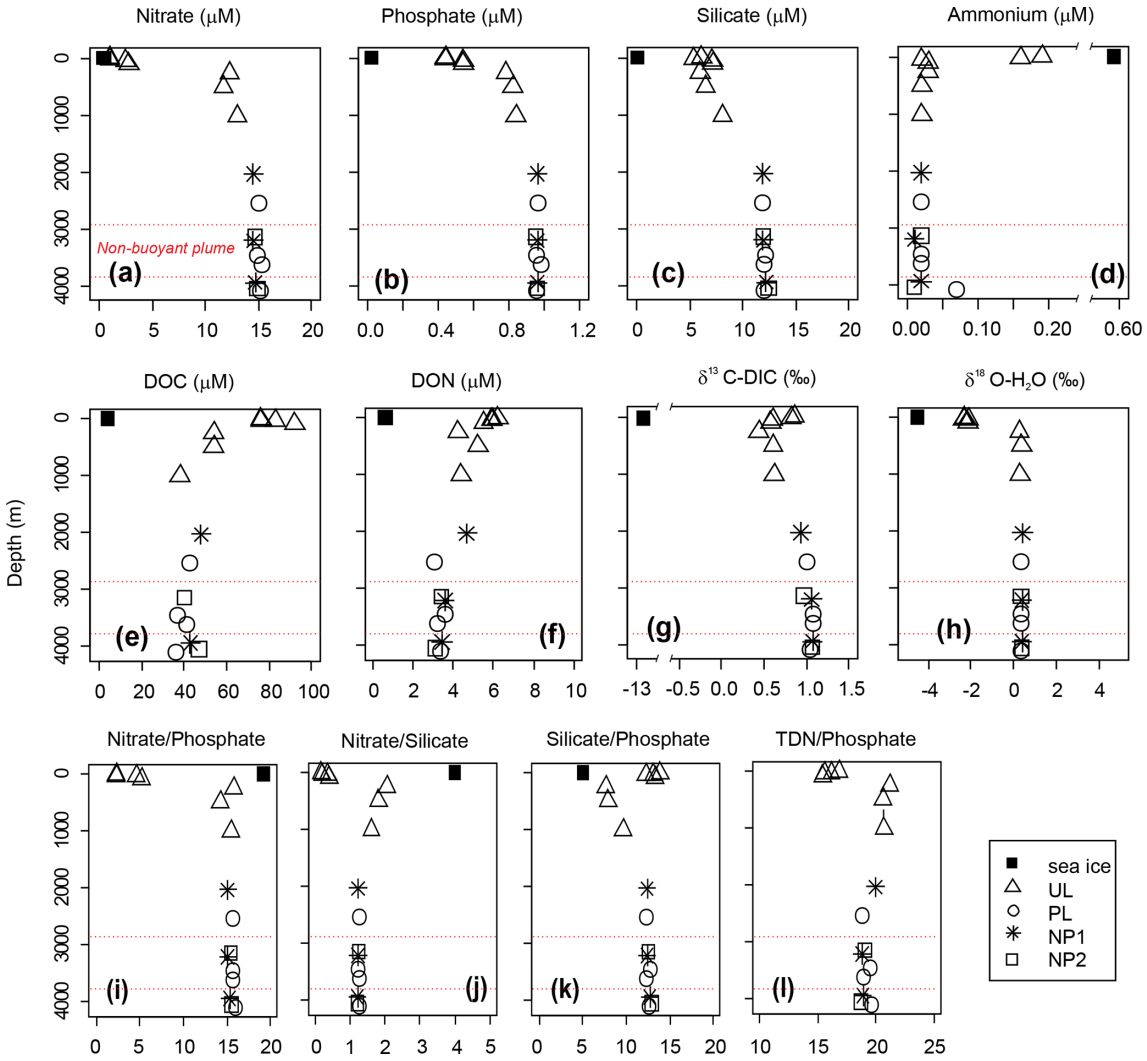

Figure 3. Depth profiles of **(a–d)** dissolved inorganic nutrients, **(e)** dissolved organic carbon (DOC), **(f)** dissolved organic nitrogen (DON), **(g)** δ^{13}C of dissolved inorganic carbon (DIC) and **(h)** δ^{18}O of water, and **(i–l)** nutrient ratios in sea ice and sampling stations background station (BG) and in sampling stations in the upper layer (UL), plume (PL) and non-plume (NP1, NP2). Axis breaks are used for a better visualization of ammonium concentration and δ^{13}C-DIC values. Total dissolved nitrogen (TDN) = nitrate + nitrite + ammonium + DON. Red dashed lines indicate the non-buoyant plume layer at PL.

DOM (43 % to 62 %; Dittmar et al., 2008), and compositional changes are not necessarily always coupled to large or substantial concentration changes. In essence, DOM molecular compositions may, more subtly, preserve some broad variations in end-member DOM traits than DOC and DON concentrations (Osterholz et al., 2016).

Continuous drifting (often $\sim$ 0.2 kn or more) of massive (kilometer scale, $\sim$ 1 m thick) ice floes prevented the vessel from keeping stable positions on station while taking samples, and, together with time constraints, related to other operational needs of the expedition, precluded us from directly sampling the buoyant stem of hydrothermal plume immediately above the active Aurora site. Due to the extreme depths (near 4 km), it furthermore typically took 3–4 h to complete a single CTD cast, so that the distance between start and end positions of a given cast were often 300–500 m apart. Nonetheless, the exact location of sampling was determined based on HiPAP data. The thickness of the non-buoyant plume also varied depending on the position of the sampling station in relation to the vent location, current direction, and bathymetric features. Based on turbidity anomalies, methane concentrations, and δ^{13}C-CH_4 contents, the plume layer was most evident at station PL, which was, counterintuitively, the station furthest away from the seamount (Fig. 4a–c), yet consistent with the prevailing current direction (see Fig. 1d). Here, methane concentrations reached a maximum of 5.1 nM at 3363 m, which is >10-fold higher compared to ambient seawater concentrations (0.3 nM) as measured at similar

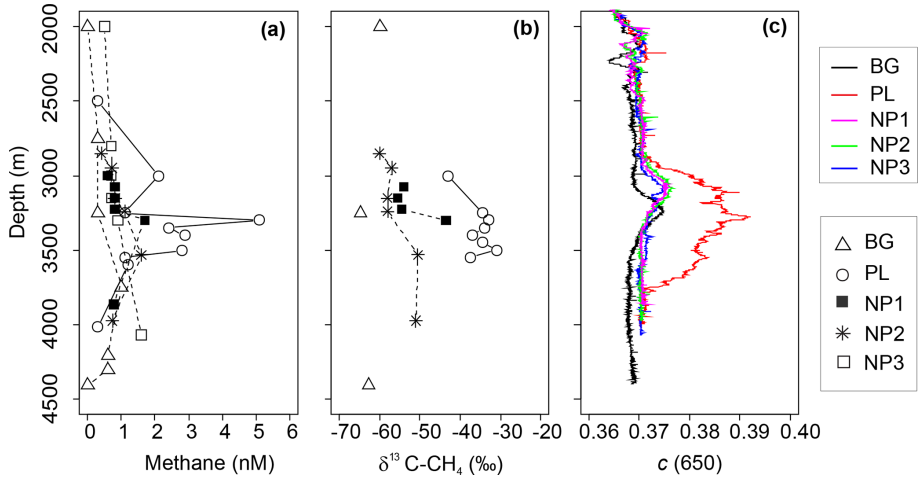

Figure 4. Depth profiles of **(a)** methane (CH_4) concentration, **(b)** δ^{13}C-CH_4 values and **(c)** beam attenuation coefficient at 650 nm **(c)** between 2000 and 4500 m depths in background (BG), upper layer (UL), plume (PL) and non-plume (NP1–NP3) stations.

depths at BG and coincides with the sharp maximum in turbidity. A small increase in turbidity was also measured at the other stations from 3000 to 3250 m, implying some level of perturbation from the hydrothermal intrusion (Fig. 4c), but these were not as strong as in PL and not accompanied with an increase in δ^{13}C-CH_4 values or methane concentrations. We found one exception to this at NP1, which was also at the northern side of the vents. Here, methane concentration (1.7 nM) and δ^{13}C-CH_4 (-43 ‰) were elevated at 3350 m, i.e., just below the turbidity anomaly.

Deep-water methane stable carbon isotope compositions in the Arctic Ocean have previously been reported with values ranging from -63 ‰ to -58 ‰ in the Beaufort and Chukchi seas, along with higher concentrations of methane of up to 55 nM (Damm et al., 2008; Kudo et al., 2018; Lorenson et al., 2016). These are attributed to microbial methanogenesis overprinting the atmospheric methane equilibrium signature (typically ~ 3.5 nM and -47 ‰). We observed a similar range of δ^{13}C-CH_4 values with much lower concentrations of methane (e.g., -64.7 ‰ and 0.3 nM) at BG (3250 m) and argue that these values may also be caused by methanogenesis, possibly in sediments or even in the water column (Damm et al., 2010; Grossart et al., 2011; Karl et al., 2008), but we suggest that methanotrophs also consume methane there (Reeburgh, 2007). In contrast, we found relatively heavy methane isotope values together with maximum methane concentrations in the plume layer at PL (e.g., -33 ‰ and 5.1 nM) (Fig. 4). Methane at hydrothermal vents is typically produced non-biologically, either by abiogenic (C reduction) or thermogenic (breakdown) processes, and is generally characterized by much higher δ^{13}C values (Whiticar, 1999; Reeves and Fiebig, 2020; Baumberger et al., 2016, and references therein). Abiogenic δ^{13}C-CH_4 values of ca. -5 ‰ to -20 ‰ are typically found in bare rock (mafic/ultramafic systems), while lower (thermogenic) values of ~ -25 ‰ to -56 ‰ are prevalent in systems influenced by hydrothermal alteration of sedimentary organic matter (Charlou et al., 2002; Baumberger et al., 2016; Wang et al., 2018; and references therein). Hence, the higher δ^{13}C-CH_4 values detected at PL provide strong evidence for a similar non-biogenic origin of plume methane venting from the Aurora site. While δ^{13}C-CH_4 values measured at the Aurora hydrothermal field are relatively depleted compared to many bare-rock-hosted hydrothermal systems, to some degree, this can be explained by both the distal nature of PL samples relative to the more concentrated buoyant plume and admixing of background seawater with its extremely isotopically depleted δ^{13}C signature and low methane concentration values (-64.7 ‰ and 0.3 nM).

To further probe the dynamics of water column methane dynamics at Aurora, we applied a Keeling mixing model approach (Keeling, 1961; Keir et al., 2006). This end-member isotope mixing model is widely used in the fields of atmospheric chemistry/physics to analyze admixtures of two isotopically distinct gas sources and to determine the source isotope composition (e.g., Pataki et al., 2003). In a Keeling plot, the reciprocal of concentration is plotted against isotope composition (Fig. 5). In case of a linear mixing, the values scatter along a straight line, and the intercept with the y axis denotes the isotope value of the source signal. Our values of methane concentration and isotope composition show predominantly linear behavior, indicating that the mixing and dilution dominates the observed concentration and isotope systematics, as has been found in other Arctic settings (Damm and Budéus, 2003; Graves et al., 2015). More complex mixing scenarios involving mixing and methane oxidation were also suggested to explain methane isotope patterns in hydrothermal plumes (Keir et al., 2009). Though we cannot completely rule out some extent of microbial methane oxidation (particularly in the most distal samples), this process is

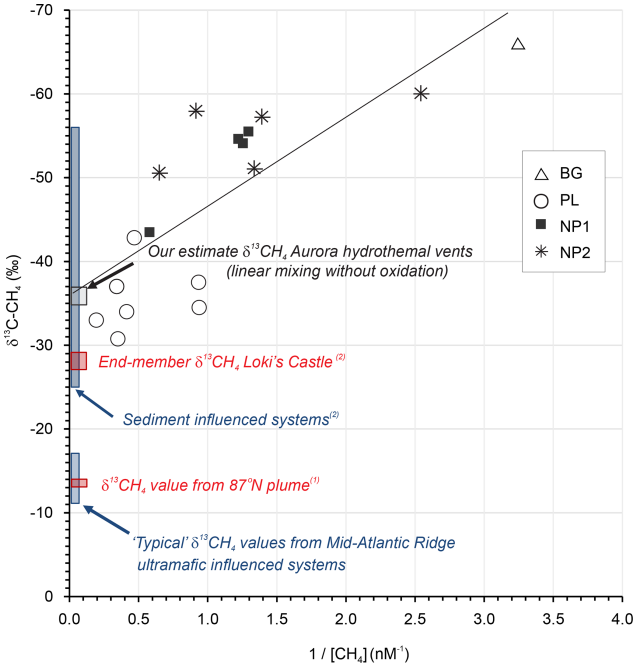

Figure 5. Keeling plot for δ^{13}C-CH_4 versus $1/[CH_4]$ for the data obtained in background (BG), upper layer (UL), plume (PL) and non-plume (NP1–NP3) stations (Keeling, 1961; Keir et al., 2006). Plotted also are "closest approach" δ^{13}C-CH_4 value reported for the 87° N hydrothermal plume on the Gakkel Ridge ([1] McDermott et al., 2017), end-member hydrothermal fluid δ^{13}C-CH_4 values from Mid-Atlantic Ridge black smoker systems known to be influenced by ultramafic rock, and the sediment-influenced Loki's Castle system ([2] Baumberger et al., 2016, and references therein).

associated with a significant kinetic isotope effect (Whiticar, 1999) and can even result in extremely high δ^{13}C-CH_4 values in microbially aged hydrothermal plumes (Keir et al., 2006; Cowen et al., 2002) . If such oxidation were pronounced, it would lead to substantial curvature in a Keeling plot by shifting the residual methane towards heavier isotopic values at lower concentrations (higher $1/[CH_4]$).

Considering a "mixing without oxidation" scenario and under the assumption of linear mixing (Keir et al., 2009), we estimate the $\delta^{13}CH_4$ value of the hydrothermal fluid source to be -36 ‰ using a least squares linear regression of the entire plume methane dataset ($R^2 = 0.59$), with an intercept uncertainty of ± 3 ‰ at the Aurora hydrothermal field (Fig. 5). The estimate is interesting, since the Aurora hydrothermal system has, thus far, been postulated to be hosted in ultramafic rock (German and Boetius, 2017; Marcon et al., 2017). The $\delta^{13}CH_4$ estimate presented here is substantially lower than both plume and end-member $\delta^{13}CH_4$ values of many Mid-Atlantic Ridge hydrothermal vents known to be hosted in or influenced by ultramafic rock (ca. -5 to -20, e.g., Keir et al., 2006; Wang et al., 2018). Such ranges are assumed to be characteristic of putatively abiotic methane (e.g., Wang et al., 2018), most likely derived from leaching of rock-hosted gas inclusions (e.g., Grozeva et al., 2020). A $\delta^{13}CH_4$ value -13.1 ‰ within this range of has also been reported for a "closest approach" in a CH_4- and H_2-rich hydrothermal plume further east on the Gakkel Ridge at 87° N (McDermott et al., 2017; confirmed by the same cavity ring-down spectrometry approach used here), also postulated to reflect ultramafic influence. In contrast, $\delta^{13}CH_4$ values in hydrothermal fluids either heavily influenced by (or hosted in) sediments undergoing substantial thermal alteration of associated sedimentary organic matter tend to be generally more ^{13}C-depleted (ranging from -25 ‰ to -56 ‰; Baumberger et al., 2016, and references therein). Indeed, similarly intermediate values of $\delta^{13}CH_4$ (-27 ‰ to -29 ‰) compared to Mid-Atlantic Ridge hydrothermal systems were also obtained in the bare-rock-hosted, but sediment-influenced, Loki's Castle hydrothermal system farther to the south on the ultraslow-spreading Mohns–Knipovich ridge junction of the Arctic Mid-Ocean Ridge system (Baumberger et al., 2016; Pedersen et al., 2010). There, exceptionally high methane (15.5 mM) and ammonium (6.1 mM) concentrations together with low C_1/C_{2+} ratios are attributed to subsurface hydrothermal fluid–sediment interactions (linked to sediment accumulation at ridge flanks and ridge valley, Baumberger et al., 2016; Pedersen et al., 2010).

A greater extent of plume dispersion and somewhat higher methane concentrations (≤ 32 nM) were previously reported within ~ 200 m of the Aurora hydrothermal vent area (Boetius, 2015; German and Boetius, 2017), but the maximum concentrations reported here (2.8–5.1 nM, in station PL) do at least coincide with the highest $\delta^{13}CH_4$ values (-31 ‰ to -33 ‰) and maximum water column turbidity. Hence, we tentatively suggest that hydrothermal fluids at Aurora might, on the basis of these closest approach plume $\delta^{13}CH_4$ values alone, potentially contain a thermogenic organic matter influence.

3.3 Composition of DOM in the sea ice, water column and in the hydrothermal plume layer

Analyses of DOM extracts revealed 8093 unique formulas in the whole dataset, with the molecular mass range between 150 and 1000 Da. From all unique formulas, 2614 and 2391 were uniquely obtained by negative and positive ESI, respectively, and 3088 formulas were assigned in both (see Fig. S3 in the Supplement). In agreement with previous findings (Ohno et al., 2016; Sert et al., 2020), unique positive ESI formulas were markedly more hydrogen saturated (average $H:C = 1.51$) and oxygen-poor (average $O:C = 0.31$) compared to negative ESI formulas (average $H:C = 1.13$ and $O:C = 0.58$). Numbers of assignments for aliphatic and lipid-like DOM components were more abundant in positive mode, and unsaturated oxygen-rich molecular formulas, carbohydrates, and lignin-like and aromatic compounds were more abundant in negative mode. Considering the features obtained in different modes (Fig. S4 in the Supplement),

combining positive and negative ESI datasets provides a considerable advantage for differentiating samples.

3.3.1 Sea ice

The DOM composition of sea ice was determined from a single sample and indicates that it was predominantly more hydrogen saturated relative to surface water composition (i.e., higher H/C ratios), with a lower number of formulas, average relative intensities, average molecular weights and considerably high LPD content (Fig. 6a–k). Differences in molecular composition between seawater and sea ice are in agreement with previous observations in sea ice DOM (Longnecker, 2015; Retelletti Brogi et al., 2018) and lake ice DOM (Liu et al., 2020; Santibáñez et al., 2019; Xu et al., 2020), implying a selective transport of DOM with less complex, aliphatic compounds, rather than larger aromatic oligomers, during ice formation. The hydrodynamics of DOM transport are not known between phases, but previous observations show that DOM segregates between water and ice, favoring lower MW formulas and less aromatic fractions in the ice phase (Belzile et al., 2002; Santibáñez et al., 2019). In the Arctic Ocean, this partition process increases the bioavailability of terrestrial DOM from rivers during initial ice formation and contributes to its removal by retaining biologically active components (Jørgensen et al., 2015). In addition to the abiotic fractionation and transport, biofilm-mediated microbial degradation and photooxidation were previously shown to be responsible for fast degradation of petroleum biopolymers in sea ice (Vergeynst et al., 2019). High LPD percentage and low average MW in sea ice DOM may also be attributed to a fresh production by ice algae or heterotrophic degradation of DOM (Hill and Zimmerman, 2016; Li et al., 2019; Retelletti Brogi et al., 2018).

3.3.2 Upper 1000 m of the water column

From the sea surface down to 1000 m, changes in DOM indices such as the number of formulas, molecular diversity and average relative intensities are consistent with changes in nutrient and DOC showing their maxima at 5 m (Figs. 6a–d and 3a–e). This is in agreement with the expected pace and diversity of biological processes in this water layer, i.e., dissolved nutrient uptake by phytoplankton and the contribution to the synthesis of dissolved and particulate organic matter (Benner et al., 1992; Hedges, 1992). Below this layer, average relative intensities of formulas decreased and showed a less diverse composition below the photic zone with decreasing light availability and heterotrophic consumption (Fig. 6b–d).

The uptake of bioavailable DOM alongside nutrients could explain the distribution of formulas of different chemical classes in the 0–1000 m layer. For example, lower abundances of LPD and LGN at the surface against the higher CAR and UNC contents (Fig. 6e–h) indicate the selective use of the more hydrogenated aliphatic compounds compared to oxygenated or aromatic formulas. Similarly, CHON and CHOS heteroatom contents were higher at the surface compared to subsurface contents up to 500 m depth (Fig. 6i–k), indicating the increase in the molecular variability and abundance of fresh DOM (Coch et al., 2019; Hertkorn et al., 2016; Jaffé et al., 2012). In contrast to bulk dissolved organic nitrogen (DON) concentrations and CHOS heteroatom contents, percentages of CHON formulas systematically increased from the subsurface ($\sim 33\,\%$) to 1000 m to reach $\sim 50\,\%$ of deep-water abundances (Fig. 6j). Taking this together with the CAR and LPD percentages at subsurface layers, surface-derived carbohydrates are presumably used with increasing depth by heterotrophs to build up cell materials where N-containing proteins dominate intracellular biochemicals (Aluwihare and Meador, 2008) .

For a detailed examination of the DOM structure in the upper layer (i.e., 0–1000 m) a more extensive dataset would be required. However, changes in the percentages of the molecular formulas seem to indicate the gradual transformation of semi-labile DOM at the surface to semi-refractory DOM in the mesopelagic zone (200–1000 m) (see Hansell, 2013). This trend was evident in most of the profiles displaying molecular percentages (Fig. 6e–k).

3.3.3 Hydrothermal plume and the surroundings

The influence of the plume dispersion on DOM composition was investigated in 11 samples from three stations below 2000 m: BG (background), PL (plume) and NP2 (non-plume). The approximate locations of these samples relative to hydrothermal vents and the possible route of the plume dispersion are depicted in Fig. 7a. PCoA and hierarchical clustering indicate a similar composition in the samples obtained from the same station (Fig. 7b and c). Exceptions are samples PL-3000 and BG-2000, which display higher molecular diversity and number of formulas and are therefore more similar to NP2 samples (Fig. 7b). Nevertheless, samples from different depths but from the same station prominently group into three separate clusters (Fig. 7a–c).

The detailed DOM formula compositions as depicted by van Krevelen diagrams reveal compositional differences between BG, PL and NP2 samples (Fig. 8). All van Krevelen diagrams are populated by a large number of molecular formulas with H : C ratios in the range of 1.0 to 1.8 and O : C ratio of 0.1 to 0.9. In general, the compositions in BG and PL samples display a similar distribution of formulas (Fig. 8a–i). However, BG samples have more formulas, especially at regions $\mathrm{H:C} \geq 2.0$ and $\mathrm{O:C} \leq 1.0$ compared to samples at PL. Contrary to BG and PL, NP2 samples have a higher number of formulas and higher frequency of oxygen-containing formulas (i.e., O : C ratio extended until 1.5) and almost no formulas with $\mathrm{H:C}$ ratio ≤ 0.5 (Fig. 8j and k).

Considering that the plume dispersion mainly occurs along a lateral transect, we collected samples at the same depths

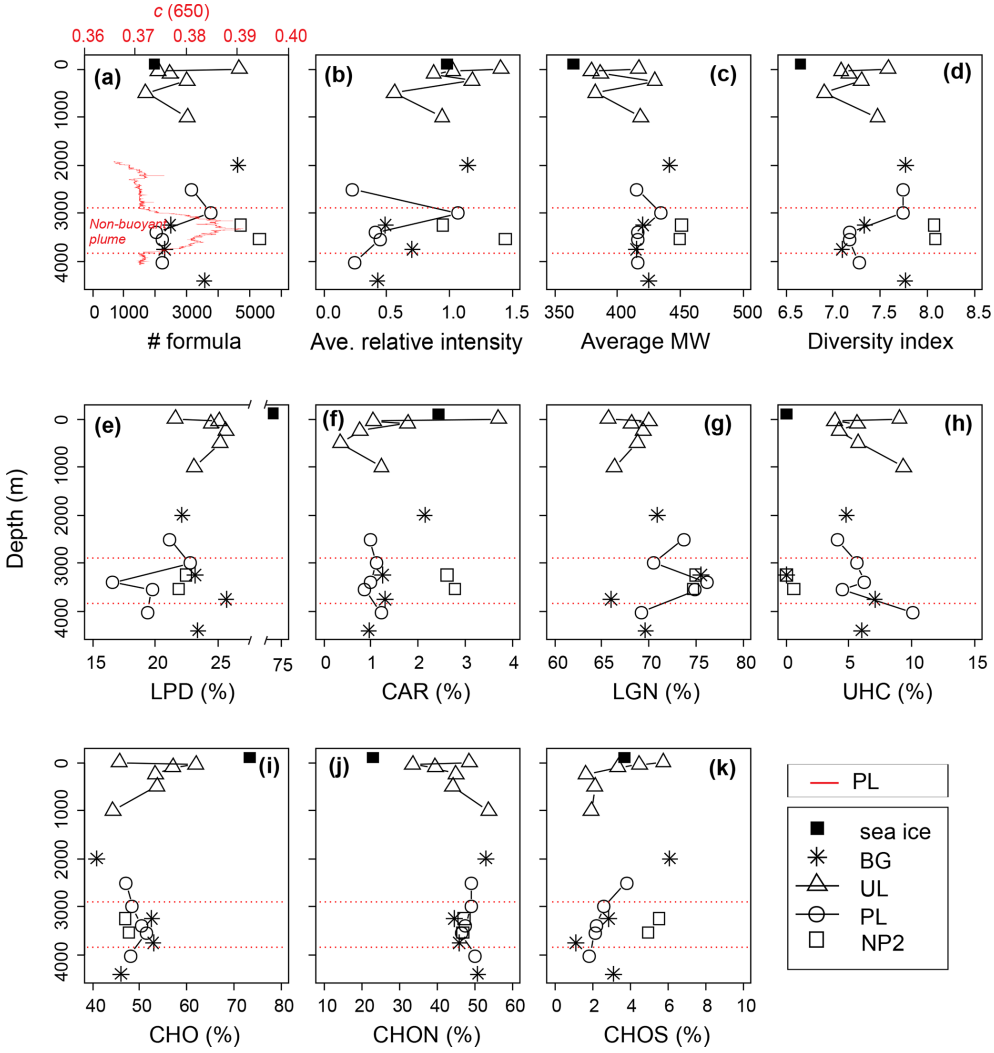

Figure 6. Depth profiles of the dissolved organic matter (DOM) composition, **(a–d)** molecular indices, **(e–h)** percentages of number of formulas in biochemical compound groups defined by H : C and O : C ratios, and **(i–k)** heteroatomic content in background (BG), upper layer (UL), plume (PL) and non-plume (NP2) stations. Abbreviations are MW, molecular weight; LPD, lipid- and protein-like; CAR, carbohydrate-like; LGN, lignin- and tannin-like; UHC, unsaturated hydrocarbon- and condensed aromatic-like; O : C, oxygen-to-carbon ratio; and H : C, hydrogen-to-carbon ratio. The beam attenuation profile of PL is added to the first panel to indicate the non-buoyant plume layer, and corresponding boundaries of the plume layer are indicated by red dashed lines in all panels.

along this lateral transect to be able to compare the differences in the DOM composition (e.g., BG-3250 vs. NP2–3250 m and PL-3500 vs. NP2-3500; Fig. 8b, h, j and k, respectively). Formulas that were unique (i.e., formulas that were not present in samples from the same layer in other stations) or distinct molecular indices (i.e., percentages in different molecular classes like LPD or CAR) were used to evaluate changes in DOM composition. Variations in these molecular properties might be related to distinct biogeochemical settings associated with the plume dispersion, as found with turbidity, methane concentrations and $\delta^{13}C$-CH_4 contents. For example, low molecular diversity, average relative intensities and LPD content in PL-3500 and PL-3400 (Fig. 6a–e) indicate the effect of hydrothermal intrusion or the molecular composition carried by the plume, in line with previous experimental and environmental data suggesting preferential removal of higher-molecular-weight and oxygen-rich compounds under hydrothermal conditions (Hawkes et al., 2016; Rossel et al., 2017).

Given that the DOM composition throughout the region is thermally altered, the nature of thermal alteration of organic matter at the hydrothermal systems has been previously formulated as (i) reduction of organic compounds in low-temperature regions ($\sim$ 60–150 °C) to generate products from weaker bonds (e.g., formation of petroleum, aliphatic hydrocarbons) (Simoneit, 1992), (ii) oxidation at higher-

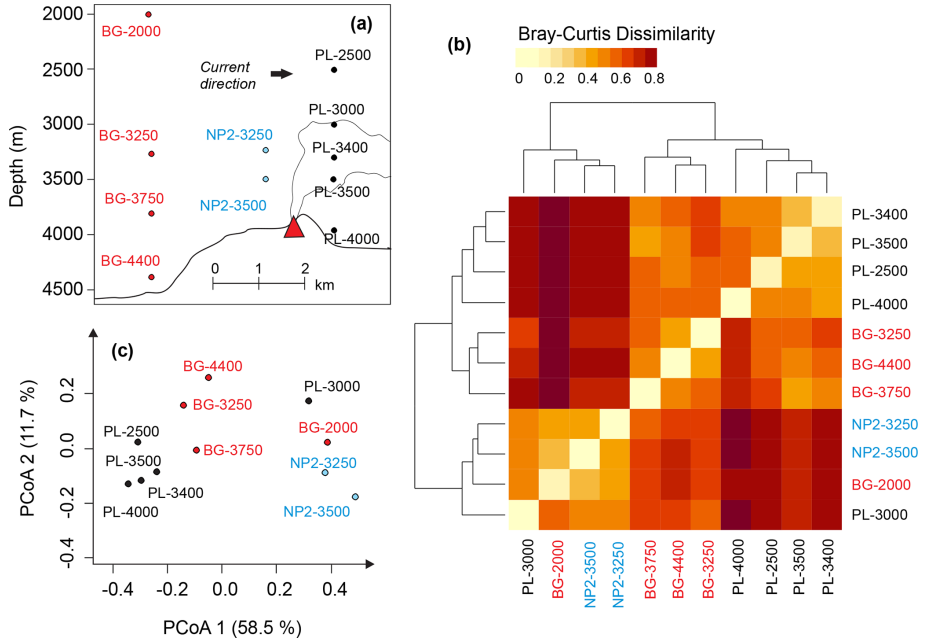

Figure 7. **(a)** Relative positions of the dissolved organic matter (DOM) samples below 2000 m and the hydrothermal plume. **(b)** Heat-map representing the relation between hierarchical clustering of DOM compositions based on Bray–Curtis dissimilarity. **(c)** Principal coordinate analysis (PCoA) based on Bray–Curtis dissimilarity of DOM composition samples. Sample names are coded as station name and the approximate depth of the sample for background (BG), upper layer (UL), plume (PL) and non-plume (NP2) stations.

temperature conditions (e.g., PAHs and alkanones) (Dittmar and Koch, 2006; Simoneit, 1995) and (iii) abiotic synthesis of organic matter by thermocatalytic (Fischer–Tropsch-type) reactions (McCollom et al., 1999; McCollom and Seewald, 2007). Therefore, it is difficult to categorize thermal processes as either a source or a sink mechanism for marine DOM over a range of temperatures from ∼ 60 to ∼ 150 °C due to, for instance, formation of petroleum products (Simoneit, 1992), water-soluble vitamins and amino acids (Longnecker et al., 2018), elevated concentrations of formate, acetate concentrations (Lang et al., 2010; McDermott et al., 2015), fractions of labile compositions (Hansen et al., 2019), and formation of iron- and sulfur-bearing organic ligands (Yücel et al., 2011). During high-temperature hydrothermal circulation, however, ∼ 94 % of the solid phase extractable DOC is typically removed (Hawkes et al., 2015). Findings at several Mid-Atlantic Ridge hydrothermal systems and temperature-controlled hydrothermal experiments showed that DOM is highly unstable and effectively removed during hydrothermal circulation, with a reduction in the abundance of recalcitrant DOM and a decrease in the number of formulas and average molecular mass (Hawkes et al., 2015, 2016; Rossel et al., 2015, 2017).

This agrees with our observations of a decreasing number of molecular formulas, molecular diversity, average relative intensity and LPD composition in the samples where plume-related hydrochemistry was manifested by a higher level of turbidity, 5 times higher methane concentration and markedly heavier methane carbon isotope compositions. We can therefore assume that the compositional differences between background seawater in BG samples and DOM in the plume layer (PL-3400) may be due to hydrothermal degradation or some other chemical combination of reactions that result in a molecular signal similar to those reported for hydrothermal fluids. Due to the difficult sampling situation in the high-Arctic marine environment, we were unfortunately unable to take samples directly from the buoyant plume of the vent to properly illustrate the distribution and composition of hydrothermal end-member DOM. Our analysis, therefore, is solely based on compositional comparison between samples that were different in their relative position to the vent and its non-buoyant plume. However, we do suggest that a portion of the observed composition in the PL is associated with the hydrothermal fluids, which are efficient at scavenging hydrothermal organic compounds from the vent area and transporting them from the heated subsurface (Simoneit, 1992). Accordingly, the temperature profile at PL implies that the hydrothermal fluids must have been cooled down to the ambient temperature before reaching the sampling point. Therefore, any thermal modifications in DOM compositions must have occurred either before entering the lithosphere or in areas adjacent to the vents themselves, being merely carried along with the plume-transported particles, dissolved gases, or water masses and gradually diluted with the surrounding waters until it reached the sampling location.

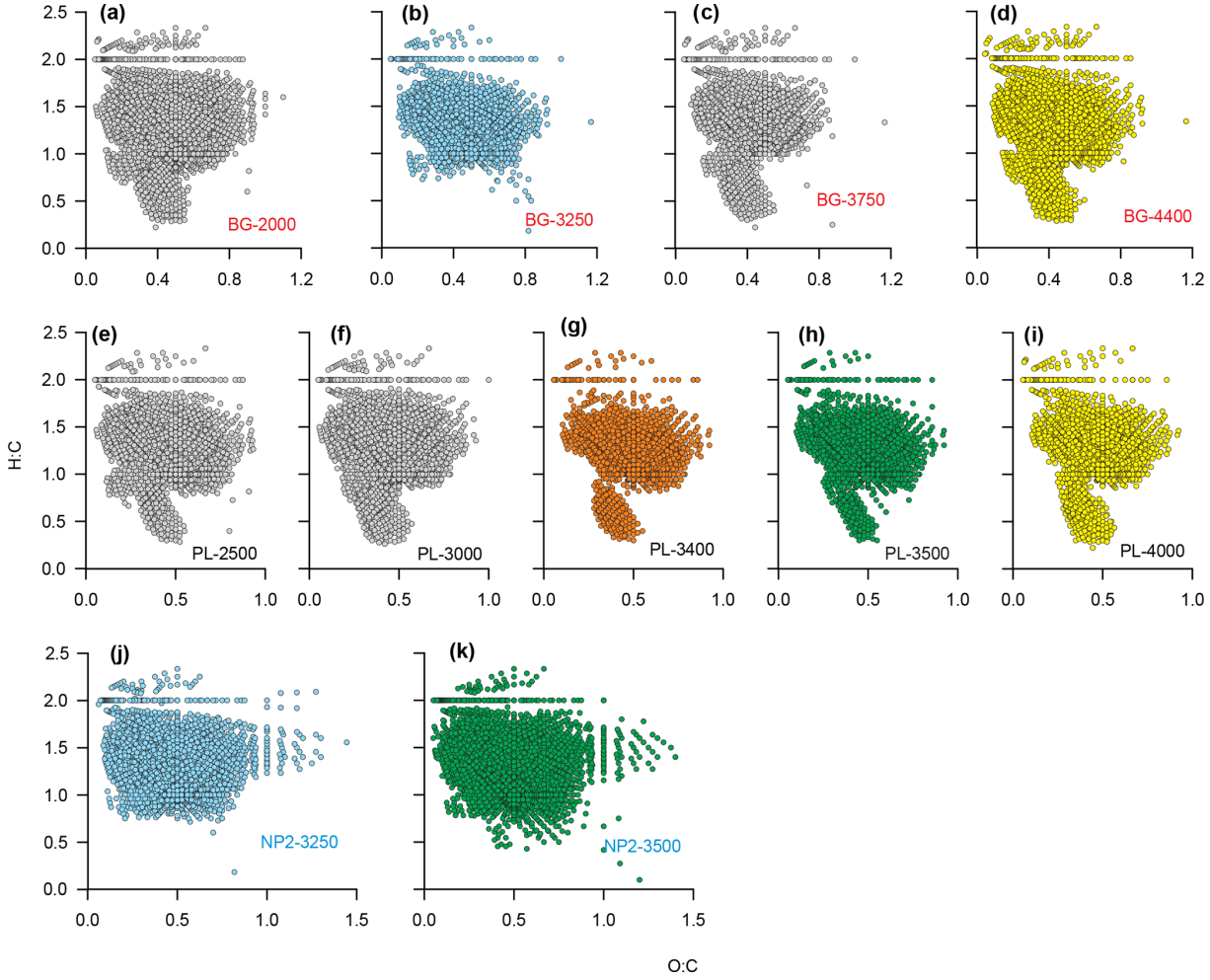

Figure 8. Dissolved organic matter (DOM) formulas on van Krevelen diagrams showing O : C and H : C ratios of the formulas at stations **(a–d)** BG, **(e–i)** PL and **(j–k)** NP2. Sample names are coded as station name and sample depth. Orange color is given to PL-3400, where the plume effect is expected to be the highest. Blue and green are used for the formulas in samples that were taken from same depths at different stations. Yellow color is for the samples that were taken from the bottom of the water column at BG and PL.

Alternatively, unique formula compositions in NP2 with higher oxygen saturation (i.e., O : C $\geq$ 1) or $\sim$ 2 % higher CAR content (see Fig. 6f) could be a product of microbial enrichment attributed to chemosynthetic activity at the southern part of the seamount where the faunal communities, sponges, amphipods and traces of biological activity were more abundant as logged by video and photographic transects from OFOBS dives (Bünz et al., 2020). Nevertheless, based on our data, a clear and direct link between activity of faunal communities and DOM molecular compositions could not be made. Because of this, we cannot yet suggest any mechanism that can transfer modifications of benthic communities to pelagic DOM compositions.

One other plausible explanation for the differences in molecular composition in PL and NP2 compared to BG could be a change in the current direction. The current direction could have been different in the past compared to what we observed on our cruise. If this were the case, the observed composition at the NP2 station could be an imprint of a previous composition of the hydrothermal vent or some other form of environmental gradient that modified and diversified the DOM composition at NP2, while the PL samples reflect the current composition at the sampling location. The higher abundance of CHOS heteroatom composition in the NP2 samples could be evidence of that. A very recent study in Kairei and Pelagia hydrothermal vents in the Indian Ocean indicate 17 % more CHOS molecular formulas in DOM from hot vent fluids along with the elevated hydrogen sulfide concentrations compared to surrounding seawater (Noowong et al., 2021). Similarly, reproduction of sulfur-containing compounds is found to occur under experimental hydrothermal conditions at several selected temperatures (Hawkes et al., 2016) and at less acidic conditions (Rossel et al., 2017).

4 Summary and conclusion

Our investigations of the water column above the Aurora hydrothermal vent field (Gakkel Ridge, Arctic Ocean) show that hydrothermal venting in this region displaces thermally degraded DOM compositions within the hydrothermal plume, along with ^{13}C-enriched methane and other vent-derived properties. We show that DOM compositions in the plume layer samples had lower numbers of molecular formulas, molecular diversity, average relative intensity, and percentage of formulas assigned to the LPD molecular class. However, at a site with higher vent-related biological imprinting and lower influence from plume dispersion, DOM compositions had higher numbers of formulas, molecular diversity, and CAR percentages. We characterized the water column hydrophysical and biochemical properties, observing that nutrient distributions and DOM compositions mainly reflect vertical changes in primary production, atmospheric gas exchange, riverine influence and water mass distributions in the upper 1000 m layer, while the water column below 2000 m was quite uniform. DOM composition in sea ice was more labile, with markedly high LPD and low-molecular-weight compositions than the ocean surface waters, suggesting selective transport during ice formation and new production by ice algae.

DOM compositions in the Arctic Ocean are prone to changes in the upper ocean layers, in parallel to the changes in global climate and decline in sea ice extent. However, deep-ocean DOM is mostly refractory, displaying remnants of ancient biological processes. Hydrothermal vents in the deep ocean could therefore be a dynamic source of organic matter and perhaps influence overlying pelagic ecosystems. There are several experimental studies on how DOM is modified during hydrothermal processes under different physical and chemical conditions; however, there is a gap of knowledge on to what extent hydrothermally and chemosynthetically modified DOM spreads along plume layers, altering water column biogeochemistry. To the best of our knowledge, our study is the first attempt to differentiate hydrothermal plume and non-plume DOM compositions in the deep Arctic Ocean; clearly more studies should address this in different hydrothermal systems and other plume-generating deep-sea environments.

Code and data availability. The data and the codes for generating figures and statistical analyses are available in UiT Open Research Data repository https://doi.org/10.18710/QPGDFW (Sert et al., 2021).

Supplement. The supplement related to this article is available online at: https://doi.org/10.5194/bg-19-2101-2022-supplement.

Author contributions. MFS designed the study and performed data acquisition with supervision from AS, FG and HN. EPR and KPH analyzed shipboard methane concentrations and methane carbon isotope compositions, respectively. TK and JJ analyzed dissolved organic matter samples, generated formula lists and wrote mass spectrometry methodology. MFS wrote the manuscript with contributions from all coauthors.

Competing interests. At least one of the (co-)authors is a member of the editorial board of *Biogeosciences*. The peer-review process was guided by an independent editor, and the authors also have no other competing interests to declare.

Disclaimer. Publisher's note: Copernicus Publications remains neutral with regard to jurisdictional claims in published maps and institutional affiliations.

Acknowledgements. We would like to acknowledge the crew of R/V *Kronprins Haakon*, chief scientist Stefan Bünz and co-chief scientist Eva Ramirez-Llodra for their tremendous efforts during this challenging expedition. We would like to thank Autun Purser and Ulrich Hoge for OFOBS observations, Colin A. Stedmon for DOC and TDN measurements, and Linda Fondes Lunde for nutrient analyses. This study is a part of CAGE (Centre for Arctic Gas Hydrate, Environment and Climate), Norwegian Research Council (grant no. 223259). The HACON project is funded by the Research Council of Norway through a FRINATEK grant (274330). This study is supported by European Union's Horizon 2020 research and innovation program (EU FT-ICR MS project; grant agreement 731077). The FT-ICR MS facility is also supported by Biocenter Finland, Biocenter Kuopio and the European Regional Development Fund (grant A70135). Kevin P. Hand contributed this research through support from the Exo-Ocean Worlds project within the Astrobiology Program at NASA and through support from the Jet Propulsion Laboratory, California Institute of Technology, under a contract with the National Aeronautics and Space Administration (80NM0018D0004). Pamela E. Rossel is funded by a European Research Council (ERC) Synergy Grant (DEEP PURPLE, grant agreement no. 856416) awarded under the European Union's Horizon 2020 research and innovation program. The publication charges for this article have been funded by a grant from the publication fund of UiT The Arctic University of Norway.

Financial support. This research has been supported by the Norges Forskningsråd (grant nos. 223259 and 274330).

Review statement. This paper was edited by Yuan Shen and reviewed by two anonymous referees.

References

Aluwihare, L. I. and Meador, T.: Chemical Composition of Marine Dissolved Organic Nitrogen, in: Nitrogen in the Marine Environment (Second edn.), edited by: Capone, D. G., Bronk, D. A., Mulholland, M. R., and Carpenter, E. J., Academic Press, San Diego, 95–140, https://doi.org/10.1016/B978-0-12-372522-6.00003-7, 2008.

Arrieta, J. M., Mayol, E., Hansman, R. L., Herndl, G. J., Dittmar, T., and Duarte, C. M.: Dilution limits dissolved organic carbon utilization in the deep ocean, Science, 348, 331–333, https://doi.org/10.1126/science.1258955, 2015.

Arrigo, K. R. and van Dijken, G. L.: Continued increases in Arctic Ocean primary production, Prog. Oceanogr., 136, 60–70, https://doi.org/10.1016/j.pocean.2015.05.002, 2015.

Baker, E. T., German, C. R., and Elderfield, H.: Hydrothermal Plumes Over Spreading-Center Axes: Global Distributions and Geological Inferences, in: Seafloor Hydrothermal Systems: Physical, Chemical, Biological, and Geological Interactions, American Geophysical Union (AGU), 47–71, https://doi.org/10.1029/GM091p0047, 1995.

Bart, M. C., de Kluijver, A., Hoetjes, S., Absalah, S., Mueller, B., Kenchington, E., Rapp, H. T., and de Goeij, J. M.: Differential processing of dissolved and particulate organic matter by deep-sea sponges and their microbial symbionts, Sci. Rep., 10, 17515, https://doi.org/10.1038/s41598-020-74670-0, 2020.

Bauch, D., Schlosser, P., and Fairbanks, R. G.: Freshwater balance and the sources of deep and bottom waters in the Arctic Ocean inferred from the distribution of H2180, Prog. Oceanogr., 35, 53–80, 1995.

Bauch, D., Polyak, L., and Ortiz, J. D.: A baseline for the vertical distribution of the stable carbon isotopes of dissolved inorganic carbon (δ13CDIC) in the Arctic Ocean, Arktos, 1, 15, https://doi.org/10.1007/s41063-015-0001-0, 2015.

Baumberger, T., Früh-Green, G. L., Thorseth, I. H., Lilley, M. D., Hamelin, C., Bernasconi, S. M., Okland, I. E., and Pedersen, R. B.: Fluid composition of the sediment-influenced Loki's Castle vent field at the ultra-slow spreading Arctic Mid-Ocean Ridge, Geochim. Cosmochim. Ac., 187, 156–178, https://doi.org/10.1016/j.gca.2016.05.017, 2016.

Beaulieu, S. E., Baker, E. T., and German, C. R.: Where are the undiscovered hydrothermal vents on oceanic spreading ridges?, Deep-Sea Res. Pt. II, 121, 202–212, https://doi.org/10.1016/j.dsr2.2015.05.001, 2015.

Belzile, C., Gibson, J. A. E., and Vincent, W. F.: Colored dissolved organic matter and dissolved organic carbon exclusion from lake ice: Implications for irradiance transmission and carbon cycling, Limnol. Oceanogr., 47, 1283–1293, https://doi.org/10.4319/lo.2002.47.5.1283, 2002.

Benner, R., Pakulski, J. D., Mccarthy, M., Hedges, J. I., and Hatcher, P. G.: Bulk Chemical Characteristics of Dissolved Organic Matter in the Ocean, Science, 255, 1561–1564, https://doi.org/10.1126/science.255.5051.1561, 1992.

Boetius, A.: The Expedition PS86 of the Research Vessel POLARSTERN to the Arctic Ocean in 2014, Alfred-Wegener-Institut Helmholtz-Zentrum für Polar- und Meeresforschung, ISSN 1866-3192, https://doi.org/10.2312/BzPM_0685_2015, 2015.

Boetius, A., Bach, W., Borowski, C., Diehl, A., German, C. R., Kaul, N. E., Koehler, J., Marcon, Y., Mertens, C., Molari, M., Schlindwein, V. S. N., Tuerke, A., and Wegener, G.: Exploring the Habitability of Ice-covered Waterworlds: The Deep-Sea Hydrothermal System of the Aurora Mount at Gakkel Ridge, Arctic Ocean (82°54′ N, 6°15 W, 3900 m), AGU Fall Meeting Abstracts, 15–19 December 2014, San Francisco, B24A-02, 2014.

Bray, J. R. and Curtis, J. T.: An Ordination of the Upland Forest Communities of Southern Wisconsin, Ecol. Monogr., 27, 325–349, https://doi.org/10.2307/1942268, 1957.

Bünz, S., Ramirez-Llodra, E., German, C., Ferre, B., Sert, F., Kalenickenko, D., Reeves, E., Hand, K., Dahle, H., Kutti, T., Purser, A., Hilario, A., Ramalho, S., Rapp, H. T., Ribeiro, P., Victorero, L., Hoge, U., Panieri, G., Bowen, A., Jakuba, M., Suman, S., Gomez-Ibanez, D., Judge, C., Curran, M., Nalicki, V., Vagenes, S., Lamar, L., Klesh, A., Dessandier, P. A., Steen, I., Mall, A., Vulcano, F., Meckel, E. M., and Drake, N.: RV Kronprins Håkon (cruise no. 2019708) Longyearbyen – Longyearbyen 19.09.–16.10.2019, UIT – The Arctic University of Norway, 100 pp., https://haconfrinatek.com/2020/01/20/hacon-cruise-report/f (last access: 14 April 2022), 2020.

Burd, B. J. and Thomson, R. E.: Hydrothermal venting at endeavour ridge: effect on zooplankton biomass throughout the water column, Deep-Sea Res. Pt. I, 41, 1407–1423, https://doi.org/10.1016/0967-0637(94)90105-8, 1994.

Charlou, J. L., Donval, J. P., Fouquet, Y., Jean-Baptiste, P., and Holm, N.: Geochemistry of high H_2 and CH_4 vent fluids issuing from ultramafic rocks at the Rainbow hydrothermal field (36°14′ N, MAR), Chem. Geol., 191, 345–359, https://doi.org/10.1016/S0009-2541(02)00134-1, 2002.

Coch, C., Juhls, B., Lamoureux, S. F., Lafrenière, M. J., Fritz, M., Heim, B., and Lantuit, H.: Comparisons of dissolved organic matter and its optical characteristics in small low and high Arctic catchments, Biogeosciences, 16, 4535–4553, https://doi.org/10.5194/bg-16-4535-2019, 2019.

Cowen, J. P., Wen, X., and Popp, B. N.: Methane in aging hydrothermal plumes, Geochim. Cosmochim. Ac., 66, 3563–3571, https://doi.org/10.1016/S0016-7037(02)00975-4, 2002.

Damm, E. and Budéus, G.: Fate of vent-derived methane in seawater above the Håkon Mosby mud volcano (Norwegian Sea), Mar. Chem., 82, 1–11, https://doi.org/10.1016/S0304-4203(03)00031-8, 2003.

Damm, E., Kiene, R. P., Schwarz, J., Falck, E., and Dieckmann, G.: Methane cycling in Arctic shelf water and its relationship with phytoplankton biomass and DMSP, Mar. Chem., 109, 45–59, https://doi.org/10.1016/j.marchem.2007.12.003, 2008.

Damm, E., Helmke, E., Thoms, S., Schauer, U., Nöthig, E., Bakker, K., and Kiene, R. P.: Methane production in aerobic oligotrophic surface water in the central Arctic Ocean, Biogeosciences, 7, 1099–1108, https://doi.org/10.5194/bg-7-1099-2010, 2010.

de la Vega, C., Jeffreys, R. M., Tuerena, R., Ganeshram, R., and Mahaffey, C.: Temporal and spatial trends in marine carbon isotopes in the Arctic Ocean and implications for food web studies, Glob. Change Biol., 25, 4116–4130, https://doi.org/10.1111/gcb.14832, 2019.

DeMets, C., Gordon, R., and Argus, D.: Geological current plate motions, Geophys. J. Int., 181, 1–80, https://doi.org/10.1111/j.1365-246X.2009.04491.x, 2010.

Dick, G. J.: The microbiomes of deep-sea hydrothermal vents: distributed globally, shaped locally, Nat. Rev. Microbiol., 17, 271–283, https://doi.org/10.1038/s41579-019-0160-2, 2019.

Dittmar, T. and Koch, B. P.: Thermogenic organic matter dissolved in the abyssal ocean, Mar. Chem., 102, 208–217, https://doi.org/10.1016/j.marchem.2006.04.003, 2006.

Dittmar, T. and Stubbins, A.: Dissolved Organic Matter in Aquatic Systems, in: Treatise on Geochemistry, edited by: Holland, H. D. and Turekian, K. K., Elsevier, Oxford, 125–156, https://doi.org/10.1016/B978-0-08-095975-7.01010-X, 2014.

Dittmar, T., Koch, B., Hertkorn, N., and Kattner, G.: A simple and efficient method for the solid-phase extraction of dissolved organic matter (SPE-DOM) from seawater, Limnol. Oceanogr.-Meth., 6, 230–235, 2008.

Edmonds, H. N., Michael, P. J., Baker, E. T., Connelly, D. P., Snow, J. E., Langmuir, C. H., Dick, H. J. B., Mühe, R., German, C. R., and Graham, D. W.: Discovery of abundant hydrothermal venting on the ultraslow-spreading Gakkel ridge in the Arctic Ocean, Nature, 421, 252–256, https://doi.org/10.1038/nature01351, 2003.

Fahrbach, E., Meincke, J., Østerhus, S., Rohardt, G., Schauer, U., Tverberg, V., and Verduin, J.: Direct measurements of volume transports through Fram Strait, Polar Res., 20, 217–224, https://doi.org/10.3402/polar.v20i2.6520, 2001.

Folkers, M. and Rombouts, T.: Sponges Revealed: A Synthesis of Their Overlooked Ecological Functions Within Aquatic Ecosystems, in: YOUMARES 9 – The Oceans: Our Research, Our Future: Proceedings of the 2018 conference for YOUng MArine RESearcher in Oldenburg, Germany, September 2018, edited by: Jungblut, S., Liebich, V., and Bode-Dalby, M., Springer International Publishing, Cham, 181–193, https://doi.org/10.1007/978-3-030-20389-4_9, 2020.

Fouilland, E., Floc'h, E. L., Brennan, D., Bell, E. M., Lordsmith, S. L., McNeill, S., Mitchell, E., Brand, T. D., García-Martín, E. E., and Leakey, R. J.: Assessment of bacterial dependence on marine primary production along a northern latitudinal gradient, FEMS Microbiol. Ecol., 94, fiy150, https://doi.org/10.1093/femsec/fiy150, 2018.

Fuchida, S., Mizuno, Y., Masuda, H., Toki, T., and Makita, H.: Concentrations and distributions of amino acids in black and white smoker fluids at temperatures over 200 °C, Org. Geochem., 66, 98–106, https://doi.org/10.1016/j.orggeochem.2013.11.008, 2014.

German, C. R. and Boetius, A.: Hydrothermal Exploration of the Gakkel Ridge, 2014 and 2016, Goldschmidt Abstracts, 1, 1324, https://goldschmidtabstracts.info/abstracts/abstractView?id=2017001867 (last access: 14 April 2022), 2017.

German, C. R. and Seyfried, W. E.: Hydrothermal Processes, in: Treatise on Geochemistry, Elsevier, 191–233, https://doi.org/10.1016/B978-0-08-095975-7.00607-0, 2014.

German, C. R., Bowen, A., Coleman, M. L., Honig, D. L., Huber, J. A., Jakuba, M. V., Kinsey, J. C., Kurz, M. D., Leroy, S., McDermott, J. M., de Lépinay, B. M., Nakamura, K., Seewald, J. S., Smith, J. L., Sylva, S. P., Van Dover, C. L., Whitcomb, L. L., and Yoerger, D. R.: Diverse styles of submarine venting on the ultraslow spreading Mid-Cayman Rise, P. Natl. Acad. Sci. USA, 107, 14020–14025, https://doi.org/10.1073/pnas.1009205107, 2010.

Graves, C. A., Steinle, L., Rehder, G., Niemann, H., Connelly, D. P., Lowry, D., Fisher, R. E., Stott, A. W., Sahling, H., and James, R. H.: Fluxes and fate of dissolved methane released at the seafloor at the landward limit of the gas hydrate stability zone offshore western Svalbard: Dissolved methane off western Svalbard, J. Geophys. Res.-Oceans, 120, 6185–6201, https://doi.org/10.1002/2015JC011084, 2015.

Grossart, H.-P., Frindte, K., Dziallas, C., Eckert, W., and Tang, K. W.: Microbial methane production in oxygenated water column of an oligotrophic lake, P. Natl. Acad. Sci. USA, 108, 19657–19661, https://doi.org/10.1073/pnas.1110716108, 2011.

Grozeva, N. G., Klein, F., Seewald, J. S., and Sylva, S. P.: Chemical and isotopic analyses of hydrocarbon-bearing fluid inclusions in olivine-rich rocks, Philos. T. Roy. Soc. A, 378, 20180431, https://doi.org/10.1098/rsta.2018.0431, 2020.

Haberstroh, P. R. and Karl, D. M.: Dissolved free amino acids in hydrothermal vent habitats of the Guaymas Basin, Geochim. Cosmochim. Ac., 53, 2937–2945, https://doi.org/10.1016/0016-7037(89)90170-1, 1989.

Hannington, M., Jamieson, J., Monecke, T., Petersen, S., and Beaulieu, S.: The abundance of seafloor massive sulfide deposits, Geology, 39, 1155–1158, https://doi.org/10.1130/G32468.1, 2011.

Hansell, D. A.: Recalcitrant Dissolved Organic Carbon Fractions, Annu. Rev. Mar. Sci., 5, 421–445, https://doi.org/10.1146/annurev-marine-120710-100757, 2013.

Hansen, C. T., Niggemann, J., Giebel, H.-A., Simon, M., Bach, W., and Dittmar, T.: Biodegradability of hydrothermally altered deep-sea dissolved organic matter, Mar. Chem., 217, 103706, https://doi.org/10.1016/j.marchem.2019.103706, 2019.

Hawkes, J. A., Rossel, P. E., Stubbins, A., Butterfield, D., Connelly, D. P., Achterberg, E. P., Koschinsky, A., Chavagnac, V., Hansen, C. T., Bach, W., and Dittmar, T.: Efficient removal of recalcitrant deep-ocean dissolved organic matter during hydrothermal circulation, Nat. Geosci., 8, 856–860, https://doi.org/10.1038/ngeo2543, 2015.

Hawkes, J. A., Hansen, C. T., Goldhammer, T., Bach, W., and Dittmar, T.: Molecular alteration of marine dissolved organic matter under experimental hydrothermal conditions, Geochim. Cosmochim. Ac., 175, 68–85, https://doi.org/10.1016/j.gca.2015.11.025, 2016.

Hedges, J. I.: Global biogeochemical cycles: progress and problems, Mar. Chem., 39, 67–93, https://doi.org/10.1016/0304-4203(92)90096-S, 1992.

Hertkorn, N., Harir, M., Cawley, K. M., Schmitt-Kopplin, P., and Jaffé, R.: Molecular characterization of dissolved organic matter from subtropical wetlands: a comparative study through the analysis of optical properties, NMR and FTICR/MS, Biogeosciences, 13, 2257–2277, https://doi.org/10.5194/bg-13-2257-2016, 2016.

Hestetun, J. T., Dahle, H., Jørgensen, S. L., Olsen, B. R., and Rapp, H. T.: The Microbiome and Occurrence of Methanotrophy in Carnivorous Sponges, Front. Microbiol., 7, 1781, https://doi.org/10.3389/fmicb.2016.01781, 2016.

Hill, V. J. and Zimmerman, R. C.: Characteristics of colored dissolved organic material in first year landfast sea ice and the underlying water column in the Canadian Arctic in the early spring, Mar. Chem., 180, 1–13, https://doi.org/10.1016/j.marchem.2016.01.007, 2016.

Hockaday, W. C., Purcell, J. M., Marshall, A. G., Baldock, J. A., and Hatcher, P. G.: Electrospray and photoionization mass spectrometry for the characterization of organic matter in natural waters: a qualitative assessment, Limnol. Oceanogr.-Meth., 7, 81–95, 2009.

Hodgkins, S. B., Tfaily, M. M., Podgorski, D. C., McCalley, C. K., Saleska, S. R., Crill, P. M., Rich, V. I., Chanton, J. P., and Cooper, W. T.: Elemental composition and optical properties reveal changes in dissolved organic matter along a permafrost thaw chronosequence in a subarctic peatland, Geochim. Cosmochim. Ac., 187, 123–140, https://doi.org/10.1016/j.gca.2016.05.015, 2016.

Horiuchi, T., Takano, Y., Ishibashi, J., Marumo, K., Urabe, T., and Kobayashi, K.: Amino acids in water samples from deep sea hydrothermal vents at Suiyo Seamount, Izu-Bonin Arc, Pacific Ocean, Org. Geochem., 35, 1121–1128, https://doi.org/10.1016/j.orggeochem.2004.06.006, 2004.

Jaffé, R., Yamashita, Y., Maie, N., Cooper, W. T., Dittmar, T., Dodds, W. K., Jones, J. B., Myoshi, T., Ortiz-Zayas, J. R., Podgorski, D. C., and Watanabe, A.: Dissolved Organic Matter in Headwater Streams: Compositional Variability across Climatic Regions of North America, Geochim. Cosmochim. Ac., 94, 95–108, https://doi.org/10.1016/j.gca.2012.06.031, 2012.

Jakobsson, M., Macnab, R., Mayer, L., Anderson, R., Edwards, M., Hatzky, J., Schenke, H. W., and Johnson, P.: An improved bathymetric portrayal of the Arctic Ocean: Implications for ocean modeling and geological, geophysical and oceanographic analyses, Geophys. Res. Lett., 35, L07602, https://doi.org/10.1029/2008GL033520, 2008.

Jørgensen, L., Stedmon, C. A., Kaartokallio, H., Middelboe, M., and Thomas, D. N.: Changes in the composition and bioavailability of dissolved organic matter during sea ice formation, Limnol. Oceanogr., 60, 817–830, 2015.

Karl, D., Beversdorf, L., Orkman, K., Church, M., Martinez, A., and Delong, E.: Aerobic production of methane in the sea, Nat. Geosci., 1, 473–478, https://doi.org/10.1038/ngeo234, 2008.

Keeling, C. D.: The concentration and isotopic abundances of carbon dioxide in rural and marine air, Geochim. Cosmochim. Ac., 24, 277–298, https://doi.org/10.1016/0016-7037(61)90023-0, 1961.

Keir, R. S., Sültenfuß, J., Rhein, M., Petrick, G., and Greinert, J.: Separation of 3He and CH4 signals on the Mid-Atlantic Ridge at 5° N and 51° N, Geochim. Cosmochim. Ac., 70, 5766–5778, https://doi.org/10.1016/j.gca.2006.06.005, 2006.

Keir, R. S., Schmale, O., Seifert, R., and Sültenfuß, J.: Isotope fractionation and mixing in methane plumes from the Logatchev hydrothermal field, Geochem. Geophy. Geosy., 10, Q05005, https://doi.org/10.1029/2009GC002403, 2009.

Kim, S., Kramer, R. W., and Hatcher, P. G.: Graphical Method for Analysis of Ultrahigh-Resolution Broadband Mass Spectra of Natural Organic Matter, the Van Krevelen Diagram, Anal. Chem., 75, 5336–5344, https://doi.org/10.1021/ac034415p, 2003.

Kudo, K., Yamada, K., Toyoda, S., Yoshida, N., Sasano, D., Kosugi, N., Ishii, M., Yoshikawa, H., Murata, A., Uchida, H., and Nishino, S.: Spatial distribution of dissolved methane and its source in the western Arctic Ocean, J. Oceanogr., 74, 305–317, https://doi.org/10.1007/s10872-017-0460-y, 2018.

Kujawinski, E. B., Longnecker, K., Blough, N. V., Vecchio, R. D., Finlay, L., Kitner, J. B., and Giovannoni, S. J.: Identification of possible source markers in marine dissolved organic matter using ultrahigh resolution mass spectrometry, Geochim. Cosmochim. Ac., 73, 4384–4399, https://doi.org/10.1016/j.gca.2009.04.033, 2009.

Lang, S. Q., Butterfield, D. A., Lilley, M. D., Johnson, H. P., and Hedges, J. I.: Dissolved organic carbon in ridge-axis and ridge-flank hydrothermal systems, Geochim. Cosmochim. Ac., 70, 3830–3842, https://doi.org/10.1016/j.gca.2006.04.031, 2006.

Lang, S. Q., Butterfield, D. A., Schulte, M., Kelley, D. S., and Lilley, M. D.: Elevated concentrations of formate, acetate and dissolved organic carbon found at the Lost City hydrothermal field, Geochim. Cosmochim. Ac., 74, 941–952, https://doi.org/10.1016/j.gca.2009.10.045, 2010.

Levin, L. A., Baco, A. R., Bowden, D. A., Colaco, A., Cordes, E. E., Cunha, M. R., Demopoulos, A. W. J., Gobin, J., Grupe, B. M., Le, J., Metaxas, A., Netburn, A. N., Rouse, G. W., Thurber, A. R., Tunnicliffe, V., Van Dover, C. L., Vanreusel, A., and Watling, L.: Hydrothermal Vents and Methane Seeps: Rethinking the Sphere of Influence, Front. Mar. Sci., 3, 72, https://doi.org/10.3389/fmars.2016.00072, 2016.

Li, G., Xie, H., Song, G., and Gosselin, M.: Production of Chromophoric Dissolved Organic Matter (CDOM) in Laboratory Cultures of Arctic Sea Ice Algae, Water, 11, 926, https://doi.org/10.3390/w11050926, 2019.

Liu, S., He, Z., Tang, Z., Liu, L., Hou, J., Li, T., Zhang, Y., Shi, Q., Giesy, J. P., and Wu, F.: Linking the molecular composition of autochthonous dissolved organic matter to source identification for freshwater lake ecosystems by combination of optical spectroscopy and FT-ICR-MS analysis, Sci. Total Environ., 703, 134764, https://doi.org/10.1016/j.scitotenv.2019.134764, 2020.

Longnecker, K.: Dissolved organic matter in newly formed sea ice and surface seawater, Geochim. Cosmochim. Ac., 171, 39–49, https://doi.org/10.1016/j.gca.2015.08.014, 2015.

Longnecker, K., Sievert, S. M., Sylva, S. P., Seewald, J. S., and Kujawinski, E. B.: Dissolved organic carbon compounds in deep-sea hydrothermal vent fluids from the East Pacific Rise at 9°50′ N, Org. Geochem., 125, 41–49, https://doi.org/10.1016/j.orggeochem.2018.08.004, 2018.

Lorenson, T. D., Greinert, J., and Coffin, R. B.: Dissolved methane in the Beaufort Sea and the Arctic Ocean, 1992–2009; sources and atmospheric flux, Limnol. Oceanogr., 61, S300–S323, https://doi.org/10.1002/lno.10457, 2016.

Lupton, J. E. and Craig, H.: A Major Helium-3 Source at 15° S on the East Pacific Rise, Science, 214, 13–18, https://doi.org/10.1126/science.214.4516.13, 1981.

Marcon, Y., Purser, A., Albers, E., Türke, A., German, C., Hand, K., Schlindwein, V., Dorschel, B., Boetius, A., and Bach, W.: Geological settings of hydrothermal vents at 6°15′ W and 55°30′ E on the Gakkel Ridge, Arctic Ocean, Goldschmidt Abstracts, 1, 2566, https://goldschmidtabstracts.info/abstracts/abstractView?id=2017004414 (last access: 14 April 2022), 2017.

Marnela, M., Rudels, B., Olsson, K. A., Anderson, L. G., Jeansson, E., Torres, D. J., Messias, M.-J., Swift, J. H., and Watson, A. J.: Transports of Nordic Seas water masses and excess SF6 through Fram Strait to the Arctic Ocean, Prog. Oceanogr., 78, 1–11, https://doi.org/10.1016/j.pocean.2007.06.004, 2008.

McCollom, T. M. and Seewald, J. S.: Abiotic Synthesis of Organic Compounds in Deep-Sea Hydrothermal Environments, Chem. Rev., 107, 382–401, https://doi.org/10.1021/cr0503660, 2007.

McCollom, T. M., Ritter, G., and Simoneit, B. R. T.: Lipid Synthesis Under Hydrothermal Conditions by Fischer- Tropsch-Type Reactions, Origins Life Evol. B., 29, 153–166, 1999.

McCollom, T. M., Seewald, J. S., and German, C. R.: Investigation of extractable organic compounds in deep-sea hydrothermal vent fluids along the Mid-Atlantic Ridge, Geochim. Cosmochim. Ac., 156, 122–144, https://doi.org/10.1016/j.gca.2015.02.022, 2015.

McDermott, J. M., Seewald, J. S., German, C. R., and Sylva, S. P.: Pathways for abiotic organic synthesis at submarine hydrothermal fields, PNAS, 112, 7668–7672, https://doi.org/10.1073/pnas.1506295112, 2015.

McDermott, J. M., Albers, E., Bach, W., Diehl, A., German, C. R., Hand, K., Koehler, J., Walter, M., Wegener, G., and Boetius, A.: Geochemistry, physics, and dispersion of a Gakkel Ridge hydrothermal plume, 87° N, 55°30′ E, Goldschmidt Abstracts, 1, 2654, https://goldschmidtabstracts.info/abstracts/abstractView?id=2017006020 (last access: 14 April 2022), 2017.

Michael, P. J., Langmuir, C. H., Dick, H. J. B., Snow, J. E., Goldstein, S. L., Graham, D. W., Lehnert, K., Kurras, G., Jokat, W., Mühe, R., and Edmonds, H. N.: Magmatic and amagmatic seafloor generation at the ultraslow-spreading Gakkel ridge, Arctic Ocean, Nature, 423, 956–961, https://doi.org/10.1038/nature01704, 2003.

Mopper, K., Stubbins, A., Ritchie, J. D., Bialk, H. M., and Hatcher, P. G.: Advanced Instrumental Approaches for Characterization of Marine Dissolved Organic Matter: Extraction Techniques, Mass Spectrometry, and Nuclear Magnetic Resonance Spectroscopy, Chem. Rev., 107, 419–442, https://doi.org/10.1021/cr050359b, 2007.

Nakamura, K. and Takai, K.: Theoretical constraints of physical and chemical properties of hydrothermal fluids on variations in chemolithotrophic microbial communities in seafloor hydrothermal systems, Progress in Earth and Planetary Science, 1, 5, https://doi.org/10.1186/2197-4284-1-5, 2014.

Noowong, A., Gomez-Saez, G. V., Hansen, C. T., Schwarz-Schampera, U., Koschinsky, A., and Dittmar, T.: Imprint of Kairei and Pelagia deep-sea hydrothermal systems (Indian Ocean) on marine dissolved organic matter, Org. Geochem., 152, 104141, https://doi.org/10.1016/j.orggeochem.2020.104141, 2021.

Ohno, T., Sleighter, R. L., and Hatcher, P. G.: Comparative study of organic matter chemical characterization using negative and positive mode electrospray ionization ultrahigh-resolution mass spectrometry, Anal. Bioanal. Chem., 408, 2497–2504, https://doi.org/10.1007/s00216-016-9346-x, 2016.

Oksanen, J., Blanchet, F. G., Friendly, M., Kindt, R., Legendre, P., McGlinn, D., Minchin, P. R., O'Hara, R. B., Simpson, G. L., Solymos, P., Stevens, M. H. H., Szoecs, E., and Wagner, H.: vegan: Community Ecology Package, R package version 2.5-7, https://CRAN.R-project.org/package=vegan (last access: 14 April 2022), 2020.

Ortmann, A. and Suttle, C.: High abundance of viruses in a deep-sea hydrothermal vent system indicates viral mediated microbial mortality, Deep-Sea Res. Pt. I, 52, 1515–1527, https://doi.org/10.1016/j.dsr.2005.04.002, 2005.

Osterholz, H., Kirchman, D. L., Niggemann, J., and Dittmar, T.: Environmental Drivers of Dissolved Organic Matter Molecular Composition in the Delaware Estuary, Front. Earth Sci., 4, 35, https://doi.org/10.3389/feart.2016.00095, 2016.

Östlund, H. G. and Hut, G.: Arctic Ocean water mass balance from isotope data, J. Geophys. Res., 89, 6373, https://doi.org/10.1029/JC089iC04p06373, 1984.

Paradis, E. and Schliep, K.: ape 5.0: an environment for modern phylogenetics and evolutionary analyses in R, Bioinformatics, 35, 526–528, https://doi.org/10.1093/bioinformatics/bty633, 2019.

Pataki, D. E., Ehleringer, J. R., Flanagan, L. B., Yakir, D., Bowling, D. R., Still, C. J., Buchmann, N., Kaplan, J. O., and Berry, J. A.: The application and interpretation of Keeling plots in terrestrial carbon cycle research, Global Biogeochem. Cy., 17, 1022, https://doi.org/10.1029/2001GB001850, 2003.

Pedersen, R. B., Rapp, H. T., Thorseth, I. H., Lilley, M. D., Barriga, F. J. A. S., Baumberger, T., Flesland, K., Fonseca, R., Früh-Green, G. L., and Jorgensen, S. L.: Discovery of a black smoker vent field and vent fauna at the Arctic Mid-Ocean Ridge, Nat. Commun., 1, 126, https://doi.org/10.1038/ncomms1124, 2010.

Purser, A., Marcon, Y., Dreutter, S., Hoge, U., Sablotny, B., Hehemann, L., Lemburg, J., Dorschel, B., Biebow, H., and Boetius, A.: Ocean Floor Observation and Bathymetry System (OFOBS): A New Towed Camera/Sonar System for Deep-Sea Habitat Surveys, IEEE J. Oceanic Eng., 44, 87–99, https://doi.org/10.1109/JOE.2018.2794095, 2019.

Qian, J. and Mopper, K.: Automated High-Performance, High-Temperature Combustion Total Organic Carbon Analyzer, Anal. Chem., 68, 3090–3097, https://doi.org/10.1021/ac960370z, 1996.

R Core Team: R: A Language and Environment for Statistical Computing, R Foundation for Statistical Computing, Vienna, Austria, https://www.R-project.org/ (last access: 14 April 2022), 2018.

Ramirez-Llodra, E., Brandt, A., Danovaro, R., De Mol, B., Escobar, E., German, C. R., Levin, L. A., Martinez Arbizu, P., Menot, L., Buhl-Mortensen, P., Narayanaswamy, B. E., Smith, C. R., Tittensor, D. P., Tyler, P. A., Vanreusel, A., and Vecchione, M.: Deep, diverse and definitely different: unique attributes of the world's largest ecosystem, Biogeosciences, 7, 2851–2899, https://doi.org/10.5194/bg-7-2851-2010, 2010.

Redfield, A. C.: The biological control of chemical factors in the environment, Am. Sci., 46, 205–221, 1958.

Reeburgh, W. S.: Oceanic Methane Biogeochemistry, Chem. Rev., 107, 486–513, https://doi.org/10.1021/cr050362v, 2007.

Reeves, E. P. and Fiebig, J.: Abiotic Synthesis of Methane and Organic Compounds in Earth's Lithosphere, Elements, 16, 25–31, https://doi.org/10.2138/gselements.16.1.25, 2020.

Retelletti Brogi, S., Ha, S.-Y., Kim, K., Derrien, M., Lee, Y. K., and Hur, J.: Optical and molecular characterization of dissolved organic matter (DOM) in the Arctic ice core and the underlying seawater (Cambridge Bay, Canada): Implication for increased autochthonous DOM during ice melting, Sci. Total Environ., 627, 802–811, https://doi.org/10.1016/j.scitotenv.2018.01.251, 2018.

Rossel, P. E., Stubbins, A., Hach, P. F., and Dittmar, T.: Bioavailability and molecular composition of dissolved organic matter from a diffuse hydrothermal system, Mar. Chem., 177, 257–266, https://doi.org/10.1016/j.marchem.2015.07.002, 2015.

Rossel, P. E., Stubbins, A., Rebling, T., Koschinsky, A., Hawkes, J. A., and Dittmar, T.: Thermally altered marine dissolved organic matter in hydrothermal fluids, Org. Geochem., 110, 73–86, https://doi.org/10.1016/j.orggeochem.2017.05.003, 2017.

Rudels, B., Wadhams, P., Dowdeswell, J. A., and Schofield, A. N.: The thermohaline circulation of the Arctic Ocean and the Greenland Sea, Philos. T. R. Soc. A, 352, 287–299, https://doi.org/10.1098/rsta.1995.0071, 1995.

Rudels, B., Björk, G., Nilsson, J., Winsor, P., Lake, I., and Nohr, C.: The interaction between waters from the Arctic Ocean and the Nordic Seas north of Fram Strait and along the East Greenland Current: results from the Arctic Ocean-02 Oden expedition, J. Marine Syst., 55, 1–30, https://doi.org/10.1016/j.jmarsys.2004.06.008, 2005.

Rudnicki, M. D. and Elderfield, H.: A chemical model of the buoyant and neutrally buoyant plume above the TAG vent field, 26 degrees N, Mid-Atlantic Ridge, Geochim. Cosmochim. Ac., 57, 2939–2957, https://doi.org/10.1016/0016-7037(93)90285-5, 1993.

Santibáñez, P. A., Michaud, A. B., Vick-Majors, T. J., D'Andrilli, J., Chiuchiolo, A., Hand, K. P., and Priscu, J. C.: Differential Incorporation of Bacteria, Organic Matter, and Inorganic Ions Into Lake Ice During Ice Formation, J. Geophys. Res.-Biogeo., 124, 585–600, https://doi.org/10.1029/2018JG004825, 2019.

Sert, M. F., D'Andrilli, J., Gründger, F., Niemann, H., Granskog, M. A., Pavlov, A. K., Ferré, B., and Silyakova, A.: Compositional Differences in Dissolved Organic Matter Between Arctic Cold Seeps Versus Non-Seep Sites at the Svalbard Continental Margin and the Barents Sea, Front. Earth Sci., 8, 552731, https://doi.org/10.3389/feart.2020.552731, 2020.

Sert, M. F., Reeves, E. P., Hand, K. P., and Ferré, B.: Replication data for: Compositions of dissolved organic matter in the ice-covered waters above the Aurora hydrothermal vent system, Gakkel Ridge, Arctic Ocean, DataverseNO [data set] and [code], https://doi.org/10.18710/QPGDFW, 2021.

Simoneit, B. R. T.: Aqueous organic geochemistry at high temperature/high pressure, Origins Life Evol. B., 22, 43–65, https://doi.org/10.1007/BF01808018, 1992.

Simoneit, B. R. T.: Evidence for organic synthesis in high temperature aqueous media – Facts and prognosis, Origins Life Evol. B., 25, 119–140, https://doi.org/10.1007/BF01581578, 1995.

Simoneit, B. R. T., Lein, A. Yu., Peresypkin, V. I., and Osipov, G. A.: Composition and origin of hydrothermal petroleum and associated lipids in the sulfide deposits of the Rainbow field (Mid-Atlantic Ridge at 36° N), Geochim. Cosmochim. Ac., 68, 2275–2294, https://doi.org/10.1016/j.gca.2003.11.025, 2004.

Speer, K. G. and Rona, P. A.: A model of an Atlantic and Pacific hydrothermal plume, J. Geophys. Res.-Oceans, 94, 6213–6220, https://doi.org/10.1029/JC094iC05p06213, 1989.

Tao, Y., Rosswog, S., and Brüggen, M.: A simulation modeling approach to hydrothermal plumes and its comparison to analytical models, Ocean Model., 61, 68–80, https://doi.org/10.1016/j.ocemod.2012.10.001, 2013.

Thingstad, T. F., Hagström, Å., and Rassoulzadegan, F.: Accumulation of degradable DOC in surface waters: Is it caused by a malfunctioning microbial loop?, Limnol. Oceanogr., 42, 398–404, https://doi.org/10.4319/lo.1997.42.2.0398, 1997.

Vanreusel, A., Andersen, A., Boetius, A., Connelly, D., Cunha, M., Decker, C., Heeschen, K., Hilario, A., Kormas, K., Maignien, L., Olu, K., Pachiadaki, M., Ritt, B., Rodrigues, C., Sarrazin, J., Tyler, P., Van Gaever, S., and Vanneste, H.: Biodiversity of Cold Seep Ecosystems Along the European Margins, Oceanography, 22, 110–127, https://doi.org/10.5670/oceanog.2009.12, 2009.

Vergeynst, L., Christensen, J. H., Kjeldsen, K. U., Meire, L., Boone, W., Malmquist, L. M. V., and Rysgaard, S.: In situ biodegradation, photooxidation and dissolution of petroleum compounds in Arctic seawater and sea ice, Water Res., 148, 459–468, https://doi.org/10.1016/j.watres.2018.10.066, 2019.

Wang, D. T., Reeves, E. P., McDermott, J. M., Seewald, J. S., and Ono, S.: Clumped isotopologue constraints on the origin of methane at seafloor hot springs, Geochim. Cosmochim. Ac., 223, 141–158, https://doi.org/10.1016/j.gca.2017.11.030, 2018.

Whiticar, M. J.: Carbon and hydrogen isotope systematics of bacterial formation and oxidation of methane, Chem. Geol., 161, 291–314, https://doi.org/10.1016/S0009-2541(99)00092-3, 1999.

Winkler, L. W.: Die Bestimmung des im Wasser gelösten Sauerstoffes, Ber. Dtsch. Chem. Ges., 21, 2843–2854, https://doi.org/10.1002/cber.188802102122, 1888.

Xu, W., Gao, Q., He, C., Shi, Q., Hou, Z.-Q., and Zhao, H.-Z.: Using ESI FT-ICR MS to Characterize Dissolved Organic Matter in Salt Lakes with Different Salinity, Environ. Sci. Technol., 54, 12929–12937, https://doi.org/10.1021/acs.est.0c01681, 2020.

Yahel, G., Sharp, J. H., Marie, D., Häse, C., and Genin, A.: In situ feeding and element removal in the symbiont-bearing sponge Theonella swinhoei: Bulk DOC is the major source for carbon, Limnol. Oceanogr., 48, 141–149, https://doi.org/10.4319/lo.2003.48.1.0141, 2003.

Yücel, M., Gartman, A., Chan, C. S., and Luther, G. W.: Hydrothermal vents as a kinetically stable source of iron-sulphide-bearing nanoparticles to the ocean, Nat. Geosci., 4, 367–371, https://doi.org/10.1038/ngeo1148, 2011.

Supplement of Biogeosciences, 19, 2101–2120, 2022
https://doi.org/10.5194/bg-19-2101-2022-supplement

Biogeosciences Open Access EGU

Supplement of

Compositions of dissolved organic matter in the ice-covered waters above the Aurora hydrothermal vent system, Gakkel Ridge, Arctic Ocean

Muhammed Fatih Sert et al.

Correspondence to: Muhammed Fatih Sert (muhammed.f.sert@uit.no)

Supplementary Information

Supplementary information 1: Post calibration of beam attenuation coefficient values

The equation used for calculating beam attenuation coefficient was

$$\text{Beam attenuation coefficient } (c, [1/m]) = -(1 / z) * \ln(\text{light transmission [decimal]})$$

where z = path length 0.25 m.

Afterwards, c values were post calibrated with an offset value that was calculated based on the theoretical clear water minimum beam attenuation coefficient of 0.364 (Intergovernmental Oceanographic Commission, 1994).

$$\text{offset} = c_{min} - 0.364$$

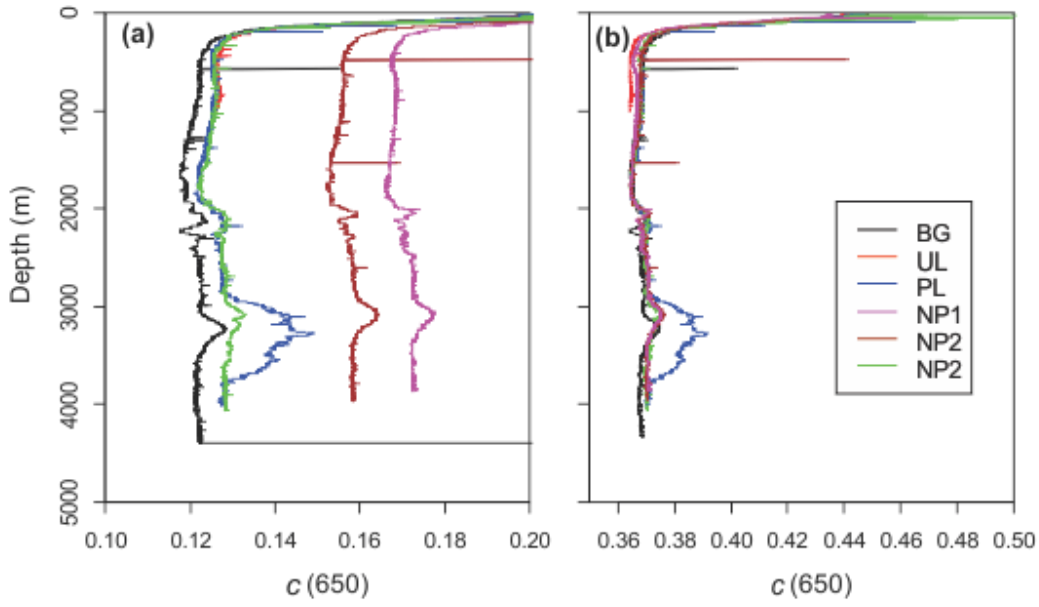

Supplementary Figure 1: Beam attenuation coefficient values before (a) and after (b) post calibration in background (BG), upper layer (UL), plume (PL) and non-plume (NP1-NP3) stations.

Supplementary information 2: Use of HiPAP data

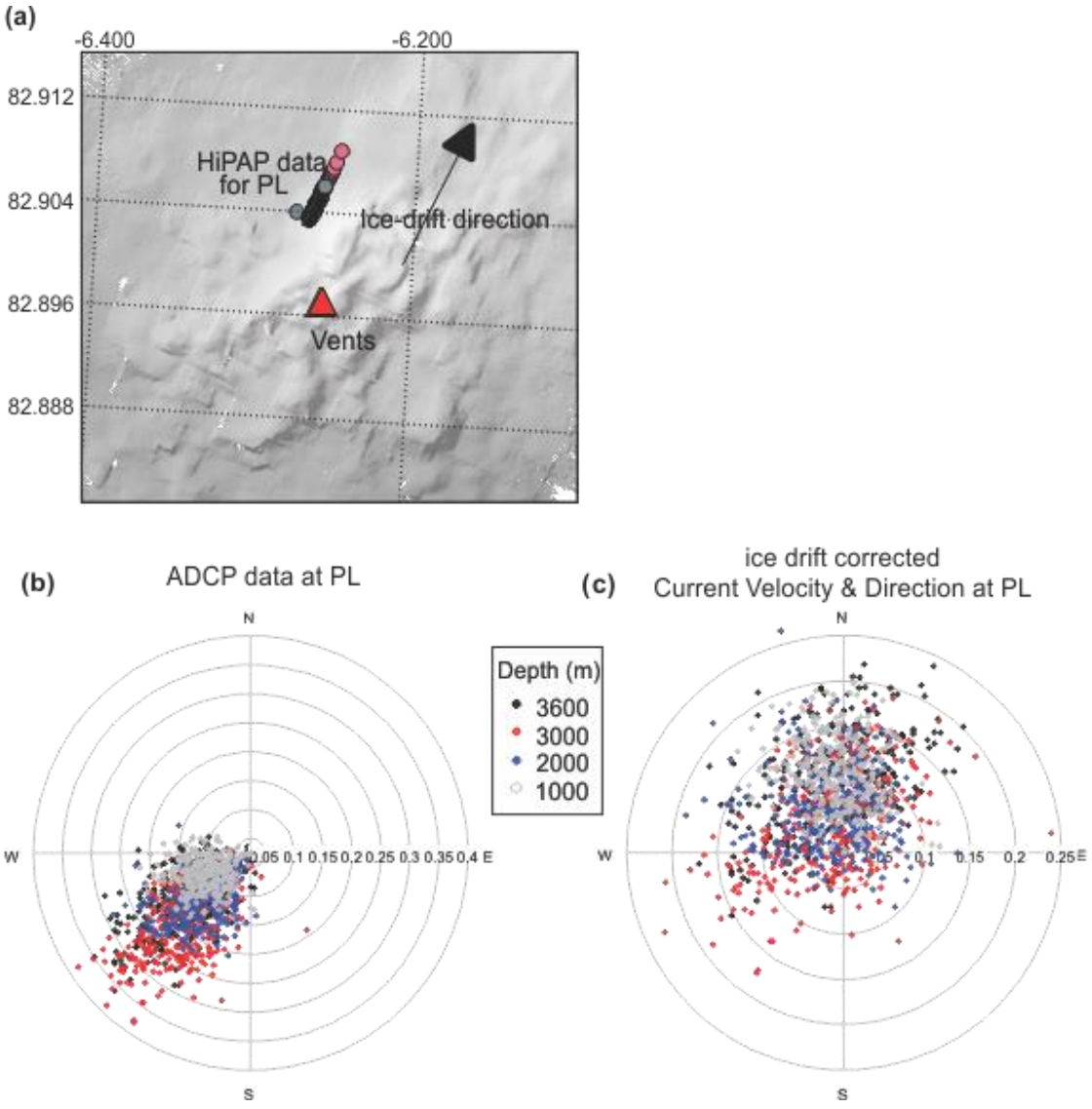

Supplementary Figure 2: (a) High precision acoustic profiler (HiPAP) data obtained at plume (PL) station and ice drift direction of the vessel on map. (b) ADCP data obtained at several depths of PL and (c) ADCP data after ice drift correction that shows actual current direction at given depths.

25

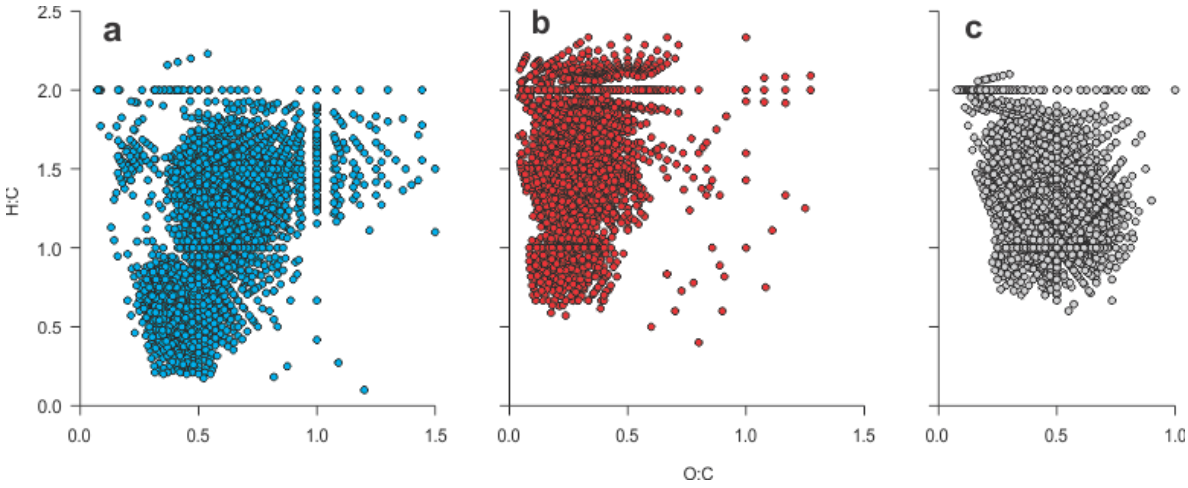

Supplementary Figure 3: Dissolved organic matter (DOM) formulas on van Krevelen diagram obtained from (a) negative ESI (electrospray ionization), (b) positive ESI and (c) formulas common in negative and positive ESI.

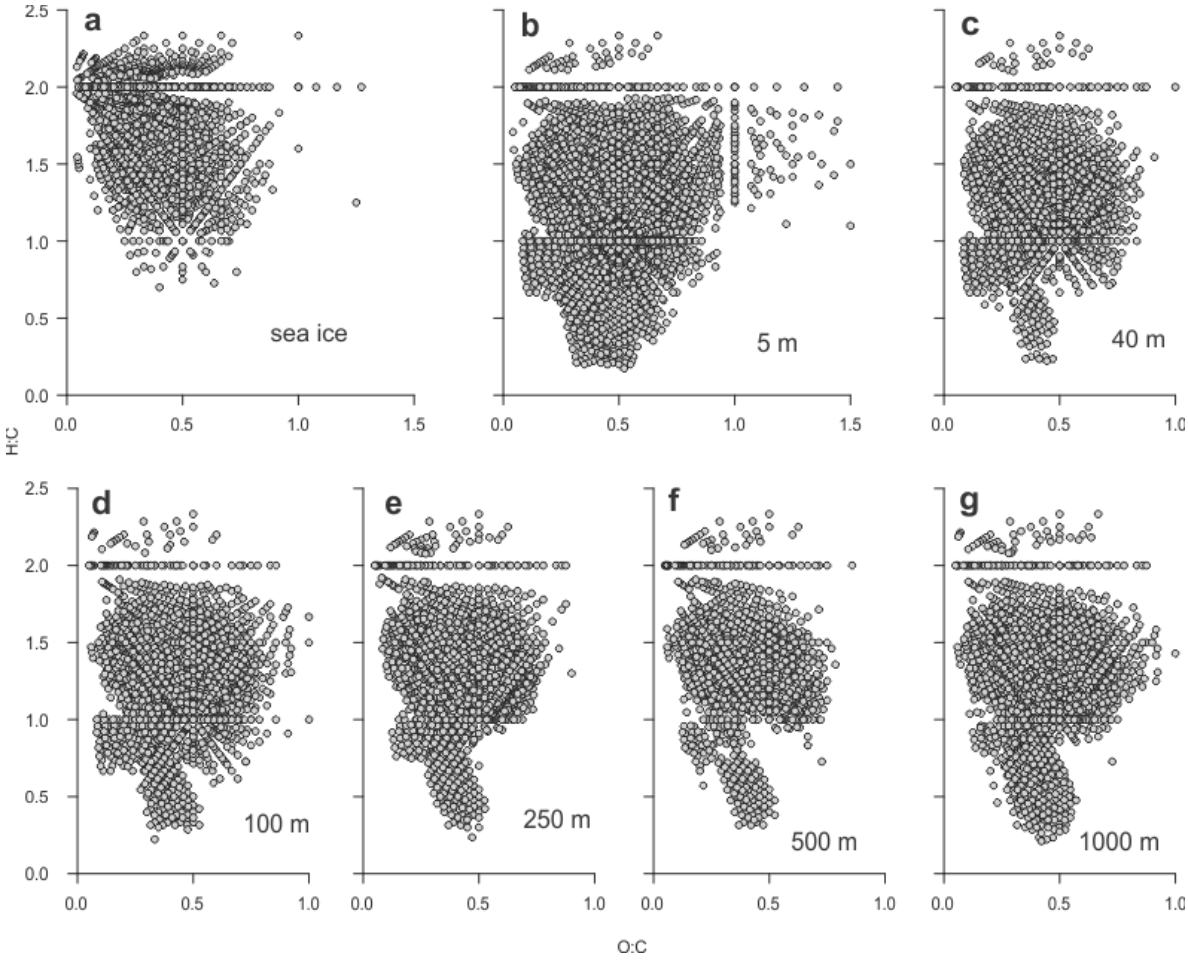

Supplementary Figure 4: Dissolved organic matter (DOM) formulas on van Krevelen diagram obtained in sea ice and upper layer (UL) station.

References

Intergovernmental Oceanographic Commission: Protocols for the Joint Global Ocean Flux Study (JGOFS) Core Measurements, Unesco, https://doi.org/10.25607/OBP-1409, 1994.

Chapter 4

Paper III

Elevated methane alters dissolved organic matter composition in the Arctic Ocean cold seeps